Development of metal sulfide/S-doped metal oxide photocatalysts for H_2 evolution from water under visible-light irradiation

（金属硫化物/硫黄ドープ金属酸化物光触媒材料の開発とその可視光応答水素発生）

Zongwei MEI

梅　宗維

Department of Chemistry

Graduate School of Science

Hokkaido University

北海道大学

2013

ABSTRACT

Photocatalytic water splitting is an ideal route to convert solar energy into clean H_2 energy. In the view of efficient utilization of solar energy, the photocatalysts are necessary to be sensitive to visible light, which takes about 43% of the whole solar energy. Furthermore, the photocatalysts should also show efficient separation and migration ability of the photoexcited carriers (electrons and holes), because the photocatalytic reaction utilizes the photoexcited electrons and holes migrating to the surface of the photocatalyst.

In comparison with metal oxides, most metal sulfides and S-doped metal oxides are attractive visible-light-sensitive photocatalysts for H_2 evolution. The S 3*p* orbitals substituting for or hybridizing with O 2*p* orbitals can narrow band gaps by lifting up the top of the valence band. Furthermore, the sulfides and S-doped oxides which contain elements with d^{10} electronic configurations (i.e., Zn and In) show good migration ability of the photoexcited carriers, because their conduction bands are constructed from the hybridized and broadly dispersed *sp* orbitals. However, few efforts have been devoted to the design and synthesis of more efficient photocatalysts based on Zn/In oxide or sulfide. In this thesis, the S-doped oxide and sulfide photocatalysts are studied, which contain In and/or Zn elements, and two strategies are adopted to enhance their energy-conversion-efficiency. The first one is the fabrication of appropriate semiconductor composite, of which the two components show different band potentials for both conduction and valence bands. The second one is the application of nanotechnology for fabricating photocatalyst with intrinsically high photocatalytic activity.

Chapter 1 provides an overview of the photocatalysis, and describes the thermodynamic conditions and main processes for photocatalytic water splitting. This chapter also

summarizes the development of semiconductor photocatalysts and strategies of achieving high photocatalytic activities.

Chapter 2 focuses on the fabrication, characterization and discussion of $Zn_5In_2O_8$/surface-S-doped $Zn_5In_2O_8$ composite which was synthesized through *in situ* sulfuration of the vacancy-rich $Zn_5In_2O_8$ in Na_2S/K_2SO_3 aqueous solution under UV-vis light irradiation. For the surface-S-doped layer, the bottom of conduction band was more negative than that of $Zn_5In_2O_8$, which resulted from the intentionally produced indium vacancy. However, the top of valence band was less positive than that of $Zn_5In_2O_8$ because of the S dopant. Therefore, the photoexcited electrons transferred from the conduction band of the surface-S-doped layer to that of $Zn_5In_2O_8$, and the photoexcited holes transferred from the valence band of $Zn_5In_2O_8$ to that of the surface-S-doped layer. This process enhanced the separation ability of the photoexcited electrons and holes, and accordingly enhanced the photocatalytic activity. The photocatalytic H_2 evolution rate of the sample sulfurized from the vacancy-rich $Zn_5In_2O_8$ was about 17 times higher than that of the sample synthesized by using the as-synthesized $Zn_5In_2O_8$. In this work, it was found that the indium vacancy and surface sulfuration played significant roles in enhancing the photocatalytic activity.

In comparison with the traditional composite, the bulk composite (interpenetrating networks formed by two semiconductors) is more beneficial to the efficient separation of photoexcited electrons and holes. On the other hand, In_2S_3 and $ZnIn_2S_4$ show narrower band gaps than $Zn_5In_2O_8$ and S-doped $Zn_5In_2O_8$, accordingly they can utilize more visible light.

Chapter 3 demonstrates the hierarchical $In_2S_3/ZnIn_2S_4$ bulk composites synthesized by an ion-exchange route under a solvothermal condition. The $In_2S_3/ZnIn_2S_4$ bulk composites showed highly improved photocatalytic activities for H_2 evolution under visible-light irradiation in comparison with the individual In_2S_3 and $ZnIn_2S_4$. The matched band edge potentials of In_2S_3 and $ZnIn_2S_4$, tight and fluent interface of the components facilitated the

more effective separation and migration of photoexcited carriers. Therefore, the photocatalytic activities of the $In_2S_3/ZnIn_2S_4$ bulk composites were greatly enhanced.

ZnS with more negative bottom of conduction band is more beneficial for photocatalytic H_2 evolution than $ZnIn_2S_4$ and In_2S_3. However, ZnS is not sensitive to visible light. Cu^{2+} doping is an effective approach to make ZnS sensitive to visible light because Cu 3*d* orbitals can lift up the top of valence band. In Chapter 4, $Zn_{1-x}Cu_xS$ ($0 \leq x \leq 0.066$) ultrathin nanocrystallines were synthesized by a complexing-wet-chemical method. The Cu^{2+} additive could be totally doped into the crystal structure of ZnS using this method. The products showed enhanced photocatalytic activities for H_2 evolution without cocatalyst than that synthesized by the traditional coprecipitation method. The enhanced photoactivities resulted from the homogeneous Cu^{2+} dopant and small nanoparticles.

Chapter 5 summarizes the importance and originality of this research, and provides future prospects of this work. The synthesis strategies developed in our work can be used to fabricate other high-performance functional semiconductors. It is also found that the photoexcited electrons on the conduction bands mainly constructed from Zn 4*s*4*p* orbitals show stronger reduction ability than those on the conduction bands mainly constructed from In 5*s*5*p* orbitals. It gives us meaningful information for the design of highly efficient photocatalysts.

CONTENTS

Chapter 1 Introduction

1.1 Overview of photocatalysis

In 1972, Fujishima and Honda discovered the photocatalytic water splitting into H_2 and O_2 by using TiO_2under UV irradiation [1], which inspired world-wide scientists' passion to develop practical applications of photocatalysis as environmentally friendly technologies under the background of energy crisis. At the mid of 1980s, Ollis and co-works found that hydroxyl radicals could be firstly produced under the light irradiation by using TiO_2 as the photocatalyst, and the produced hydroxyl radicals subsequently degraded the organic pollutants in the air or water environment [2-4]. During the subsequent 20 years, it had been reported that more than 1200 different organic toxicants could be degraded by photocatalysts [5]. In addition to H_2 evolution, detoxification of effluents, and decomposition of organic pollutants, many other potential applications of TiO_2 have also been developed, such as disinfection and superhydrophilic self-cleaning [6, 7].

Although TiO_2 is an efficient photocatalyst, it is not sensitive to visible light which takes about 43% of the whole solar energy [8]. Figure 1.1 exhibits the solar irradiation spectrum. During the last decade, great efforts have been devoted to develop other complex metal oxides as novel photocatalytic materials containing the cations of d^0 or d^{10} electronic configurations such as Ti^{4+}, Zr^{4+}, Nb^{5+}, Ta^{5+}, W^{6+}, Ga^{3+}, In^{3+}, Ge^{4+}, Sn^{4+}, Sb^{5+}, Bi^{5+}, and Ag^{+} [8-26]. In 2001, Zou *et al.* reported that $In_{1-x}Ni_xTaO_4$ could directly split pure water into H_2 and O_2 under visible-light irradiation [23]. It was a big step for photocatalysis by the concept of more efficient utilization of solar energy to visible light region. 5 years later, Domen *et al.* found that ZnO-GaN solid solution was an efficient overall-water-splitting photocatalyst under visible-light irradiation [27].

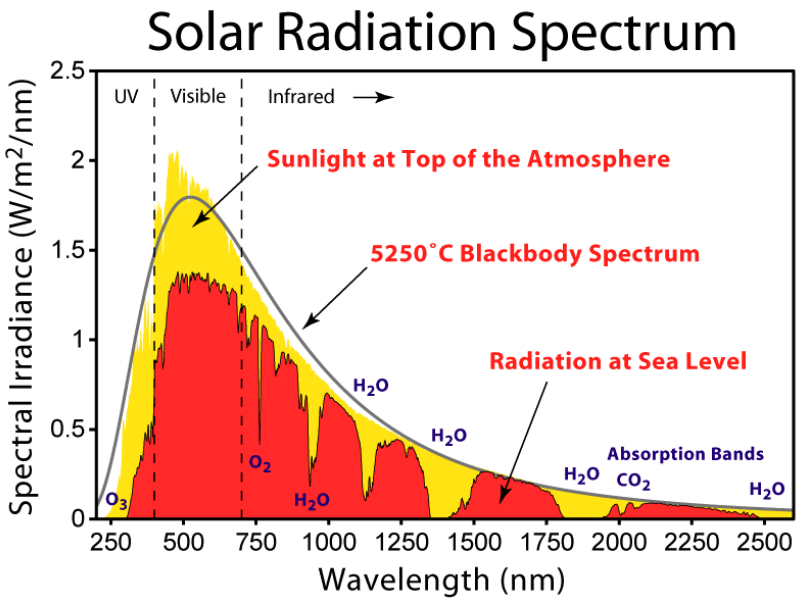

Figure 1.1 Solar radiation spectra above atmosphere and at the surface of the earth. Downloaded from http://en.wikipedia.org/wiki/Air_mass_(solar_energy).

At the same time, various efforts have also been devoted to develop new photocatalysts for the half reaction of water splitting (H_2 or O_2 evolution only). Metal sulfides are excellent candidates for photocatalytic H_2 evolution under visible-light irradiation. Pt-PdS/CdS was a typical material with extremely high quantum efficiency (93% around 420 nm) for visible-light-driven hydrogen production [28]. In recent years, highly efficient photocatalysts without expensive noble-metal cocatalyst have also been synthesized, such as Cu-doped ZnS [29], nanoporous ZnS-In_2S_3-Ag_2S solid solution [30], hierarchical ZnS-In_2S_3-CuS nanospheres with nanoporous structure [31], nanoporous single-crystal-like $Cd_xZn_{1-x}S$ nanosheets [32], porous CuS/ZnS nanosheets based on photoinduced interfacial charge transfer [33] etc. For the above materials, indium and cadmium are rare and poisonous elements, respectively. These demerits are not beneficial to the practical application for photocatalysts. Cu-doped ZnS is a hopeful candidate as an efficient, cheap, and environment-friendly photocatalyst. However, it is necessary to develop a new method for the controllable and homogeneous

dopant of Cu^{2+} into ZnS. For the half reaction of O_2 evolution from water splitting, Ag_3PO_4 and $BiVO_4$ were excellent candidates for the evolution of O_2under visible-light irradiation [34, 35]. Till now, researchers are still devoting great efforts to the development of high efficient, good stability, low cost, nontoxic, and visible-light-sensitive photocatalysts.

In the view of thermodynamics, the overall water splitting is an uphill reaction due to the large positive change of Gibbs free energy (ΔG^0 =237 kJ/mol). The principle of overall water splitting is shown in Figure 1.2. Firstly, the bottom of the conduction band should locate at a more negative position than the reduction potential of H^+ to H_2 (0 V versus the normal hydrogen electrode (NHE) at pH = 0). Secondly, the top of the valence band must locate at a more positive position than the oxidation potential of H_2O to O_2 (1.23 V versus NHE). The conduction band (CB) potential ranges from +0.5 V to -1.5 V NHE depending on the semiconductor and pH, while the valence band (VB) potential ranges from +1.0 V to +3.5 V versus NHE[36]. Accordingly, photoexcited electron and hole pairs (e^-/h^+ pairs) in semiconductors can initiate redox reactions and subsequently convert the light energy into chemical energy.

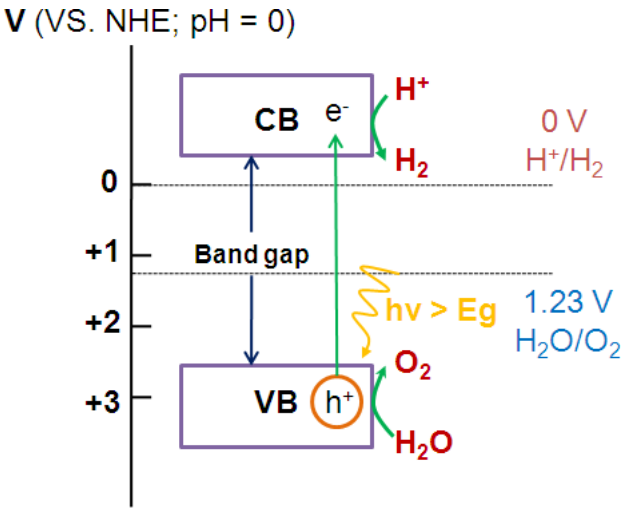

Figure 1.2 Principle of overall water splitting on a semiconductor photocatalyst.

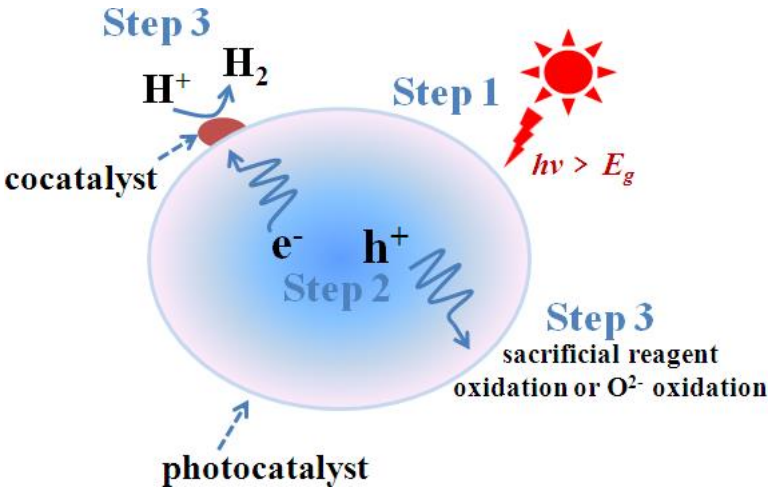

Figure 1.3 Processes occurring in semiconductor photocatalysts under light irradiation.

Figure 1.3 shows the fundamental processes of a semiconductor photocatalysis for water splitting (overall water splitting or half reaction for H_2 evolution). They can be summarized as three steps, (1) the photocatalyst absorbs photon energy which is higher than the band gap energy and generates e^-/h^+ pairs in the bulk, (2) the photoinduced e^-/h^+ pairs separate and migrate to the surface without recombination, and (3) surface reactions to form H_2 and O_2 or oxidation of sacrificial reagents. In the second step, a large proportion of the photoinduced e^-/h^+ pairs recombine.

In order to prevent the recombination of the photoinduced e^-/h^+ pairs, one usually can improve the crystallinity, decrease the particle size, and load cocatalyst such as Pt, Pd, NiO, and RuO_2 on the surface of photocatalyst. The higher crystallinity results in fewer defects which act as the recombination center of photoinduced e^-/h^+ pairs. The recombination of excited charges decreases the photocatalytic activity. On the other hand, the smaller size of the particle, the shorter distance that the photoinduced e^-/h^+ pairs must migrate to the reaction sites on the surface, which decrease the recombination probability. In the case of cocatalyst, a hetero-junction is built between the host semiconductor and the cocatalyst and subsequently an internal electric field is formed, which facilitates the separation of the photoexcited

carriers. Furthermore, these cocatalysts show better conductivity, lower overpotential, and higher catalytic activity than the host semiconductors. Accordingly, they usually act as ideal active sites for photocatalytic reactions.

1.2 Photocatalysts for water splitting

1.2.1 Metal oxide photocatalysts

As mentioned in Section 1.1, various semiconductor photocatalysts have been developed on the d^0 electronic configurations, such as Ti^{4+}, Nb^{5+}, and Ta^{5+}. They were efficient under UV-light irradiation.

TiO_2 was firstly studied for photocatalytic water splitting under UV irradiation [37]. Subsequently, plenty of research has been carried out for water splitting into H_2 or/and $O_2$from pure water or aqueous solutions containing sacrificial reagents under UV irradiation [38-42]. $SrTiO_3$ is another photocatalyst being given intense research interests for water splitting [43-50]. The photocatalytic activity could be enhanced when it was pretreated in H_2 atmosphere and using the dense NaOH solution during the photocatalytic reaction process [48, 49]. Domen *et al.* reported that doping lower valence cation than that of parent cation to intentionally introduce oxygen vacancies and decrease the amount of Ti^{3+} was an effective route to enhance the photocatalytic activity of $SrTiO_3$ [51].

Pt-loaded Nb_2O_5 was highly active for H_2 evolution in the aqueous methanol solution under UV irradiation [52]. Furthermore, mesoporous Nb_2O_5 with larger surface area, which was synthesized by an evaporation-induced self-assembly (EISA) route, showed 20 times higher for photocatalytic H_2 evolution than its bulk phase. On the other hand, lots of efficient oxides based on Nb were also developed to decompose water by using UV light. For example, single crystal $Sr_2Nb_2O_7$ nanoribbon and $SrNb_2O_6$ nanorod synthesized through a facile hydrothermal route exhibited highly efficient photocatalytic activity for H_2 and O_2 evolution

from pure water under UV-light irradiation [53]. It was found that the quantum efficiency was as high as 32% under the irradiation of a 200 W Hg-Xe lamp.

Tantalum oxides have been given intense research efforts due to their photocatalytic activity of H_2 evolution from water under UV-light irradiation. Individual bulk Ta_2O_5 showed very low photocatalytic activity for pure water splitting [54]. However, nanostructure and mesoporous Ta_2O_5 are efficient photocatalysts for H_2 from ethanol or methanol aqueous solution without any cocatalyst under UV irradiation [55-58]. Furthermore, mesoporous Ta_2O_5 is highly active for pure water splitting into H_2 and O_2 when modified with NiO as cocatalyst under UV irradiation [59-61]. Crystallized and fluorinated nanoporous Ta_2O_5 spheres showed higher photocatalytic hydrogen production than P25 and commercial Ta_2O_5 from aqueous methanol solution under UV irradiation [62]. This excellent activity resulted from the large surface area, accessible nanoporous structure, crystallized phase, and surface fluorination.

Many other oxide photocatalysts based on d^{10}electronic configurations, such asIn^{3+}, are also active for photocatalytic water decomposition. RuO_2-loaded $AInO_2$ (A = Li, Na) have been developed for overall water splitting [63]. However, $LiInO_2$ showed little activity under Hg-Xe lamp illumination, $NaInO_2$ was active for photocatalytic pure water splitting into H_2 and O_2. It was also found that the substitution of Na^+ by Li^+ sharply decreased the photocatalytic activity of $NaInO_2$, whereas the photocatalytic activity was increased with increasing the amount of K^+ substituting Na^+. Inoue *et al.* also studied the photocatalytic activities of overall water splitting by RuO_2-loaded alkaline earth metal and lanthanum indates with an octahedrally coordinated In^{3+} ion [64]. The results showed that highly dispersed RuO_2 particles combined with well-crystallized $CaIn_2O_4$ caused high evolution rates of H_2 and O_2 from water under UV irradiation. $RuO_2/SrIn_2O_4$ also showed photocatalytic activity for overall water splitting, whereas RuO_2-dispersed

$LaInO_3$ showed much lower photoactivity. The further research on $SrIn_2O_4$ by Inoue *et al.* explained the better photoactivity for overall water splitting. They found that the distorted InO_6 octahedra with dipole moment and the highly dispersed conduction band consisting of In5*s*5*p* orbitals promoted the separation and migration ability of the photoexcited electrons and holes [65].

To efficiently utilize the solar energy, it is necessary to make wide-band-gap photocatalysts sensitive to visible light. Doping is an effective route to fulfill this aim [66]. In 2001, Asahi *et al.* found that N was an effective nonmetal doping into TiO_2 and widened its light absorption to visible-light range [67]. The bandgap of TiO_2 was narrowed by the mixed *p* states of N and 2*p* states of O. Then, water splitting was carried out under visible-light irradiation using this special photocatalyst synthesized by various methods [68, 69]. Other nonmetal elements were also doped into the pure TiO_2 for water splitting under visible-light irradiation, such as C [70], F [71], and S [72]. Cr-doped $SrTiO_3$ showed high photocatalytic activity for H_2 evolution under visible-light irradiation in aqueous solution containing a sacrificial reagent [73, 74]. Reunchan *et al.* claimed the effect of Cr substitution for Ti (Cr_{Ti}) on the photocatalytic activity of Cr-doped $SrTiO_3$ using hybrid density-functional calculations [75]. The singly negative Cr_{Ti} is relevant to a lower oxidation state of Cr and advantageous for the visible-light absorption without forming electron trapping centers. A series of cubic $SrTi_xM_{1-x}O_3$ (M = Ru, Rh, Ir, Pt, Pd) nanoparticles were synthesized by a hydrothermal method, of which Rh-doped $SrTiO_3$ showed the highest H_2 evolution rate under visible-light irradiation [76]. The results obtained from density functional theory calculations showed that the better photocatalytic activity was caused by its suitable band energetics, and the hybridized Ti/Rh orbitals in the bandgap of $SrTiO_3$.

Developing nondoping and visible-light-sensitive photocatalysts is another hot research topic. Many heterometallic oxides have been successfully synthesized by using metal-mediated band structure engineering.

Indium is a *p*-block transitional metal, many oxides based on it were effective for water splitting under visible-light irradiation. For these oxides, the top of valence band was constructed from O 2*p* orbitals, and the bottom of conduction band was constructed from In 5*s*5*p* orbitals. Thus, the visible-light absorption was attributed to the photoexcitation from the O 2*p* to the In 5*s*5*p* orbitals. Kudo *et al*. reported $In_2O_3(ZnO)_m$ with laminal structure showed photocatalytic activities for H_2 or O_2 evolution under visible-light irradiation in the methanol aqueous solution or silver nitrate aqueous solution[77], respectively. NiO_x loaded $InNbO_4$ and $InTaO_4$ showed photocatalytic H_2 evolution from pure water under visible-light irradiation [78]. For these two oxides, there are two kinds of octahedral, InO_6 and MO_6 (M = Nb, Ta); the valence bands of them should be a combination of both the O 2*p* orbitals of the InO_6 and MO_6 octahedrons [78-80].

For most metal oxide photocatalysts, they are only responsive to UV light. It is not beneficial to the efficient utilization of solar energy. Though some metal oxides are visible-light-responsive photocatalysts, there is much space for the improvement of energy-conversion-efficiency.

1.2.2 Metal sulfide photocatalysts

The valence bands of metal sulfides are usually composed of S 3*p* orbitals, which are less positive than O 2*p* orbitals and thus make most of the metal sulfides sensitive to visible-light. Although sulfides suffer from photocorrosion, it can be suppressed by using S^{2-}/SO_3^{2-} as the scavenger of holes.

CdS (E_g = 2.4 eV) is a very famous sulfide photocatalyst for H_2 evolution in S^{2-}/SO_3^{2-} aqueous solution under visible-light irradiation [81-87]. CdS is also a potential candidate for the conversion of H_2S into H_2 and S [88], which is beneficial from both environmental and energy standpoints. When CdS was modified by some other appropriate sulfides as cocatalysts, such as NiS [89] and MoS [90], the H_2 evolution rate was greatly enhanced from lactic acid sacrificial solution under visible-light irradiation, which was even higher than that of noble-metal-loaded CdS. When CdS was co-loaded with Pt and PdS, the quantum efficiency can achieve as high as 93% at 420 nm for H_2 evolution in S^{2-}/SO_3^{2-} aqueous solution under visible-light irradiation [28].

Many ternary or multicomponent metal chalcogenides were developed for photocatalytic H_2 evolution under visible-light irradiation. The $ZnIn_2S_4$ synthesized by a hydrothermal method showed good photostability for H_2 evolution in S^{2-}/SO_3^{2-} aqueous solution [91], the conduction band of it was constructed from In 5*s* orbital, which narrowed the bandgap to be sensitive to visible light. Shen *et al.* studied the effects on the photocatalytic activities of $ZnIn_2S_4$ by loading different transition-metal sulfides [92]. They found that CoS, NiS, or MnS-loading lowered down the photocatalytic activity of $ZnIn_2S_4$, while Ag_2S, SnS or CuS loading enhanced the photocatalytic activity. They also studied the effects of different transition metals (Cr, Mn, Fe, Co) doping on the photocatalytic activity of $ZnIn_2S_4$ [93]. It was found that Cr-, Fe-, and Co-doped $ZnIn_2S_4$ performed poorer photocatalytic activities, while Mn-doped $ZnIn_2S_4$ enhanced the photocatalytic activities.

Many other metal sulfides have also been studied. Cubic spinel $CdIn_2S_4$ with a fascinating marigold-like morphology was firstly synthesized by hydrothermal method [94]. It exhibited high photocatalytic activity for H_2 evolution from H_2S aqueous solution under visible-light irradiation. A p-type bulk $AgGaS_2$ was also fabricated by a solid-state method route for H_2 evolution under visible-light irradiation [95]. When indium was substituted at

gallium site in chalcopyrite $AgGaS_2$, the band gap energy of $AgGa_{1-x}In_xS_2$ was tailored by the In 5s orbitals, and accordingly the photocatalytic activity of $AgGa_{1-x}In_xS_2$was modified [96]. Kudo *et al.* found that $NaInS_2$ with layered structure also showed photocatalytic activity for H_2 evolution from an aqueous K_2SO_3 solution under visible-light irradiation [97]. Zheng *et al.* fabricated $CuInS_2$ with enhanced photocatalytic activity under visible-light irradiation [98]. Tabata *et al.* developed $CuGa_3S_5$ with a band gap of 2.4 eV [99]. It showed photocatalytic H_2 evolution activity even without a cocatalyst under visible-light irradiation from Na_2S/Na_2SO_3 aqueous solution. Kale *et al*. reported a new ternary chalcogenide material $CdLa_2S_4$ with different morphologies [100]. This photocatalyst showed high efficient H_2 evolution under visible-light irradiation from the KOH solution with a H_2S flow. Graphene-like Cu_2ZnSnS_4 nanosheets were firstly prepared and showed high photocatalytic activity for H_2 evolution from aqueous solution containing S^{2-}/SO_3^{2-} without loading any noble metal [101].

Most metal sulfides are attractive candidates for photocatalytic water splitting into H_2 under visible-light irradiation. However, it is also necessary to develop metal sulfide photocatalysts which are high efficient, low cost, and nontoxic.

1.2.3 Oxysulfide photocatalysts

The valence bands of oxysulfides were mainly constructed by S 3*p* orbitals with partial attribution of O 2*p* orbitals [102] and the S 3*p* orbitals are located at a less positive position than those of O 2*p* orbitals. This makes oxysulfides narrower bandgaps being sensitive to visible light, which was also supported by the theoretical calculation [103].

In 2002, Ishikawa *et al.* found that$Sm_2Ti_2S_2O_5$ was a stable visible-light-sensitive photocatalyst for not only H_2 evolution in the Na_2S/Na_2SO_3 aqueous solution, but also for O_2 evolution from the $AgNO_3$ aqueous solution [104]. The electrochemical measurements indicated that the conduction and valence bands' positions were enough for the reduction of

H^+ to H_2 and the oxidation of H_2O to O_2 at pH = 8. They also developed a new method to synthesize $Sm_2Ti_2S_2O_5$ at lower temperature for shorter time [105]. Subsequently, Zhang *et al.* modified $Sm_2Ti_2S_2O_5$ and $Gd_2Ti_2S_2O_5$ with nanoparticulate Rh (reduction site) and Ag_2S (oxidation site) [106]. The modification greatly enhanced their photocatalytic H_2 evolution rate from water containing Na_2S and Na_2SO_3. They also studied the effects of metal modification on its photocatalytic activities [107]. It was found that the simultaneous addition of 5% Mg and 1% Ag produced the highest level of catalytic performance for H_2 evolution. Their further research showed that $Sm_2Ti_2S_2O_5$ modified with 1 wt% Ag and 1 wt% Rh was more efficient for photocatalytic H_2 evolution [108].

Lanthanide-based oxysulfides $LnTaO_{3.5}S_{0.5}$ were also fabricated by sulfurization in a flowing H_2S [109]. These oxysulfides were also sensitive to visible-light due to the formation of occupied S 3*p* orbitals on the top of valence band. They showed photocatalytic H_2 evolution activity from Na_2S/Na_2SO_3 aqueous solution. Ishikawa *et al*. synthesized a series $Ln_2Ti_2S_2O_5$ (Ln = Pr, Nd, Sm, Gd, Tb, Dy, Ho and Er) [110]. These photocatalysts could split water into H_2 or O_2 under visible-light irradiation from the solution containing Na_2S/Na_2SO_3 or Ag^+. Ogisu *et al*. developed Lanthanum-Indium oxysulfide as a visible-light-driven photocatalyst for water splitting [111]. The photocatalyst loaded with IrO_2 was effective for promoting O_2 evolution, while Pt was effective for H_2 evolution.

Oxysulfides are novel photocatalysts due to their oxidation ability to produce O_2 from water. However, the energy-conversion-efficiency should be further improved.

1.2.4 Metal-(oxy)nitride photocatalysts

GaN (E_g = 3.4 eV) and Ge_3N_4 (E_g =3.6 eV) are UV-light-sensitive photocatalysts [102]. Ge_3N_4 loaded with RuO_2 could stoichiometrically split pure water into H_2 and O_2 [112]. However, N_2 was also detected indicating the degradation of the nitride photocatalyst. The

photocatalytic activity was enhanced and simultaneously N_2 release was remarkably reduced by increasing the crystallinity of Ge_3N_4 [113]. It was also found that the photocatalytic activity of RuO_2/Ge_3N_4 for overall water splitting strongly depended on the concentration of H_2SO_4 in the reaction solution and the pressure of gaseous oxygen [114]. GaN, with a conduction band edge which is 0.5 V higher than the redox potential of H^+/H_2, could decompose water into H_2 without cocatalyst in a solution containing hole scavenger (Na_2S-Na_2SO_3, CH_3OH)[115]. $Rh_{2-y}Cr_yO_3$ modified GaN with well crystallinity was capable to overall water splitting [116]. Ta_3N_5, a novel photocatalyst responding to visible light, was found to be able to split water into H_2 or O_2 in a solution containing methanol or $AgNO_3$ [117].Ta_3N_5 was still fabricated as photoanode, which was used for water splitting under visible-light irradiation [118, 119].

In comparison with Ta_2O_5, the bottom of conduction band of TaON mainly consisted of Ta 5*d* orbitals, while the top of valence band consisted of the hybridized orbitals of N 2*p* and O 2*p* [120] based on the DFT calculation. According to the calculation, it was considered that the potential of the bottom of the conduction band kept at the same level of the corresponding oxide, but the top of the valence band shifted to a less positive position than that of the oxide. This difference in valence band resulted in the narrower band gap of TaON, however, showing enough potential for water splitting under visible-light irradiation [121]. A series of Ta-based oxynitrides, $ATaO_2N$ (A = Ca, Sr, Ba) were also fabricated by heating amorphous $A_2Ta_2O_7$. Pt-loaded $CaTaO_2N$ and $BaTaO_2N$ were active for H_2 evolution in an aqueous solution containing methanol or I^- as the electron donor under visible-light irradiation, whereas $SrTaO_2N$ was not active due to its oxidative decomposition [122]. Nb-based oxynitrides, such as $CaNbO_2N$, $SrNbO_2N$, $BaNbO_2N$, and $LaNbON_2$, showed H_2 or O_2 evolution under visible-light irradiation from a methanol or $AgNO_3$ aqueous solution [123], respectively.

Metal nitrides and metal oxynitrides are efficient photocatalysts for water splitting. However, the stability of them should be improved.

1.2.5 Nonmetal photocatalysts

Carbon nitride (g-C_3N_4), a metal-free polymeric photocatalyst, was fabricated by thermal condensation. It was stable and efficient for H_2 or O_2 evolution from water containing sacrificial reagents under visible-light irradiation [124]. The graphitic planes consisted of tri-s-triazine unites linked by planar amino groups as shown in Figure 1.4 (a). The XRD pattern and UV-vis absorption spectrum of C_3N_4 were shown in Figure 1.4 (b) and (c), respectively.

The band gap of the C_3N_4 was estimated to be 2.7 eV. The electronic and optical properties of carbon nitride are adjustable by organic protocols in principle. Zhang *et al.* extended the absorption up to about 750 nm by simple copolymerization with barbituric acid (BA) [125]. Carbon nitride with porous structures showed enhanced photocatalytic activity for H_2 evolution under visible-light irradiation [126, 127]. When the C_3N_4 was doped with S

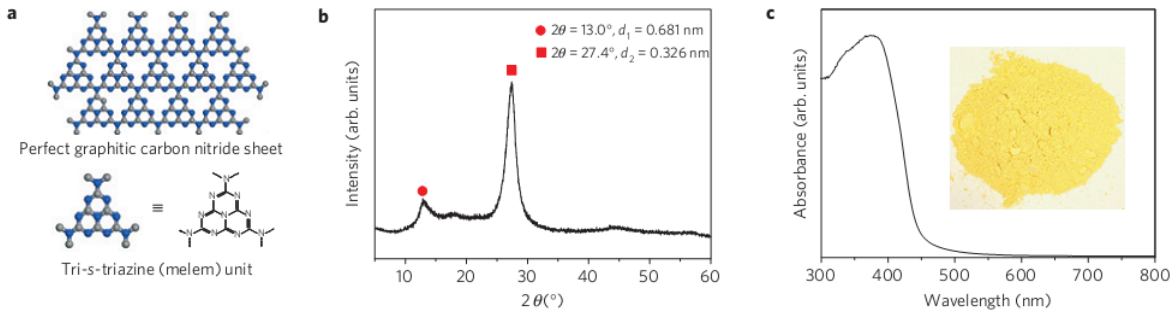

Figure 1.4 (a) Schematic pictures of a perfect graphitic carbon nitride sheet constructed from melem units, (b) XRD pattern of the polymeric carbon nitride, (c) UV-vis absorption spectrum of the polymeric carbon nitride. Inset: A photograph of the as-synthesized carbon nitride. Reproduced from ref. [124].

[128, 129] or C [130], its photocatalytic H_2 evolution rate was also promoted under visible-light irradiation.

C_3N_4 is interesting as a nonmetal photocatalyst. Further efforts should be given to enhance its photocatalytic activity.

1.2.6 Composite photocatalysts

The semiconductor composites have been given intense research interests for photocatalytic reactions due to the better separation of photoexcited carriers at the interface of components. Especially, the separation ability of photoexcited electrons and holes is more strongly required for water splitting than for the photocatalytic reactions in the presence of sacrificial reagents to inhibit the recombination of photoexcited carriers [131]. Usually, for n-type/n-type semiconductor composites, the charges transfer is simple, the more negative photoexcited electrons move to the less negative conduction band, while the more positive photoexcited holes move to the less positive valence band. However, for p-n junction semiconductor composites, the transfer of photoexcited charges depends on the appropriate match of energy edges of the components as shown Figure 1.5. There is an internal field with a direction from the n-type semiconductor to the p-type semiconductor at the thermodynamic equilibrium state [132]. In the view of band energy, Figure 1.5 (a) is the best appropriate one for photocatalytic composite, the excited electrons of the p-type semiconductor transfer to the conduction band of the n-type semiconductor, and simultaneously the holes of the n-type semiconductor transfer to the valence band of the p-type semiconductor. This process greatly reduces the recombination and accordingly enhances the photocatalytic activity. The second case in Figure 1.5 (b) is favorable to the separation of photoexcited holes by transferring them from the n-type semiconductor to the p-type semiconductor easily. However, the electrons can’t transfer from the n-type semiconductor to the p-type semiconductor, because it was

blocked by the internal electric fields constructed by the p-n junction. The third case in Figure 1.5 (c) is not beneficial to the separation of charges due to the block of internal electric field.

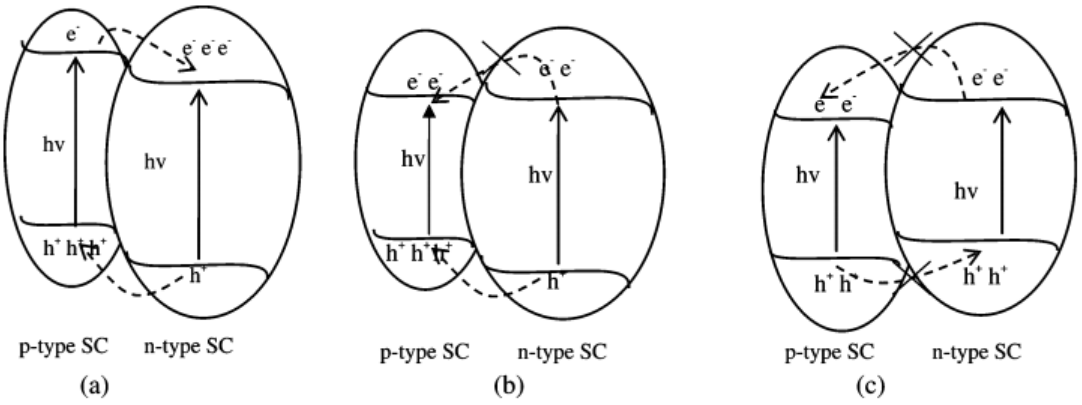

Figure 1.5 Schematic principle of charge separation of p-n junction semiconductor composites under light irradiation. Reproduced from ref. [132].

TiO_2 is an interesting photocatalysts for H_2 evolution, however, under UV-light irradiation. Well-crystallized TiO_2 with a high surface area, high separation and migration abilities of photoexcited charges are necessary to efficiently use solar energy. TiO_2/semiconductor composites are proved to be effective for enhanced H_2 or O_2 evolution under UV-light irradiation [131, 133,134]. Figure 1.6 shows the charge separation in $TiO_2/SrTiO_3$ heterojunction. Interestingly, CdS was also a sensitizer being sensitive to visible light for water splitting in CdS/TiO_2 composite [135, 136]. TiO_2 coupled with grapheme [137], carbon nanotube [138], or MoS_2 and grapheme [139] showed highly promotion in photocatalytic H_2 evolution rate due to the enhanced separation ability of the photoexcited charges. In 2008, Zhang *et al.* fabricated a phase junction formed between the surface anatase nanoparticles and rutile particles, and this junction greatly enhanced the photocatalytic activity for H_2 evolution [140].

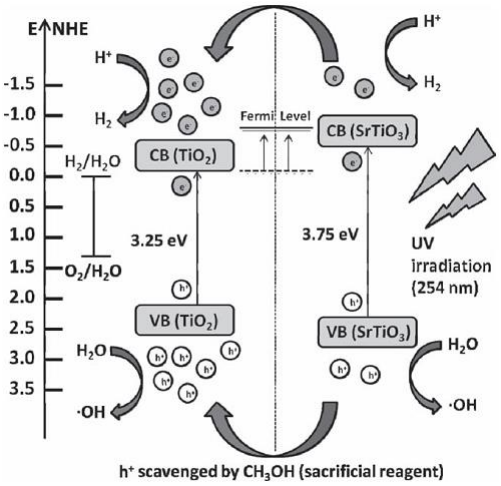

Figure 1.6 Schematic diagram for the respective band positions (pH = 1) and spatial separation of photoexcited charges. Reproduced from ref. [131].

Because of the fact that the semiconductor composites can truly improve the separation and migration ability of the photoexcited charges, which accordingly enhance the photocatalytic activity, many other semiconductor composites have been synthesized for photocatalytic water splitting. Wang *et al.* synthesized Cr-doped $Ba_2In_2O_5/In_2O_3$ oxide semiconductor composite with enhanced activity for water splitting by a solid-state reaction method [141]. The composite system with compatible band edges suitable for H_2 and O_2 evolution was assumed to be bridged properly by an ohmic contact, which was advantageous in photoinduced charge carrier separation and migration. Figure 1.7 shows the typical excitation, separation, and migration and redox reactions for H_2 and O_2 evolution in the composite. The composite loaded with Pt was active for H_2 evolution from aqueous methanol solution under visible-light irradiation, and it was also active for overall water splitting under UV-light irradiation by loading with NiO. $In_2O_3/NaNbO_3$ also showed enhanced photocatalytic activity for H_2 evolution under visible-light irradiation and pure water splitting under UV-light irradiation [142]. The charge separation was similar to that of Cr-doped $Ba_2In_2O_5/In_2O_3$ oxide composite [141]. Wang *et al.* also found that a Zn-doped

Lu_2O_3/Ga_2O_3composite could split pure water into H_2 and O_2 in stoichiometric ratio under UV-light irradiation [143]. Xu *et al.* fabricated In_2O_3/Ta_2O_5 composites, which showed obviously enhanced photocatalytic activity for H_2 production with a long-term stability under UV-light irradiation [144, 145]. Monoclinic ZrO_2/TaON composite prepared by a surface modification method also showed enhanced photocatalytic activity for H_2 evolution from water under visible-light irradiation [146].

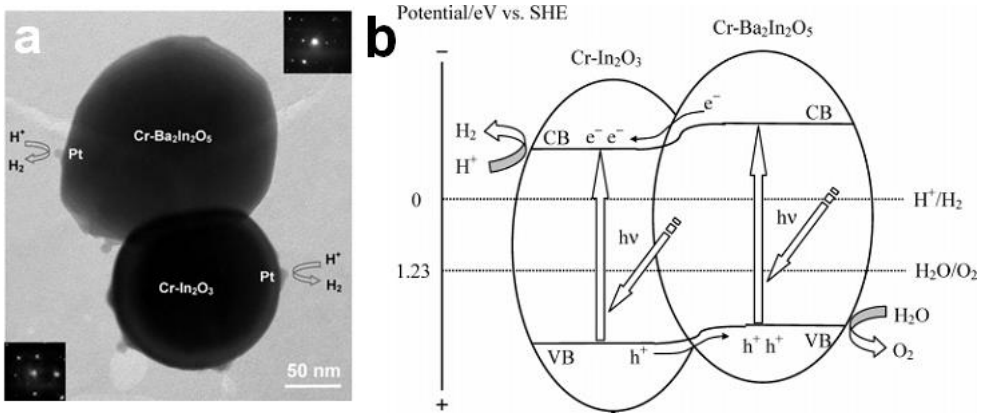

Figure 1.7 (a) Typical TEM images and SAED patterns taken from different particles of the composite loaded with Pt nanoparticles. (b) Schematic diagram for band structures, charge HRTEM image and SAED patterns, and the schematic diagram of the band structures, charge excitation, separation, and migration and redox reactions for H_2 and O_2 evolution. Reproduced from ref. [141].

Trari *et al.* developed a series of p-n junction for water splitting under visible-light irradiation. The p-$CuMO_2$/n-Cu_2O (M = Mn, Cr), p-$CuAlO_2$/n-TiO_2, and p-$CuFeO_2$/n-SnO_2 showed enhanced photocatalytic H_2 evolution activity from water solution containing reducing agents [147-150]. Kim *et al.* synthesized p-$CaFe_2O_4$/n-type $MgFe_2O_4$ bulk heterojunction by a polymer complex (PC) method [151]. This composite was highly active for H_2 evolution from water under visible-light irradiation due to the high separation and

migration ability of the photoexcited charges. Figure 1.8 shows the special structure, band energy, and charge migration of the p-$CaFe_2O_4$/n-$MgFe_2O_4$ bulk composite. In a bulk composite with p- and n-type semiconductors interfacing each other, it is probable that the excited carriers can reach the interface and the dissociation is higher, especially when the domain size of the semiconductor particles is similar to the exciton diffusion length. This could enhance the photocatalytic activity. Sulfide-based p-n junction, such as p-$AgGaS_2$/n-CdS, has also been fabricated by decorating $AgGaS_2$ surface with nanoparticles of CdS through a hydrothermal route [152]. The heterojunction system resulted in an efficient charge separation, and accordingly enhanced the H_2 production under visible-light irradiation.

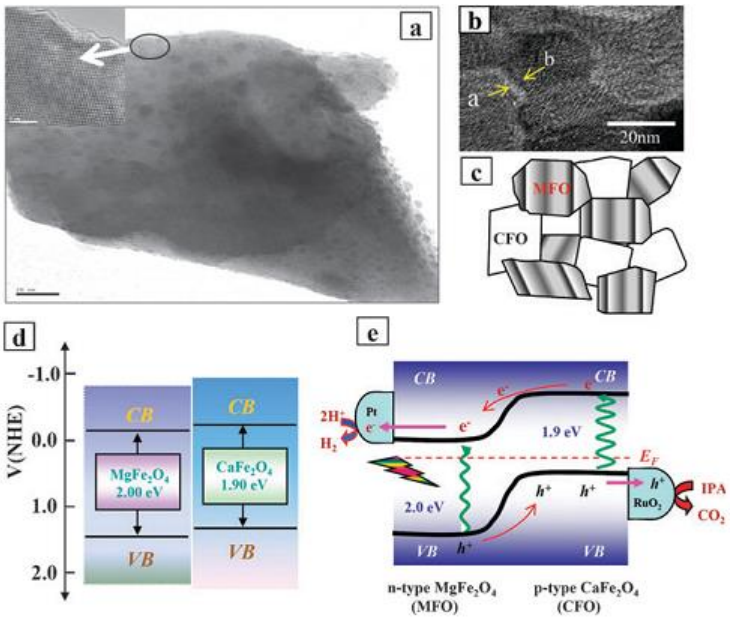

Figure 1.8 (a) A TEM image of $CaFe_2O_4$/$MgFe_2O_4$ composite. (b) A HRTEM image of interfaces between the semiconductor nanoparticles. (c) A schematic structure of $CaFe_2O_4$/$MgFe_2O_4$ composite. (d) A schematic diagram of the band energies of $CaFe_2O_4$ and $MgFe_2O_4$. (e) A schematic diagram of charge separation in $CaFe_2O_4$/$MgFe_2O_4$ composite. Reproduced from ref. [151].

Recently, carbon nitride has been given increasing research interest as a polymer photocatalysis. Many methods were developed to enhance its photocatalytic activities, coupling with other semiconductors is an attractive way based on the previous experience. The g-C_3N_4/CdS composite photocatalysts with various weight ratios of CdS were synthesized by a chemical impregnation route [153]. The composite showed about 8 times higher of photocatalytic H_2 evolution rate under visible-light irradiation than the pure g-C_3N_4. Yan *et al.* also reported a g-C_3N_4/TiO_2 composite that showed remarkably enhanced photocatalytic activity for H_2 evolution under visible light [154]. All the improved photocatalytic activities were caused by the enhanced separation ability of photoexcited electrons and holes.

As mentioned above, composite photocatalysts are efficient for the separation and migration of photoexcited carriers, which is dominated by the contact electronic field. Therefore, it is significant to synthesize composites with good contact and fluent interface between the semiconductor components.

1.2.7 Solid solution photocatalysts

A solid solution between wide and narrow band gap semiconductors is an effective candidate for controlling the band structure of a photocatalyst. Both conduction band and valence band can be adjusted by changing the ratio of the narrow and wide band gap semiconductor in the solid solution.

Wang *et al.* fabricated a series of $(AgNbO_3)_{1-x}(SrTiO_3)_x$ ($0 < x < 1$) solid solutions as visible-light-sensitive photocatalysts for O_2 evolution and decomposition of organic pollutants [155, 156]. In the mixed valent perovskites $(AgNbO_3)_{1-x}(SrTiO_3)_x$, the hybridization between the Ag 4*d* and O 2*p* orbitals and between the Nb 4*d* and Ti 3*d* orbitals

play a significant role in tuning the energy band structure (band gap, band edge, and bandwidth, etc.) and, thus, in adjusting the photophysical and photocatalytic properties.

Oxynitride solid solutions are also important candidates for water splitting under light irradiation. The narrowed band gaps usually can be adjusted by both lowering the bottom of the conduction band and raising the top of the valence band. Luo *et al.* developed $(SrTiO_3)_{1-x}\cdot(LaTiO_2N)_x$ by a thermal ammonolysis method [157]. Its band gaps linearly reduced from 3.18 to 2.04 eV with increasing x from 0 to 0.30. The solid solution showed photocatalytic H_2 or O_2 evolution activity from aqueous solution containing sacrificial reagents under visible-light irradiation. In 2005, Domen *et al.* developed GaN-ZnO solid solutions as potential candidates for overall water splitting under visible-light irradiation [27]. Each component, GaN or ZnO, is UV-light-sensitive semiconductor (E_g > 3.0 eV), the visible-light-sensitive ability of the solid solution results from the *p-d* repulsion of Zn 3*d* and N 2*p* orbitals in the valence band [158, 159], which shifts the top of the valence band upward without changing the conduction band. Thus, the potentials of conduction and valence bands are suitable to overall water splitting under visible-light irradiation. When $Rh_{2-y}Cr_yO_3$ was loaded on the surface of GaN-ZnO solid solution as the cocatalyst, the photocatalytic activity was greatly enhanced because of the reducement of recombination of photoexcited charges and backward reaction from H_2 and O_2 to H_2O [160-163].

Based on the successful development of GaN-ZnO solid solution, Domen's group subsequently developed $(Zn_{1+x}Ge)(N_2O_x)$ constructed by $ZnGeN_2$ and ZnO components [164-167], which was another active and stable photocatalyst for overall water splitting under visible-light irradiation. The band gap of this kind of solid solution decreases slightly with increasing zinc content, attributable to *p-d* repulsion between Zn 3*d* and N 2*p* + O 2*p* electrons in the upper valence band, which raises the top of the valence band. The activity of $Rh_yCr_{2-y}O_3$-loaded $(Zn_{1+x}Ge)(N_2O_x)$ photocatalyst for over all water splitting under visible-

light irradiation was enhanced by calcination in N_2. The apparent quantum efficiency achieved 2.0% at 420-440 nm. The improvement of photocatalytic activity was caused by the decrease of defects acting as the recombination centers for photogenerated electrons and holes [166].

The solid solutions based on metal sulfides are also attractive candidates for water splitting under visible-light irradiation. $Zn_{1-x}Cd_xS$ solid solution was ever synthesized by a coprecipitation method [168, 169]. It showed photocatalytic activity for H_2 evolution under visible-light irradiation even without noble metal as cocatalyst. Recently, the photocatalytic activity of this photocatalyst was greatly enhanced by special morphologies synthesized through new fabrication methods [170, 171]. $Cd_{1-x}Zn_xS$ solid solution with nano-twin structures exhibited superior photocatalytic activities for H_2 evolution from water under visible-light irradiation without noble metal cocatalyst. The “back to back” potential formed by parallel nano-twins in the $Cd_{1-x}Zn_xS$ crystals significantly improved the separation of the photogenerated electrons and holes as shown in Figure 1.9. Nanoporous $Zn_{1-x}Cd_xS$ solid solutions were synthesized by a simple aqueous route at room temperature. The photocatalytic activity depended on the compositions varying the band gap energy.

Kudo and co-workers have developed many solid solutions based on ZnS and other sulfides (e. g., $CuInS_2$, $AgInS_2$) with narrow band gaps [172-175]. The band gaps of the solid solution were controllable by changing the composition. The band edges are linear to the composition. The solid solutions showed high photocatalytic H_2 evolution from aqueous solutions containing sacrificial reagents, SO_3^{2-} and S^{2-}, under visible-light irradiation even without Pt as the cocatalyst. However, the H_2 evolution rate was highly enhanced after loading Pt as the cocatalyst. Subsequently, ZnS-$CuInS_2$-$AgInS_2$ solid solution was developed

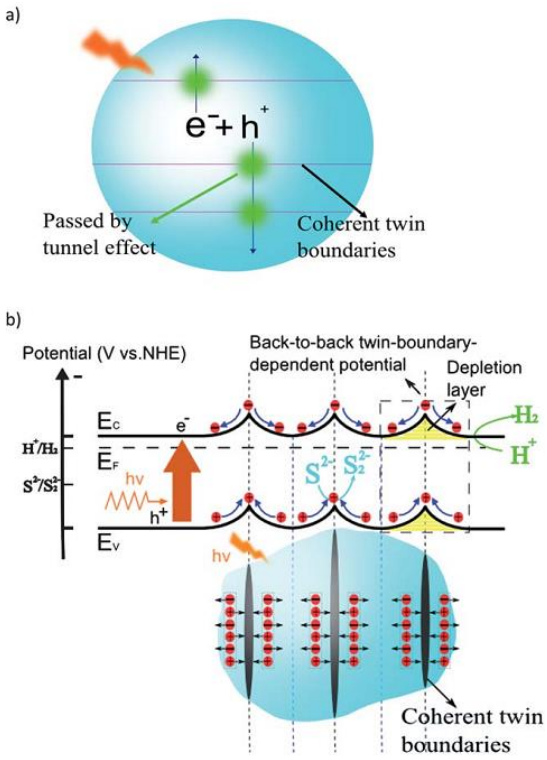

Figure 1.9 The migration of free charges and photocatalytic H_2 evolution from an aqueous solution over nano-twin $Cd_{0.5}Zn_{0.5}S$ crystals. a) Free charges pass through single atom layer boundaries without being trapped or scattered. b) Parallel boundaries provided twin-boundary-dependent potential which derived the "back to back" Schottky barrier and would control the migration of free charges. Reproduced from ref. [170].

as an active visible-light-sensitive photocatalyst [176, 177]. It was found that the ZnS-$CuInS_2$-$AgInS_2$ solid solution showed a higher photocatalytic H_2 evolution activity under the irradiation from a solar simulator in comparison with those of ZnS-$MInS_2$ (M = Cu or Ag) solid solutions. This enhanced activity probably resulted from the longer absorption bands in wavelength due to interactions between the Cu 3*d* and Ag 4*d* orbitals.

In 2010, Kudo *et al.* synthesized another series of stannite-type complex sulfides A^I_2-Zn-A^{IV}-S_4 (A^I= Cu and Ag; A^{IV} = Sn and Ge) for photocatalytic H_2 evolution under visible-light irradiation [178]. Diffuse reflection spectra and the plane-wave-based density functional

theory (DFT) calculation suggested that the conduction bands were constructed by Ge 4*s*4*p* or Sn 5*s*5*p* with S 3*p* orbitals, while the valence bands consisted of Cu 3*d* and Ag 4*d* with S 3*p* orbitals. Then they developed $AGa_2In_3S_8$ (A =Cu or Ag) with layered structures [179]. $CuGa_2In_3S_8$ with a 1.91-eV band gap and $AgGa_2In_3S_8$ with a 2.27-eV band gap showed 15% apparent quantum yields at 560 nm and 460 nm for H_2 evolution from aqueous solutions containing K_2SO_3 and Na_2S as sacrificial reagents using Rh as the cocatalyst.

Chen's group fabricated nanoporous ZnS-In_2S_3-Ag_2S and ZnS-In_2S_3-CuS solid solutions by a simple template-free route [30, 31]. Both of them showed high photocatalytic activities for H_2 evolution under visible-light irradiation without any cocatalyst from aqueous solutions containing SO_3^{2-} and S^{2-} as electron donors. The apparent quantum yields were 19.8% and 22.6% at 420 nm, respectively.

Solid solution photocatalysts can effectively adjust the band gaps and are efficient candidates for photocatalytic reactions. However, it is also necessary to develop simpler and more effective route to synthesize more efficient photocatalysts. On the other hand, it is still significant to develop photocatalysts based on cheap and nontoxic elements.

1.3 The significance and research topics of this thesis

Now we are facing increasing energy crisis and environmental pollutions, and decreasing levels of fossil fuels. It is urgent for researchers to develop clean and renewable energy. H_2 is regarded as an ideal energy candidate in future due to its high energy density and pollution-free combustion product. Photocatalysts are excellent candidates for solar energy conversion into H_2 by water splitting. As mentioned above, in the view of efficient utilization of solar energy, a photocatalytst should be sensitive to visible light, because it takes about 43% of the total solar energy. Furthermore, efficient separation and migration of the photoexcited electrons and holes are crucial to an efficient photocatalyst. It has been proved by many reports that appropriate semiconductor composites are beneficial to the effective separation and migration of the photoexcited charges. Thus, developing semiconductor composites is a significant means to achieve highly efficient photocatalysts. On the other hand, nanostructured photocatalysts are also effective photocatalysts because the photoexcited charges cover a short distance to reach the photocatalysts' surface and there are much active sites creating by the large surface area for redox reactions. Both of them facilitate the enhanced photocatalytic activity. Up to now, there is little systematic research about the composite and nanostructured photocatalysts based on Zn/In elements for photocatalytic water splitting. In this thesis, I devoted in the development of efficient and visible-light-sensitive Zn/In-based semiconductor composites and nanocrystallines for H_2 evolution from water. The detailed research topics are shown as follows.

$Zn_5In_2O_8$ is sensitive to visible light and there are few reports about its photocatalytic activities. As mentioned in Chapter 1.2.3, the S 3*p* orbitals can lift up the top of valence bands of metal oxides. On the other hand, surface vacancies significantly affect the crystal growth, especially in the weak driving force regime [180]. In Chapter 2, $Zn_5In_2O_8$ was firstly fabricated and subsequently further treated to produce vacancy-rich $Zn_5In_2O_8$ in NaCl/KCl

molten-salt. Then, a $Zn_5In_2O_8$/surface-S-doped $Zn_5In_2O_8$ composite was fabricated through *in situ* sulfuration of the vacancy-rich $Zn_5In_2O_8$ in Na_2S/K_2SO_3 aqueous solution under light irradiation emitted from a 300 W Xe lamp. This composite was desired to show tight contact interface, and accordingly enhance the photocatalytic activity.

In_2S_3 and $ZnIn_2S_4$ can utilize more visible light due to their narrower band gaps than that of $Zn_5In_2O_8$. On the other hand, the bulk composite shows tight contact and fluent interface, and homogeneous distribution of the components. These merits are more beneficial to the more efficient separation and migration of the photoexcited electrons and holes than traditional composites. In Chapter 3, $In_2S_3/ZnIn_2S_4$ bulk composites were synthesized by an ion-exchange route using $ZnCl_2$ and $MgCl_2·6H_2O$ as the ion-exchange reagents, and using $NaInS_2$ as the precursor. The $In_2S_3/ZnIn_2S_4$ bulk composite are desired to show higher photocatalytic activities than $Zn_5In_2O_8$/surface-S-doped $Zn_5In_2O_8$ composite.

The conduction band bottom of ZnS consists of Zn 4*s*4*p* orbitals which are more negative than In 5*s*5*p* orbitals. In the view of thermodynamics, ZnS shows stronger reduction ability for photocatalytic H_2 evolution than In_2S_3 and $ZnIn_2S_4$, because In 5*s*5*p* orbitals construct the conduction band bottoms of In_2S_3 and $ZnIn_2S_4$. ZnS can reduce H_2O into H_2 even without cocatalyst, however, under UV light. In order to make ZnS sensitive to visible light, Cu^{2+} doping is an effective route by lifting up the top of valence band. Usually, Cu^{2+} was doped into ZnS by a coprecipitation route. This method was hard to make Cu^{2+} totally and evenly doped because of the greatly different solubility products of ZnS and CuS. Therefore, it is significant to develop new routes to synthesize homogeneous Cu^{2+} dopant in ZnS. In Chapter 4, a complexing-wet-chemical method was developed to synthesize ultrafine $Zn_{1-x}Cu_xS$ ($0.018 \leq x \leq 0.066$) nanocrystallines. These materials were desired to show high photocatalytic activity for H_2 evolution under visible-light irradiation without cocatalyst.

References

[1] Fujishima A and Honda K 1972 *Nature***238** 37.

[2] Hsiao C Y, Lee C L and Ollis D F 1983 *J. Catal.***82**418.

[3] Pruden A L and Ollis D F 1983 *J. Catal.***82**404.

[4] Childs L P and Ollis D F 1980 *J. Catal.***66**383.

[5] Blake DM (ed.), Bibliography of Work on Heterogeneous, Photocatalytic Removal of Hazardous Compounds, (US Department of Energy, Golden Colorado, 1995).

[6] Wang R, Hashimoto K, Fujishima A, Chikuni M, Kojima E, Kitamura A, Shimohigoshi M and Watanabe T 1997 *Nature***388** 431.

[7] Hashimoto K, Irie H and Fujishima A 2005 *Jpn. J. Appl. Phys.***44** 8269.

[8] Ouyang S X, Zhang H T, Li D F, Yu T, Ye J H and Zou Z G 2006 *J. Phys. Chem. B***110** 11677.

[9] Tong H, Umezawa N and Ye J H 2011 *Chem. Commun.* **47** 4219.

[10] Wagner F T and Somorjai G A 1980 *Nature* **285** 559.

[11] Sayama K and Arakawa 1993 *J. Phys. Chem.* **97** 531.

[12] Ding Q P, Yuan Y P, Xiong X, Li R P, Huang H B, Li Z S, Yu T, Zou Z G and Yang S G 2008 *J. Phys. Chem. C* **112** 18846.

[13] Chen D and Ye J H 2009 *Chem. Mater.* **21** 2327.

[14] Kato H, Asakura K and Kudo A 2003 *J. Am. Chem. Soc.* **125** 3082.

[15] Ikeda S, Itani T, Nango K and Matsumura M 2004 *Catal. Lett.* **98** 229.

[16] Ouyang S X, Kikugawa N, Zou Z G and Ye J H 2009 *Appl. Catal., A: General* **366** 309.

[17] Ouyang S X, Kikugawa N, Chen D, Zou Z G and Ye J H 2009 *J. Phys. Chem. C* **113** 1560.

[18] Li X K, Ouyang S X, Kikugawa N and Ye J H 2008 *Appl. Catal., A: General* **334** 51.

[19] Tang J W, Zou Z G and Ye J H 2004 *Angew. Chem. Int. Ed.* **43** 4463.

[20] Ye J H, Zou Z G and Matsushita A 2003 *Int. J. Hydrogen Energy* **28** 651.

[21] Zou Z G, Ye J H and Arakawa H 2002 *J. Phys. Chem. B* **106** 13098.

[22] Ye J H, Zou Z G, Oshikiri M, Matsushita A, Shimoda M, Imai M and Shishido T 2002 *Chem. Phys. Lett.* **356** 221.

[23] Zou Z G, Ye J H, Sayama K and Arakawa H 2001 *Nature* **414** 625.

[24] Kako T, Zou Z G, Katagiri M and Ye J H 2007 *Chem. Mater.* **19**198.

[25] Xue H, Li Z H, Dong H, Wu L, Wang X X and Fu X Z 2008 *Cryst. Growth Des.* **8** 4469.

[26] Kako T, Kikugawa N and Ye J H 2008 *Catal. Today* **131** 197.

[27] Maeda K, Teramura K, Lu D L, Takata T, Saito N, Inoue Y and Domen K 2006 *Nature* **440** 295.

[28] Yan H J, Yang J H, Ma G J, Wu G P, Zong X, Lei Z B, Shi J Y and Li C 2009 *J. Catal.* **266** 165.

[29] Arai T, Senda S, Sato Y, Takahashi H, Shinoda K, Jeyadevan B and Tohji K 2008 *Chem. Mater.* **20** 1997.

[30] Li Y X, Chen G, Zhou C and Sun J X 2009 *Chem. Commun.* **15** 2020.

[31] Li Y X, Chen G, Wang Q, Wang X, Zhou A K and Shen Z Y 2010 *Adv. Funct. Mater.* **20** 3390.

[32] Yu Y F, Zhang J, Wu X, Zhao W W and Zhang B 2012 *Angew. Chem. Int. Ed.* **51** 897.

[33] Zhang J, Yu J G, Zhang Y M, Li Q and Gong J R 2011 *Nano Lett.* **11** 4774.

[34] Yi Z G, Ye J H, Kikugawa N, Kako T, Ouyang S X, Stuart-Williams H, Yang H, Cao J Y, Luo W J, Li Z S, Liu Y and Withers R L 2010 *Nat. Mater.* **9** 559.

[35] Kudo A, Omori K and Kato H 1999 *J. Am. Chem. Soc.* **121** 11459.

[36] Grätzel M 1989 *Hetrogeneous Photochemical Electron Transfer*; CRC Press: Boca Raton, FL.

[37] Schrauzer G N and Guth T D 1977 *J. Am. Chem. Soc.* **99** 7189.

[38] Kudo A, Domen K, Maruya K and Onishi T 1987 *Chem. Phys. Lett.* **133** 517.

[39] Duonghong D, Borgarello E and Grätzel M 1981 *J. Am. Chem. Soc.* **103** 4685.

[40] Tabata S, Nishida H, Masaki Y and Tabata K 1995 *Catal. Lett.* **34** 245.

[41] Shi J Y, Chen J, Feng Z C, Chen T, Lian Y X, Wang X L and Li C 2007 *J. Phys. Chem. C* **111** 693.

[42] Zhang J, Xu Q, Feng Z C, Li M J and Li C 2008 *Angew. Chem. Int. Ed.* **47** 1766.

[43] Puangpetch T, Sreethawong T, Yoshikawa S and Chavadej S 2009 *J. Mol. Catal. A: Chem.* **312** 97.

[44] Ikeda S, Hirao K, Ishino S, Matsumura M and Ohtani B 2006 *Catal. Today* **117** 343.

[45] Liu Y, Xie L, Li Y, Yang R, Qu J L, Li Y Q and Li X G 2008 *J. Power Sources* **183** 701.

[46] Kudo A, Tanaka A, Domen K and Onishi T 1988 *J. Catal.* **111** 296.

[47] Domen K, Kudo A, Onishi T, Kosugi N and Kuroda H 1986 *J. Phys. Chem.* **90** 292.

[48] Domen K, Naito S, Onishi T, Tamaru K and Soma M 1982 *J. Phys. Chem.* **86** 3657.

[49] Domen K, Saito S, Onishi T and Tamaru K 1982 *Chem. Phys. Lett.* **92** 433.

[50] Domen K, Kudo A and Onishi T 1986 *J. Catal.* **102** 92.

[51] Tanaka T and Domen K 2009 *J. Phys. Chem. C* **113**19386.

[52] Chen X Y, Yu T, Fan X X, Zhang H T, Li Z S, Ye J H and Zou Z G 2007 *Appl. Surf. Sci.* **253** 8500.

[53] Chen D and Ye J H 2009 *Chem. Mater.* **21** 2327.

[54] Sayama K, Arakawa H and Domen K 1996 *Catal. Today* **28** 175.

[55] Gonçalves R V, Migowski P, Wender H, Eberhardt D, Weibel D E, Sonaglio F C, Zapata M J M, Dupont J, Feil A F and Teixeira R T 2012 *J. Phys. Chem. C* **116** 14022.

[56] Duan J Y, Shi W D, Xu L L, Mou G Y, Xin Q L and Guan J G 2012 *Chem. Commun.* **48** 7301.

[57] Lü X J, Ding S J, Lin T Q, Mou X L, Hong Z Land Huang F Q 2012 *Dalton Trans.* **41** 622.

[58] Sreethawong T, Ngamsinlapasathian S, Suzuki Y and Yoshikawa S 2005 *J. Mol. Catal. A: Chem.* **235** 1.

[59] Takahara Y, Kondo J N, Takata T, Lu D L and Domen K 2001 *Chem. Mater.* **13** 1194.

[60] Kondo J N and Domen K 2008 *Chem. Mater.* **20** 835.

[61] Noda Y, Lee B, Domen K and Kondo J N 2008 *Chem. Mater.* **20** 5361.

[62] Li Z H, Liu J W, Li J Y and Shen J 2012 *Nanoscale* **4** 3867.

[63] Sato J, Kobayashi H, Saito N, Nishiyama H and Inoue Y 2003 *J. Photochem. Photobiol., A* **158** 139.

[64] Sato J, Saito N, Nishiyama H and Inoue Y 2003 *J. Phys. Chem. B* **107** 7965.

[65] Sato J, Kobayashi H and Inoue Y 2003 *J. Phys. Chem. B* **107** 7970.

[66] Chen X B, Shen S H, Guo L J and Mao S S 2010 *Chem. Rev.* **110** 6503.

[67] Asahi R, Morikawa T, Ohwaki T, Aoki K and Taga Y 2001 *Science* **293** 269.

[68] Sayed F N, Jayakumar O D, Sasikala R, Kadam R M, Bharadwaj S R, Kienle L, Schürmann U, Kaps S, Adelung R, Mittal J P and Tyagi A K 2012 *J. Phys. Chem. C* **116** 12462.

[69] Wu M C, Hiltunen J, Sápi A, Avila A, Larsson W, Liao H C, Huuhtanen M, Tóth, Shchukarev A, Laufer N, Kukovecz Á, Kónya Z, Mikkola J P, Keiski R, Su W F, Chen Y F, Jantunen H, Ajayan P M, Vajtai R and Kordás K 2011 *ACS Nano* **5** 5025.

[70] Park J H, Kim S and Bard A 2006 *Nano Lett.* **6** 24.

[71] Wen C Z, Hu Q H, Guo Y N, Gong X Q, Qiao S Z and Yang H G 2011 *Chem. Commun.* **47** 6138.

[72] Szatmáry L, Bakardjieva S, Šubrt J, Bezdička P, Jirkovský, Bastl Z, Brezová V and Korenko M 2011*Catal. Today* **161** 23.

[73] Yu H, Ouyang S X, Yan S C, Li Z S, Yu T and Zou Z G 2011 *J. Mater. Chem.* **21** 11347.

[74] Liu J W, Chen G, Li Z H and Zhang Z G 2006 *J. Solid State Chem.* **179** 3704.

[75] Reunchan P, Umezawa N, Ouyang S X and Ye J H 2012 *Phys. Chem. Chem. Phys.* **14** 1876.

[76] Bae S W, Borse P H and Lee J S 2008 *Appl. Phys. Lett.* **92** 104107.

[77] Kudo A and Mikami I 1998*Chem. Lett.* 1027.

[78] Zou Z G, Ye J H and Arakawa H 2001 *Mater. Res. Bull.* **36** 1185.

[79] Zhang L Z, Djerdj I, Cao M H, Antonietti M and Niederberger M 2007 *Adv. Mater.* **19** 2083.

[80] Chiou Y C, Kumar U and Wu J C S 2009 *Appl. Catal., A: General* **357** 73.

[81] Matsumura M, Saho Y and Tsubomura 1983 *J. Phys. Chem.* **87** 3807.

[82] Reber J F and Rusek M 1986 *J. Phys. Chem.* **90** 824.

[83] Jing D W and Guo L J 2006 *J. Phys. Chem. B* **110** 11139.

[84] Sathish M and Viswanath R P 2007 *Catal. Today* **129** 421.

[85] Bao N Z, Shen L M, Takata T and Domen K 2008 *Chem. Mater.* **20** 110.

[86] Jang J S, Joshi U A and Lee J S 2007 *J. Phys. Chem. C* **111** 13280.

[87] Berr M, Vaneski A, Susha A S, Rodríguez-Fernáadez J, Döblinger M, Jäckel F, Rogach A L and Feldmann J 2010 *Appl. Phys. Lett.* **97** 093108.

[88] Ma G J, Yan H J, Shi J Y, Zong X, Lei Z B and Li C 2008 *J. Catal.* **260** 134.

[89] Zhang W, Wang Y B, Wang Z, Zhong Z Y and Xu R 2010 *Chem. Commun.* **46** 7631.

[90] Zong X, Yan H G, Wu G P, Ma G J, Wen F Y, Wang L and Li C 2008 *J. Am. Chem. Soc.* **130** 7176.

[91] Lei Z B, You W S, Liu M Y, Zhou G H, Takata T, Hara M, Domen K and Li C 2003 *Chem. Commun.* **17** 2142.

[92] Shen S H, Chen X B, Ren F, Kronawitter C X, Mao S S and Guo L J 2011 *Nanoscale Res. Lett.* **6** 290.

[93] Shen S H, Chen J, Wang X X, Zhao L and Guo L J 2011 *J. Power Sources* **196** 10112.

[94] Kale B B, Baeg J O, Lee S M, Chang H, Moon S J and Lee C W 2006 *Adv. Funct. Mater.* **16** 1349.

[95] Jang J S, Choi S H, Shin N, Yu C J and Lee J S 2007 *J. Solid State Chem.* **180** 1110.

[96] Jang J S, Borse P H, Lee J S, Choi S H and Kim H G 2008 *J. Chem. Phys.* **128** 154717.

[97] Kudo A, Nagane A, Tsuji I and Kato H 2002 *Chem. Lett.* **31** 882.

[98] Zheng L, Xu Y, Song Y, Wu C Z, Zhang M and Xie Y 2009 *Inorg. Chem.* **48** 4003.

[99] Tabata M, Maeda K, Takahiro T, Minegishi T, Takata T and Domen K 2010 *J. Phys. Chem. C* **114** 11215.

[100] Kale B B, Baeg J O, Kong K J, Moon S J, Nikam L K and Patil K R 2011 *J. Mater. Chem.* **21** 2624.

[101] Wang L, Wang W Z and Sun S M 2012 *J. Mater. Chem.* **22** 6553.

[102] Kudo A and Miseki Y 2009 *Chem. Soc. Rev.* **38** 253.

[103] Yashima M, Ogisu K and Domen K2008 *Acta Cryst.* **B64** 291.

[104] Ishikawa A, Takata T, Kondo J N, Hara M, Kobayashi H and Domen K 2002 *J. Am. Chem. Soc.* **124** 13547.

[105] Ishikawa A, Yamada Y, Takta T, Kondo J N, Hara M, Kobayashi K and Domen K 2003 *Chem. Mater.* **15** 4442.

[106] Zhang F X, Maeda K, Takata T and Domen K 2010 *Chem. Commun.* **46** 7313.

[107] Zhang F X, Maeda K, Takata T and Domen K 2011 *J. Catal.* **280** 1.

[108] Zhang F X, Maeda K, Takata T, Hisatomi T and Domen K 2012 *Catal. Today* **185** 253.

[109] Ikeue K, Ando S, Mitsuyama T, Ohta Y, Arayama K, Tsutsumi A and Machida M 2008 *Top Catal.* **47** 175.

[110] Ishikawa A, Takata T, Matsumura T, Kondo J N, Hara M, Kobayashi H and Domen K 2004 *J. Phys. Chem. B* **108** 2637.

[111] Ogisu K, Ishikawa A, Teramura K, Toda K, Hara M and Domen K 2007 *Chem. Lett.* **36** 854.

[112] Sato J, Saito N, Yamada Y, Maeda K, Takata T, Kondo J N, Hara M, Kobayashi H, Domen K and Inoue Y 2005 *J. Am. Chem. Soc.* **127** 4150.

[113] Maeda K, Saito N, Inoue Y and Domen K 2007 *Chem. Mater.* **19** 4092.

[114] Maeda K, Saito N, Lu A L, Inoue Y and Domen K 2007 *J. Phys. Chem. C* **111** 4749.

[115] Kida T, Minami Y, Guan G, Nagano M, Akiyama M and Yoshida A 2006 *J. Mater. Sci.* **41** 3527.

[116] Maeda K, Teramura K, Saito N, Inoue Y and Domen K 2007 *Bull. Chem. Soc. Jpn.* **80** 1004.

[117] Hitoki G, Ishikawa A, Takata T, Kondon J N, Hara M and Domen K 2002 *Chem. Lett.* **31** 736.

[118] Feng X J, LaTempa T J, Basham J I, Mor G K, Varghese O K and Grimes C A 2010 *Nano Lett.* **10** 948.

[119] Yokoyama D, Hashiguchi H, Maeda K, Minegishi T, Takata T, Abe R, Kubota J nad Domen K 2011 *Thin Solid Films* **519** 2087.

[120] Domen K, Hara M, Kondo J N, Takata T, Kudo A, Kobayashi H and Inoue Y 2001 *Korean J. Chem. Eng.* **18** 862.

[121] Hara M, Hitoki G, Takata T, Kondo J N, Kobayashi H and Domen K 2003 *Catal. Today* **78** 555.

[122] Higashi M, Abe R, Takata T and Domen K 2009 *Chem. Mater.* **21** 1543.

[123] Siritanaratkul B, Maeda K, Hisatomi T and Domen K 2011 *ChemSusChem* **4** 74.

[124] Wang X C, Maeda K, Thomas A, Takanabe K, Xin G, Carlsson J M, Domen K and Antonietti M 2009 *Nat. Mater.* **8** 76.

[125] Zhang J S, Chen X F, Takanabe K, Maeda K, Domen K, Epping J D, Fu X Z, Antonietti M and Wang X C 2010 *Angew. Chem. Int. Ed.* **49** 441.

[126] Zhang Y W, Liu J H, Wu G and Chen W 2012 *Nanoscale* **4** 5300.

[127] Yan H J 2012 *Chem. Commun.* **48** 3430.

[128] Hong J D, Xia X Y, Wang Y S and Xu R 2012 *J. Mater. Chem.* **22** 15006.

[129] Liu G, Niu P, Sun C H, Smith S C, Chen Z G, Lu G Q and Cheng H M 2010 *J. Am. Chem. Soc.* **132** 11642.

[130] Dong G H, Zhao K and Zhang L Z 2012 *Chem. Commun.* **48** 6178.

[131] Ng J W, Xu S P, Zhang X W, Yang H Y and Sun D D 2010 *Adv. Funct. Mater.* **20** 4287.

[132] Long M, Cai W M, Cai J, Zhou B X, Chai X Y and Wu Y H 2006 *J. Phys. Chem. B* **110** 20211.

[133] Kim J and Kang M 2012 *Bull. Korean Chem. Soc.* **33** 2133.

[134] Gu Q, Long J L, Zhou Y G, Yuan R S, Lin X X and Wang X X 2012 *J. Catal.* **289** 88.

[135] Shen J, Meng Y L and Xin G 2011 *Rare Metals* **30** 280.

[136] Li C L, Yuan J A, Han B Y, Jiang L and Shangguan W F 2010 *Int. J. Hydrogen Energy* **35** 7073.

[137] Zhang X Y, Li H P, Cui X L and Lin Y H 2010 *J. Mater. Chem.* **20** 2801.

[138] Takenaka S, Arike T, Miyazaki T, Matsune H and Kishida M 2012 *Chem. Lett.* **41** 617.

[139] Xing Q J, Yu J G and Jaroniec M 2012 *J. Am. Chem. Soc.* **134** 6575.

[140] Zhang J, Xu Q, Feng Z C, Li M J and Li C 2008 *Angew. Chem. Int. Ed.* **47** 1766.

[141] Wang D F, Zou Z G and Ye J H 2005 *Chem. Mater.* **17** 3255.

[142] Lv J, Kako T, Li Z S, Zou Z G and Ye J H 2010 *J. Phys. Chem. C* **114** 6157.

[143]Wang D F, Zou Z G and Ye J H 2004*Chem.Phys.Lett.* **384** 139.

[144] Xu L L, Guan J G, Gao L and Sun Z G 2011 *Catal. Commun.* **12** 548.

[145] Xu L L, Guan J G, Shi W D and Liu L J 2012 *J. Colloid Interface Sci.* **377** 160.

[146] Maeda K, Terashima H, Kase K, Higashi M, Tabata M and Domen K 2008 *Bull. Chem. Soc. Jpn* **81** 927.

[147]Bessekhouad Y, Trari M and Doumerc J P 2003 *Int. J. Hydrogen Energy* **28** 43.

[148] Saadi S, Bouguelia A and Trari M 2006 *Solar Energy* **80** 272.

[149] Brahimi R, Bessekhouad Y, Bouguelia A and Trari M 2007 *J. Photochem. Photobiol. A: Chemistry* **186** 242.

[150] Derbal A, Omeiri S, Bouguelia A and Trari M 2008 *Int. J. Hydrogen Energy* **33** 4274.

[151] Kim H G, Borse P H, Jang J S, Jeong E D, Jung O S, Suh Y J and Lee J S 2009 *Chem. Commun.* **39** 5889.

[152] Jang J S, Hwang D W AND Lee J S 2007 *Catal. Today* **120** 174.

[153] Ge L, Zuo F, Liu J K, Ma Q, Wang C, Sun D Z, Bartels L and Feng P Y 2012 *J. Phys. Chem. C* **116** 13708.

[154] Yan H J and Yang H X 2011 *J. Alloys Compd.* **509** L26.

[155] Wang D F, Kako T and Ye J H 2008 *J. Am. Chem. Soc.* **130** 2724.

[156] Wang D F, Kako T and Ye J H 2009 *J. Phys. Chem. C* **113** 3785.

[157] Luo W J, Li Z S, Jiang X J, Yu T, Liu L F, Chen X Y, Ye J H and Zou Z G 2008 *Phys. Chem. Chem. Phys.* **10** 6717.

[158] Maeda K, Teramura K, Takata T, Hara M, Saito N, Toda K, Inoue Y, Kobayashi H and Domen K 2005 *J. Phys. Chem. B* **109** 20504.

[159] Yashima M, Yamada H, Maeda K and Domen K 2010 *Chem. Commun.* **46** 2379.

[160] Maeda K, Teramura K, Lu D L, Saito N, Inoue Y and Domen K 2006 *Angew. Chem. Int. Ed.* **45** 7806.

[161] Hisatomi T, Maeda K, Takanabe K, Kubota J and Domen K 2009 *J. Phys. Chem. C* **113** 21458.

[162] Maeda K, Teramura K, Liu D L, Saito N, Inoue Y and Domen K 2007 *J. Phys. Chem. C* **111** 7554.

[163] Yoshida M, Takanabe K, Maeda K, Ishikawa A, Kubota J, Sakata Y, Ikezawa Y and Domen K 2009 *J. Phys. Chem. C* **113** 10151.

[164] Lee Y, Terashima H, Shimodaira Y, Teramura K, Hara M, Kobayashi H, Domen K and Yashima M 2007 *J. Phys. Chem. C* **111** 1042.

[165] Lee Y, Teramura K, Hara M and Domen K 2007 *Chem. Mater.* **19** 2120.

[166] Wang X C, Maeda K, Lee Y and Domen K 2008 *Chem. Phys. Lett.* **457** 134.

[167] Tessier F, Maillard P, Lee Y, Bleugat C and Domen K 2009 *J. Phys. Chem. C* **113** 8526.

[168] Kakuta N, Park K H, Finlayson M F, Ueno A, Bard A J, Campion A, Fox M A, Webber S E and White J M 1985 *J. Phys. Chem.* **89** 732.

[169] Youn H C, Baral S and Fendler J H 1988 *J. Phys. Chem.* **9**2 6320.

[170] Liu M C, Wang L Z, Lu G Q, Yao X D and Guo L J 2011 *Energy Environ. Sci.* **4** 1372.

[171] Wang D H, Wang L and Xu A W 2012 *Nanoscal* **4** 2046.

[172] Tsuji I, Kato H, Kobayashi H and Kudo A 2004 *J. Am. Chem. Soc* .**126** 13406.

[173] Tsuji I, Kato H, Kobayashi H and Kudo A 2005 *J. Phys. Chem. B* **109** 7323.

[174] Torimoto T, Adachi T, Okazaki K, Sakuraoka M, Shibayama T, Ohtani B, Kudo A and Kuwabata S 2007 *J. Am. Chem. Soc.* **129** 12388.

[175] Kudo A, Tsuji I and Kato H 2002 *Chem. Commun.* **17** 1958.

[176] Tsuji I, Kato H and Kudo A 2005 *Angew. Chem. Int. Ed.* **44** 3565.

[177] Tsuji I, Kato H and Kudo A 2006 *Chem. Mater.* **18** 1969.

[178] Tsuji I, Shimodaira Y, Kato H, Kobayashi H and Kudo A 2010 *Chem. Mater.* **22** 1402.

[179] Kaga H, Saito K and Kudo A 2010 *Chem. Commun.* **46** 3779.

[180] Penn R L and Banfield J F 1998 *Science* **281** 969.

Chapter 2 Zinc Indium Oxide ($Zn_5In_2O_8$)/Surface-S-doped $Zn_5In_2O_8$ Composite for Photocatalytic Water Splitting

2.1 Introduction

Intensive research interest has been devoted to semiconductor photocatalysts that can produce H_2 from water using solar energy because of the increasing energy requirements and environmental concerns. Many types of photocatalysts have been reported to produce H_2 or/and O_2 from water under light irradiation, such as metal oxides [1-7] and metal oxysulfides [8, 9]. To efficiently utilize solar energy, bandgap modification is necessary to make wide-bandgap photocatalysts sensitive to visible light as mentioned in Chapter 1. Doping is an effective way of designing visible-light-sensitive photocatalysts [10-13]. Simultaneously, nondoped visible-light-sensitive photocatalysts are also drawing intense attention. Photocatalysts which contain a *p*-block metal ion with a d^{10} configuration (i.e. In^{3+}) exhibit good photocatalytic activity for water splitting [14]. Zinc indium oxides ($In_2O_3(ZnO)_k$, k = integer) show excellent electron transport properties [15] and are promising visible-light-sensitive photocatalysts for water splitting [16].

Appropriate composites can promote the separation and migration of photoinduced electrons and holes and accordingly enhance the photocatalytic activity of H_2 evolution, because rapid recombination of photogenerated electron-hole pairs is one of the most disadvantageous factors for photocatalytic water splitting [17]. Many reports reveal that semiconductor composites can effectively suppress the recombination of photogenerated electron-hole pairs [17-20]. The valence bands (VBs) and conduction bands (CBs) of the semiconductors in a composite have different energies, and the resulting potential difference assists the separation and migration of photoinduced electrons and holes [18]. Generally, the

VB top in metal oxides consists of the O 2*p* orbitals. Whereas in S-doped oxides, it mainly involves the S 3*p* orbitals, which narrows the band gap [21]. Therefore, we considered that a $Zn_5In_2O_8$/surface-S-doped $Zn_5In_2O_8$ composite could have an enhanced photocatalytic H_2 evolution efficiency compared with the $Zn_5In_2O_8$.

Surface vacancies significantly affect the crystal growth, especially in the weak driving force regime, and provide nucleation sites for phase transformations [22]. Here, we developed a facile photoassisted method of fabricating $Zn_5In_2O_8$/surface-S-doped $Zn_5In_2O_8$ composites using a vacancy-rich $Zn_5In_2O_8$ as the precursor. The S-doped $Zn_5In_2O_8$ was *in situ* generated on the surfaces of precursors in a Na_2S/K_2SO_3 aqueous solution. It was found that surface sulfuration of vacancy-rich $Zn_5In_2O_8$ was an effective route to synthesize efficient $Zn_5In_2O_8$/surface-S-doped $Zn_5In_2O_8$ composite for photocatalytic water splitting.

2.2 Experimental section

2.2.1 Synthesis of $Zn_5In_2O_8$ (ZIO) and vacancy-rich ZIO

All chemicals were purchased from Wako Company, including zinc oxide (ZnO, 99.9%), indium oxide (In_2O_3, 99.9%), sodium chloride (NaCl, > 99.5%), potassium chloride (KCl, > 99.5%), and copper metal powder (Cu, > 99.85%). They were used without further treatment. Powders of ZIO and vacancy-rich ZIO were synthesized by the molten-salt method. The typical fabrication steps were as follows. NaCl (7.3050 g)/KCl (9.3188 g) and ZnO (1.0174 g)/In_2O_3 (0.6941 g) were mixed evenly and then milled with an appropriate amount of ethanol in a mortar for 30 min. The mixture was dried in an oven at 60 °C for 2-3 hours and then heated at 1200 °C for 3 h. The products were cleaned with distilled water until Cl^- ions could not be detected using silver nitrate ($AgNO_3$), and then dried in an oven at 60 °C for one day.

The as-synthesized ZIO was further treated to generate artificial vacancies. In this study, we adopted the high-temperature molten-salt process to prepare a vacancy-rich $Zn_5In_2O_8$ under Ar atmosphere because vacancies can be generated at high temperatures [23]. The Cu metal powder was added as a getter of the trace O_2 resulting from leaks. In a typical procedure, ZIO (0.950 g), NaCl (5.844 g)/KCl (7.455 g), and 9.5 mg of Cu powder were mixed together and milled with an appropriate amount of ethanol. Then, the mixture was dried in an oven at 60 °C for 2-3 hours and heated in a horizontal tube furnace at 850 °C for 18 h under the Ar atmosphere. The red-colored Cu layer and the concretionary molten salt were washed away using distilled water until Cl^- ions could not be detected. This vacancy-rich ZIO powder was dried in an oven at 60 °C for 24 h. It is worth noting that the color of the vacancy-rich ZIO was blue, but it turned yellow during the milling. Hence, vacancies were only introduced on the surface of ZIO.

2.2.2 Synthesis of $Zn_5In_2O_8$/surface-S-doped oxide composite

In a typical procedure, 0.30 g of vacancy-rich ZIO was suspended in 270 ml of Na_2S (0.35 M)/K_2SO_3 (0.25 M) aqueous solution containing $H_2PtCl_6 \cdot 6H_2O$ under continuous magnetic stirring. Then, this mixture was irradiated by a 300 W Xe lamp for 48 h to sulfurize the surface layer and form a $Zn_5In_2O_8$/surface-S-doped vacancy-rich-$Zn_5In_2O_8$ (ZIO/S-doped V-ZIO) composite. Figure 2.1 shows the formation mechanism of ZIO/S-doped V-ZIO. First, the as-synthesized ZIO was treated to produce In and O vacancies; then, it was irradiated by UV and visible light in a Na_2S/K_2SO_3 aqueous solution. As a result, the vacancy-rich surface part reacted with Na_2S to produce a S-doped layer on the surface of ZIO. At the same time, the Pt cocatalyst (0.5 wt%) was loaded on the surface of the composite during the sulfuration process under this combined UV and visible light irradiation. Then, the ZIO/S-doped V-ZIO composite was continuously irradiated by the Xe lamp with a UV-cut-off filter (L42, Hoya

Co., Japan) for 5 cycles (24 h/cycle).For comparison, the pristine ZIO was treated by the same procedure to prepare a $Zn_5In_2O_8$/surface-S-doped $Zn_5In_2O_8$ (ZIO/S-doped ZIO) composite. This procedure was performed in a closed gas-circulation system.

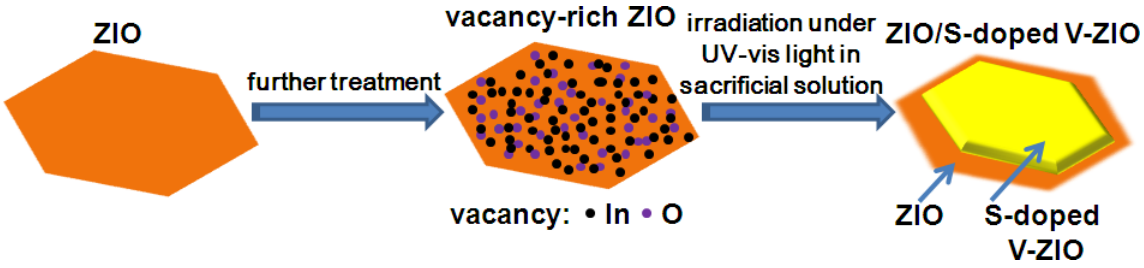

Figure 2.1 Schematic of the formation process of ZIO/S-doped V-ZIO composite.

2.3 Characterization

The surface morphology of the synthesized samples was characterized with a field-emission scanning electron microscope (SEM, JSM-6701F, JEOL Co., Japan) equipped with an energy-dispersive X-ray spectrometer (EDX). Powder X-ray diffraction (XRD) characterization was performed using a Rint-2000 diffractometer (Rigaku Co., Japan, Cu Kα radiation, λ = 1.5406 Å) operated at 40 kV and 20 mA. Inductively coupled plasma/optical emission spectroscopy (ICP/OES) characterization for Zn and In elements was carried out with an IRIS Advantage setup (Nippon Jarrell-Ash Co., Japan). The Brunauer-Emmett-Teller (BET) surface area was measured by nitrogen adsorption at 77 K with a BELSORP mini II surface area analyzer (Bel Japan Co., Japan). X-ray photoelectron spectroscopy (XPS) studies were carried out with a Theta Probe using monochromatized Al Kα radiation (1486.6 eV). UV-visible diffuse reflection spectra were recorded on a UV-2500PC spectrophotometer (Shimadzu Co., Japan) and converted into absorption spectra using the Kubelka-Munk equation. High-resolution transmission electron microscopy (HRTEM) and scanning

transmission electron microscopy (STEM) images and elemental mapping were acquired with a JEM-2100F microscope (JEOL).

2.4 Photocatalytic H_2 evolution

The closed gas-circulation system mentioned above was evacuated to evaluate the photocatalytic activity of the studied composites. The visible light (λ > 400 nm) was generated by a 300 W Xe lamp combined with a UV-cut-off filter (L42, Hoya Co., Japan). The evolved H_2 was analyzed using an on-line gas chromatograph (GC-8A, Shimadzu Co., Japan) equipped with a thermal conductivity detector (TCD). The apparent quantum efficiency (AQE) was measured by applying a Xe lamp (300 W) with a 420 nm band-pass filter (MIF-W, Optical Coatings Japan Co., Japan; λ_0 = 418.5 ± 14.5 nm). The number of incident photons was measured using a radiant power energy meter (Ushio Spectroradiometer, USR-40).The AQE was calculated using the following equation:

$$AQE\ (\%) = \frac{\text{Number of reacted electrons}}{\text{Number of incident photons}} \times 100\%$$
$$= \frac{\text{Number of evolved } H_2 \text{ molecules} \times 2}{\text{Number of incident photons}} \times 100\%$$

2.5 Results and discussion

2.5.1 Crystal structure, morphology, and optical properties of ZIO and vacancy-rich ZIO

The XRD patterns of ZIO and vacancy-rich ZIO are given in Figure 2.2. The XRD patterns show similar peaks among the products and can be indexed to the pure hexagonal $Zn_5In_2O_8$ phase (JCPDS card: 020-1440) as in the previous report [24]. Therefore, it can be concluded that the crystal structure of ZIO was unchanged by the vacancy generation. However, the peak intensities decreased after the treatment, implying loss of crystallinity.

Figure 2.3 shows the typical SEM images of ZIO and vacancy-rich ZIO. Frequency analysis indicates that ZIO consists of particles with average diameters of 2.45 and 3.28 μm for untreated and vacancy-rich ZIO, respectively (Figure 2.4).

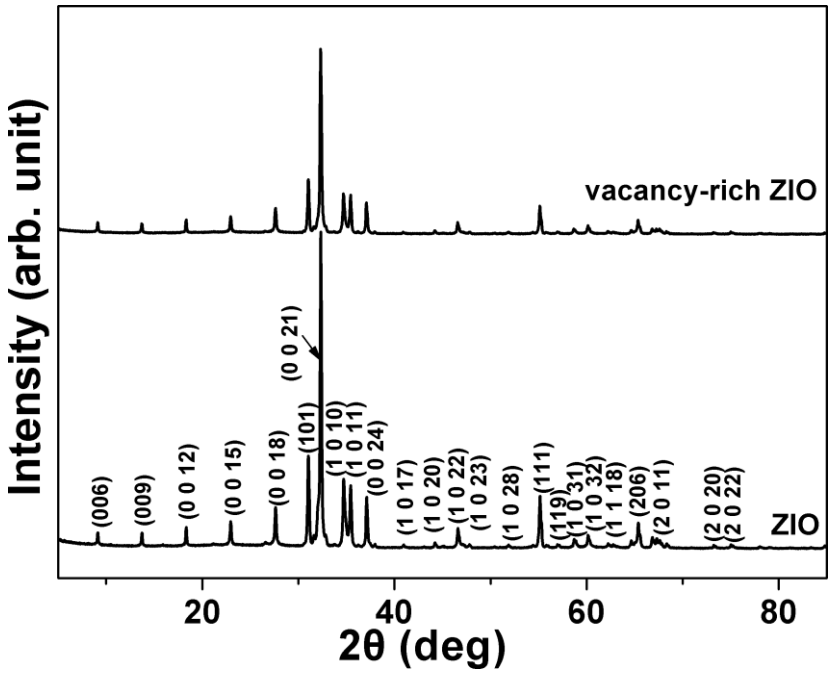

Figure 2.2 XRD patterns of (a) ZIO and (b) vacancy-rich ZIO.

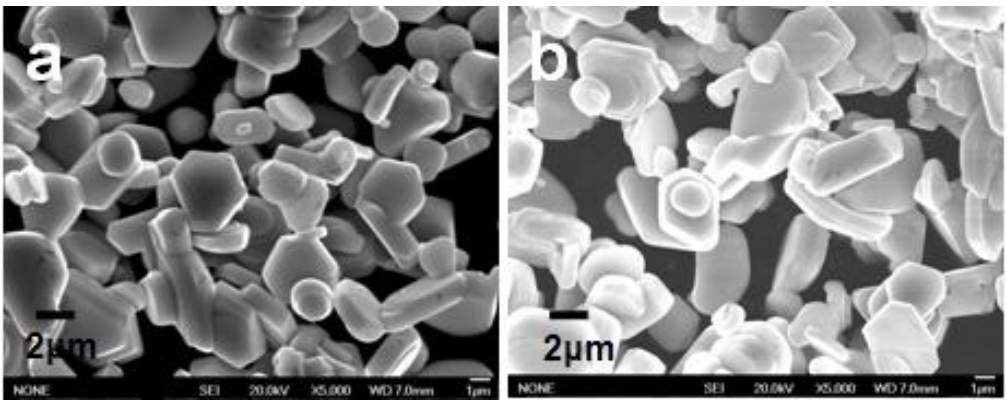

Figure 2.3 SEM images of (a) ZIO and (b) vacancy-rich ZIO.

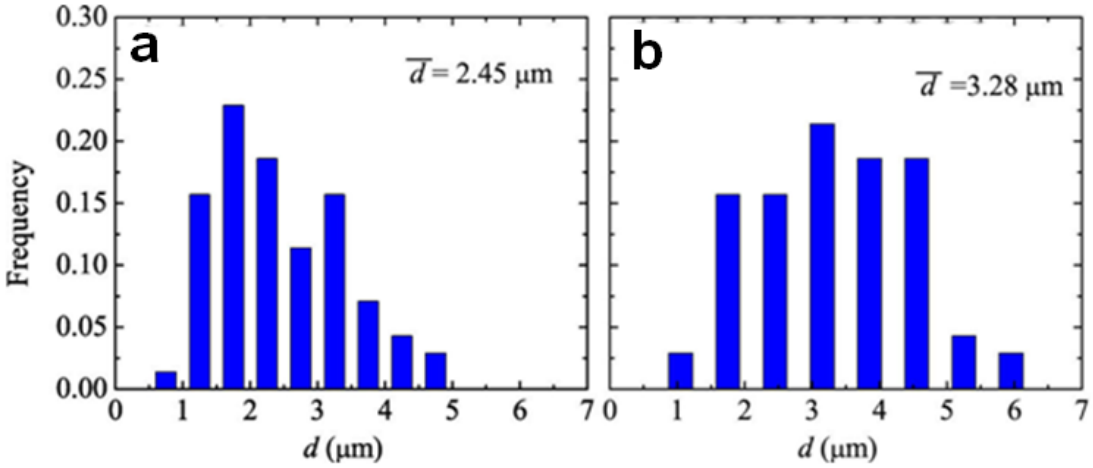

Figure 2.4 Frequency analysis for the particle diameter in (a) ZIO and (b) vacancy-rich ZIO.

The ICP/OES data indicate a slightly larger Zn/In molar ratio in the vacancy-rich (Zn/In = 2.43) than in the untreated ZIO (Zn/In = 2.40), which can be explained by a higher concentration of In vacancies in the former material. Those indium vacancies could be produced at high temperatures via indium sublimation, as reported for indium tin oxide [25]. Indium evaporates from the ZIO bulk as In_2O gas and, simultaneously, O_2 gas forms at high temperatures in the inert atmosphere. A possible formation mechanism of vacancies in ZIO can be expressed as:

$$Zn_5In_2O_8 \rightarrow Zn_5In_{2-x}O_{8-1.5x} + 0.5xIn_2O(gas) + 0.5xO_2(gas).$$

Figure 2.5 shows the optical absorption spectra of ZIO and vacancy-rich ZIO. The ZIO absorbs wavelengths shorter than 500 nm via transitions between the VB and CB. The spectrum of vacancy-rich ZIO is blue-shifted compared with that of ZIO. Furthermore, the vacancy-rich ZIO shows an absorption from 480 nm, which possibly results from the O defects. A similar phenomenon was reported for the $Sr(TiO_3)_{1-x}\cdot(LaTiO_2N)_x$ solid solution by Luo *et al*. [26].

The blue-shift in the vacancy-rich ZIO is consistent with the formation of indium vacancies. For $In_2O_3(ZnO)_k$ (k = integer), the CB bottom mainly consists of the In 5*s* level

with a minor contribution from the Zn 4*s* level [15], and the In 5*s* level locates below the Zn 4*s* level [27]. Therefore, the loss of indium widens the bandgap of vacancy-rich ZIO. Furthermore, since Cu doping narrows the bandgap by introducing Cu 3*d* levels above the VB of ZIO [28], it can be concluded that the Cu concentration was rare in the vacancy-rich ZIO.

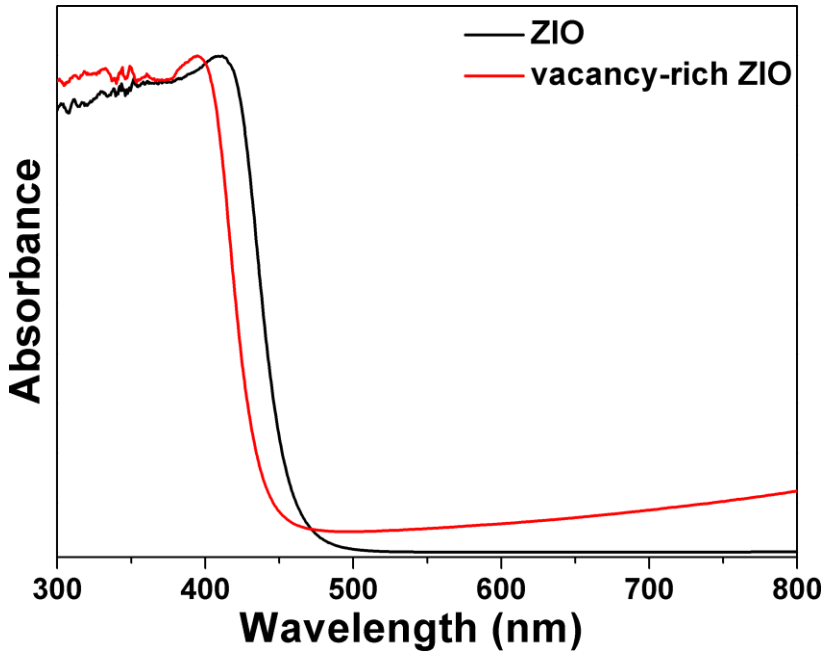

Figure 2.5 UV-vis absorption spectra of (a) ZIO and (b) vacancy-rich ZIO.

2.5.2 Evaluation of photocatalytic H_2 evolution under visible-light irradiation

As mentioned above, the samples were pretreated in a Na_2S/K_2SO_3 aqueous solution for 48 h under UV and visible light irradiation using a Xe lamp (300 W) before the evaluation of photocatalytic activity. Figure 2.6 shows the H_2 evolution rates of ZIO/S-doped V-ZIO and ZIO/S-doped ZIO composites under visible-light irradiation ($\lambda > 400$ nm). Five cycles were carried out and the evaluation system was evacuated after each cycle. The H_2 evolution rates are summarized in Table 2.1, revealing much higher values for ZIO/S-doped V-ZIO than for ZIO/S-doped ZIO at every 24-h cycle. The maximum rate of ZIO/S-doped V-ZIO was 94.7

μmol/h. It is about 18 times as high as that of ZIO/S-doped ZIO in the same cycle. The AQE for ZIO/surface-S-doped V-ZIO was about 5.2% at 420 nm.

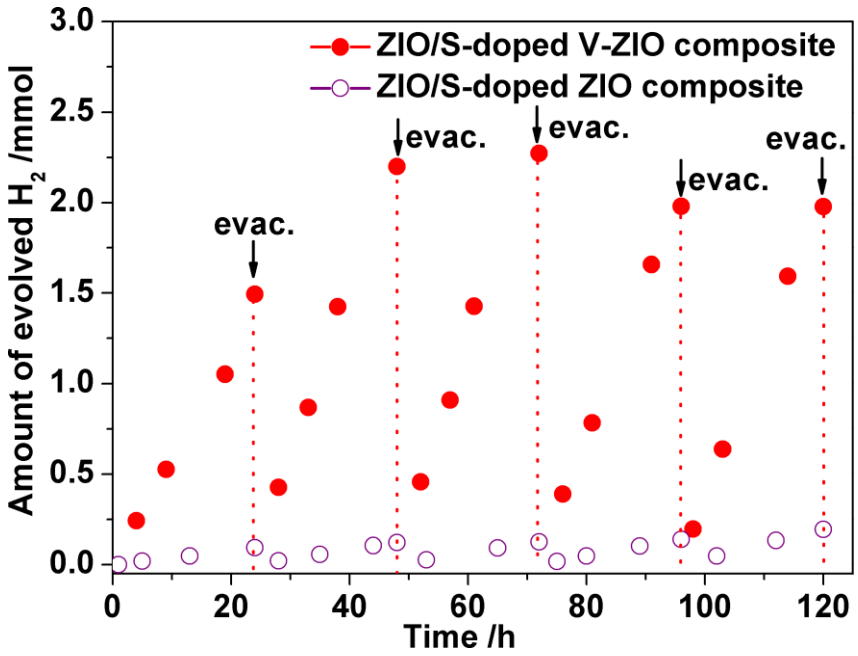

Figure 2.6 Time course of photocatalytic H_2 evolution in a K_2SO_3/Na_2S aqueous solution (270 ml) over 0.3 g Pt (0.5 wt%)/$Zn_5In_2O_8$ under visible light irradiation ($\lambda > 400$ nm). (a) ZIO/S-doped V-ZIOcomposite, (b) ZIO/S-doped ZIOcomposite. The ZIO and vacancy-rich ZIO were pre-irradiated by UV-visible light for 48 h in a K_2SO_3/Na_2S aqueous solution before this measurement.

Table 2.1 H_2 evolution rate (μmol/h) under visible-light irradiation ($\lambda > 400$ nm)

Sample	Cycle 1	Cycle 2	Cycle 3	Cycle 4	Cycle 5
ZIO/S-doped V-ZIO	62.3	91.6	94.7	82.4	82.4
ZIO/S-doped ZIO	3.9	5.1	5.2	5.8	8.1

2.5.3 Characterization of oxide/surface-S-doped oxide composites

The samples after photocatalytic H_2 evolution were cleaned several times with distilled water, dried, and collected for further characterization. Figures 2.7(a) and (b) show the SEM images of ZIO/S-doped V-ZIO and ZIO/S-doped ZIO composites, respectively. The edges and corners of particles are more diffuse compared with those in Figure 2.3 and fine particles appear on the surface, revealing that the surface was perturbed by the sulfuration. According to the BET analysis, the surface area was increased from 0.20 to 44 and 26 m^2/g for ZIO/S-doped V-ZIO and ZIO/S-doped ZIO, respectively. Figures 2.7(c) and (d) show the EDX spectra of ZIO/S-doped V-ZIO and ZIO/S-doped ZIO composites, revealing Zn, In, O, and S elements.

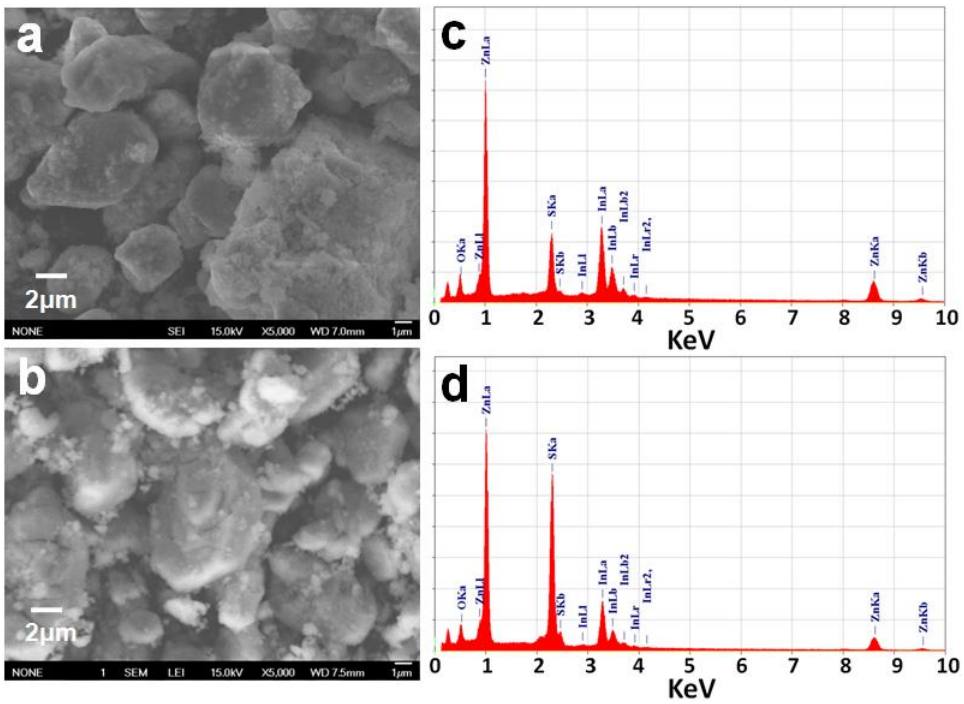

Figure 2.7 SEM images of (a) ZIO/S-doped V-ZIO and (b) ZIO/S-doped ZIO composites; EDX spectra of (c) ZIO/S-doped V-ZIO and (d) ZIO/S-doped ZIO composites.

Figure 2.8(a) shows XRD patterns of ZIO, vacancy-rich ZIO, ZIO/S-doped V-ZIO, and ZIO/S-doped ZIO composites. A minor ZnS impurity was detected in the ZIO/S-doped V-ZIO and ZIO/S-doped ZIO composites, which was a by-product of the sulfuration process. The (0 0 21) peak shows left-shift for the ZIO/S-doped ZIO and ZIO/S-doped V-ZIO composites in Figure 2.8(b). Such shift can be attributed to the substitution of S^{2-} ions (1.84 Å in radius) for O^{2-} ions (1.4 Å in radius).

Figure 2.9 shows the peak-fitting of (0 0 21) of ZIO/S-doped V-ZIO composite. It can be separated into two peaks which belong to ZIO and S-doped V-ZIO. The 2θ values of ZIO and V-ZIO are 32.28° and 32.18°, respectively. We can estimate the degree of S/O substitution in S-doped ZIO. The concrete calculation procedures are showed as follows. Δd is the difference of interplanar distance of (0 0 21) of ZIO and S-doped V-ZIO; c_1 and $c_2$are the values of the c axis of ZIO and S-doped V-ZIO, respectively. According to the Bragg equation and the calculation equation of interplanar distance for hexagonal crystals, we can get the following equations:

$$\Delta d_{(0\,0\,21)} = \frac{\lambda}{2}\left(\frac{1}{\sin 16.09} - \frac{1}{\sin 16.14}\right)$$

$$\Delta d_{(0\,0\,21)} = d_{S-ZIO(0\,0\,21)} - d_{ZIO(0\,0\,21)} = \frac{C_2 - C_1}{21}$$

Then the expansion of c axis of S-doped V-ZIO (c_2-c_1) is 0.176 Å. Due to the close-packed structure of hexagonal crystals, the expansion of c axis of one S substitution for O in $Zn_5In_2O_8$ is 2.64 Å. Thus, the degree of S substitution can be exhibited as $Zn_5In_2O_{8-x}S_x$ (x~ 0.07).

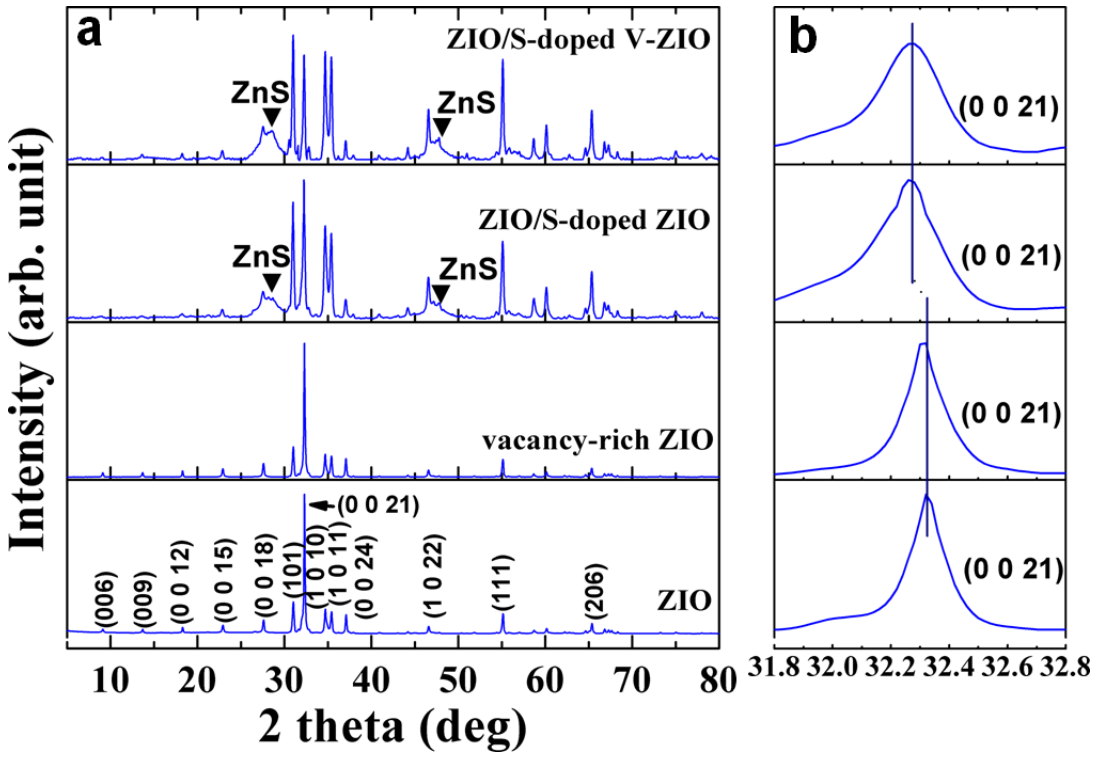

Figure 2.8 (a) XRD patterns and (b) enlarged (0 0 21) peaks of ZIO, vacancy-rich ZIO, ZIO/S-doped ZIO composite, and ZIO/S-doped V-ZIO composite.

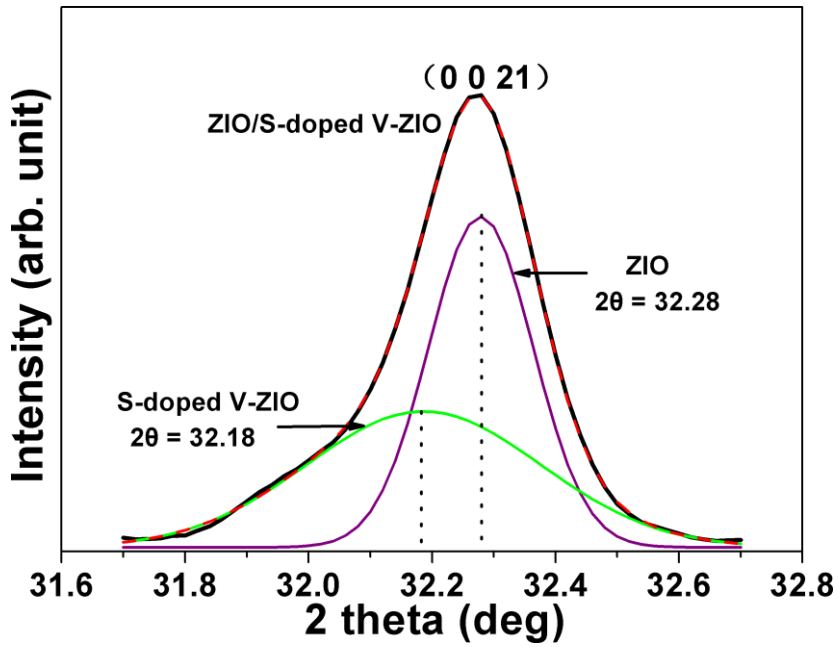

Figure 2.9 Peak-fitting of (0 0 21) of ZIO/S-doped V-ZIO composite XRD.

Figure 2.10 shows the UV-vis absorption spectra of ZIO/S-doped ZIO and ZIO/S-doped V-ZIO. They are red-shifted compared with those of ZIO and vacancy-rich ZIO, which can be explained by the bandgap narrowing due to a VB shift by the S 3*p* orbitals.

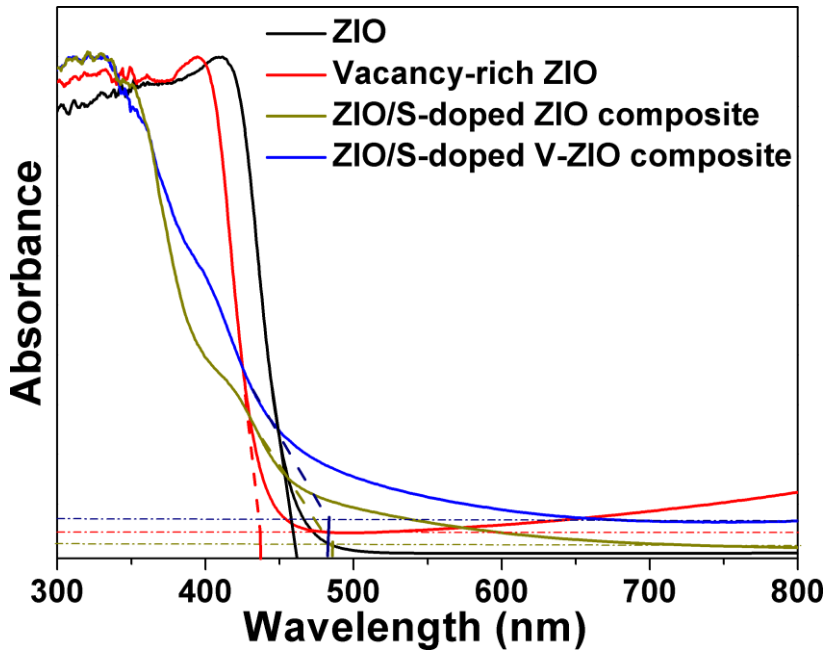

Figure 2.10 UV-vis absorption spectra of ZIO, vacancy-rich ZIO, ZIO/S-doped ZIO composite, and ZIO/S-doped V-ZIO composite.

XPS was employed for the surface analysis of ZIO/S-doped ZIO and ZIO/S-doped V-ZIO composites as shown in Figure 2.11. Peak positions were internally referenced to the C1s signal at 284.6 eV. The spectra exhibit the similar peaks of Zn, In, O, and S elements for the two composites. All the Zn 2*p*, In 3*d*, O 1*s*, and S 2*p* spectra consist of two peaks. The core lines are located at 1045.0 eV and 1022.0 eV for the Zn 2*p* level, 452.4 eV and 444.9 eV for the In 3*d* level, 533.3 eV and 532.0 eV for the O 1*s* level, and 168.7 eV and 161.8 eV for the S 2*p* level. The positions of Zn 2*p* and In 3*d* peaks are consistent with the spin orbit separations (23.0 eV for Zn 2*p* and 7.5 eV for In 3*d*). For O 1*s*, the 533.3 eV signal should belong to water absorbed on the sample surface [29], whereas the 532.0 eV peak is related to

the sample. The S 2*p* peak at 168.7 eV is due to the trace sulfate (SO_4^{2-}) adsorbed on the sample surface [30-33], which is the oxidation product of SO_3^{2-} by photogenerated holes [34], whereas the 161.8 eV signal is attributed to S^{2-} [35].

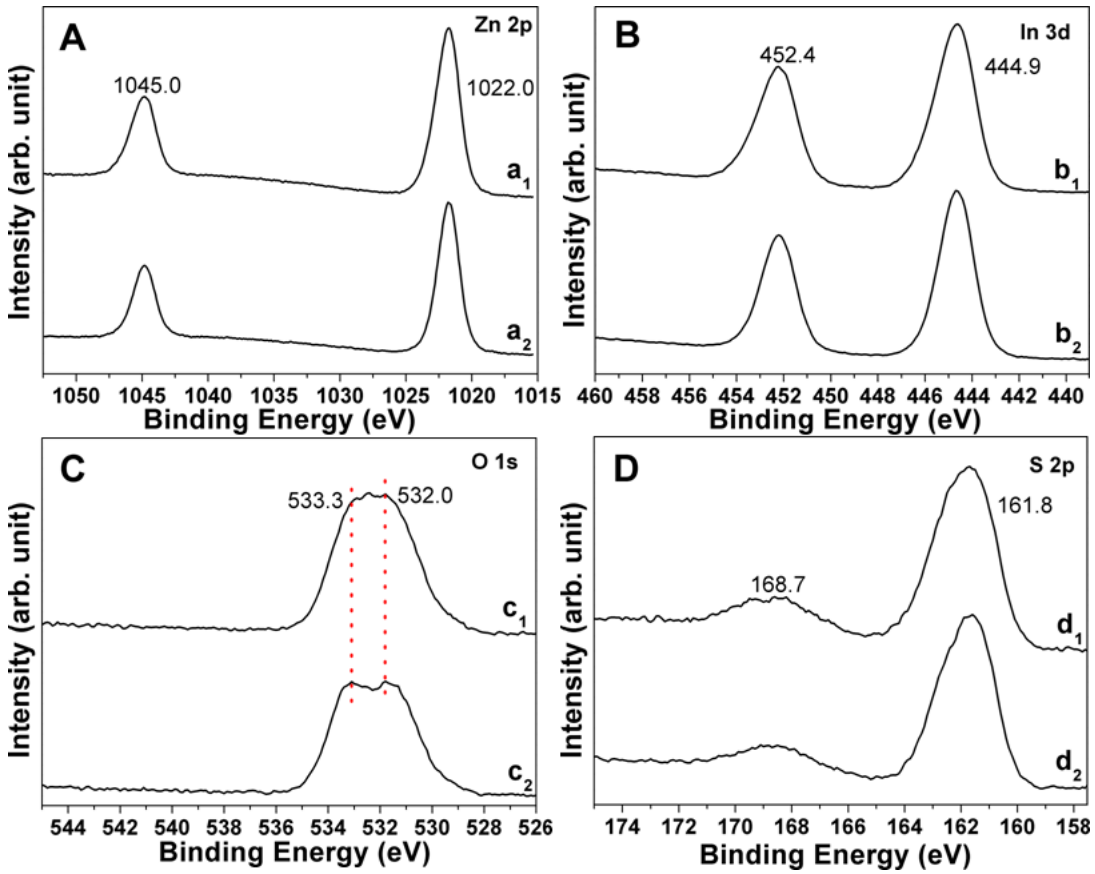

Figure 2.11(A) Zn 2*p*, (B) In 3*d*, (C) O 1*s*, and (D) S 2*p* XPS spectra of ZIO/S-doped ZIO (a_1, b_1, c_1, and d_1) and ZIO/S-doped V-ZIO composites (a_2, b_2, c_2, and d_2).

The structures of vacancy-rich ZIO and ZIO/S-doped V-ZIO composite were characterized by HRTEM as shown in Figure 2.12. The interplanar spacing of 2.88 Å in Figure 2.12(a) is consistent with the spacing between the (101) planes of hexagonal $Zn_5In_2O_8$. We could not probe the inner part of ZIO/S-doped V-ZIO (Figure 2.12(b)) owing to the large sample thickness in that area. S-doped V-ZIO has a polycrystalline structure, and the spacing of 3.2 Å in Figure 2.12(b) corresponds to the (0 0 18) planes of S-doped V-ZIO.

Figure 2.13 shows the STEM element mapping of ZIO/S-doped V-ZIO composite, which reveals homogeneous distribution of Zn, In, and O elements in the composite. However, the signal intensity of S element at the edge is stronger than that in the middle part as shown in the marked particle in Figure 2.13 (e), it means that the S anions were doped into the surface part of ZIO.

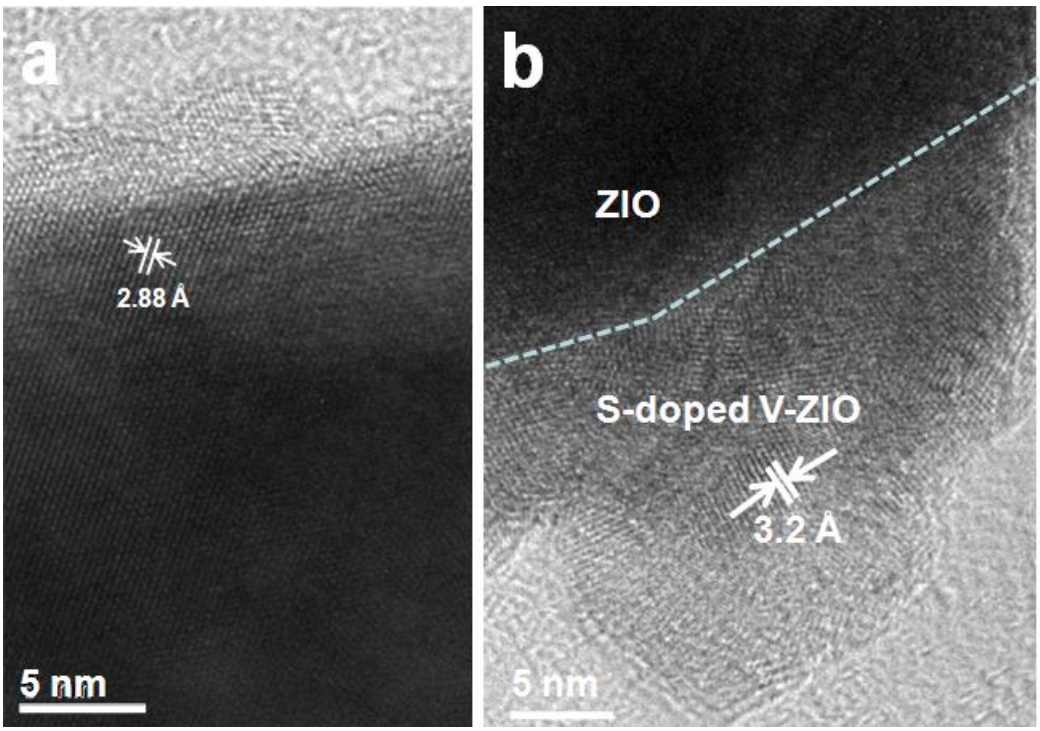

Figure 2.12 HRTEM images of (a) vacancy-rich ZIO and (b) ZIO/S-doped V-ZIO composite.

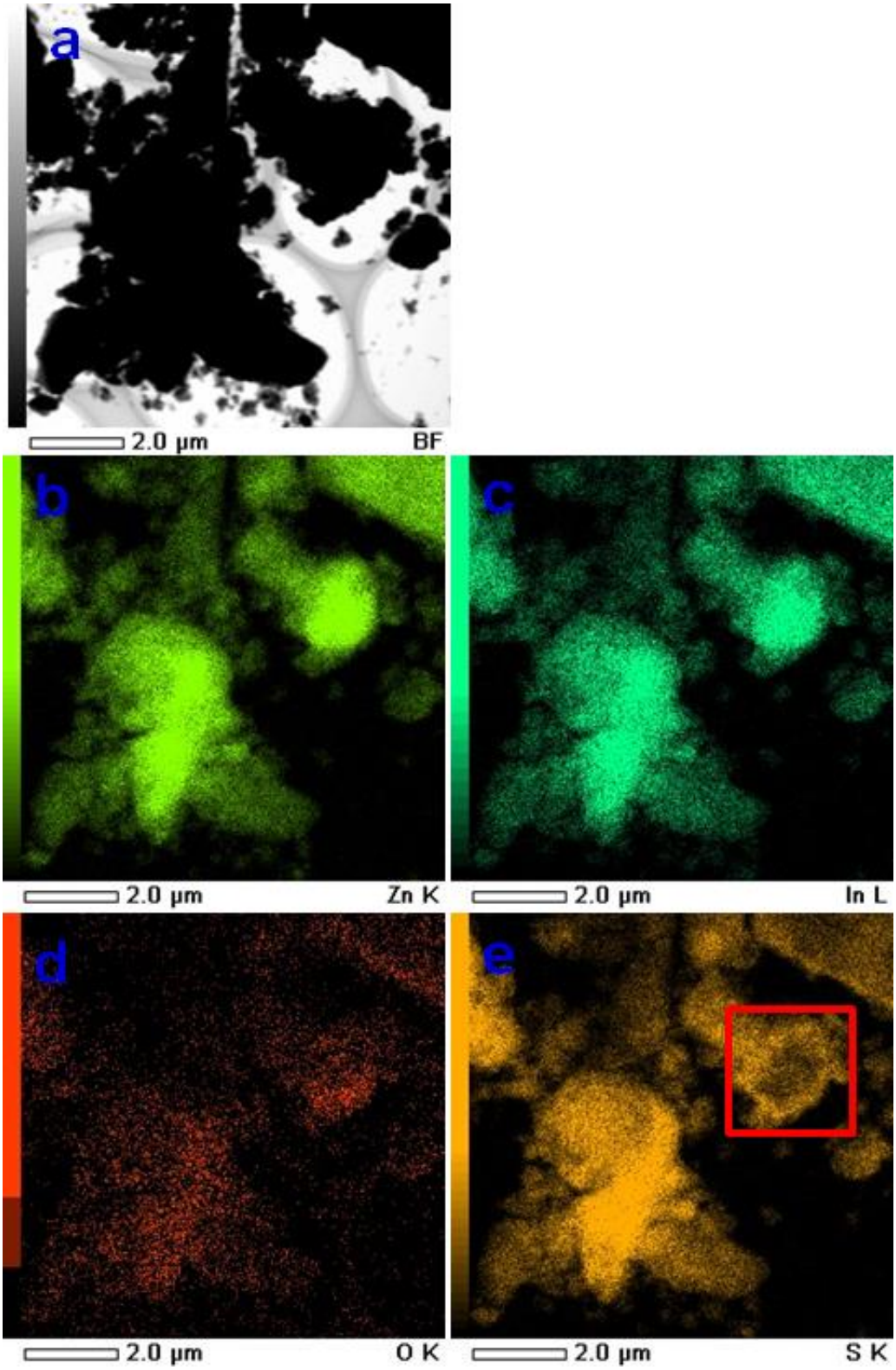

Figure 2.13 (a) STEM image and elemental maps of (b) Zn, (c) In, (d) O, and (e) S in the ZIO/S-doped V-ZIO composite.

2.6 The effects of Cu additive on the photocatalytic activity

In order to make clear the function of Cu metal powder in the fabrication process and other properties, controlled experiments were also carried out. The further treated conditions, being in Ar atmosphere and at 850 °C, were as the same as the process mentioned above. Figure 2.14 shows the XRD patterns of the ZIO, ZIO treated in the molten-salt with or without Cu metal powder after the treatment processes. The crystal structures of the treated samples were not changed.

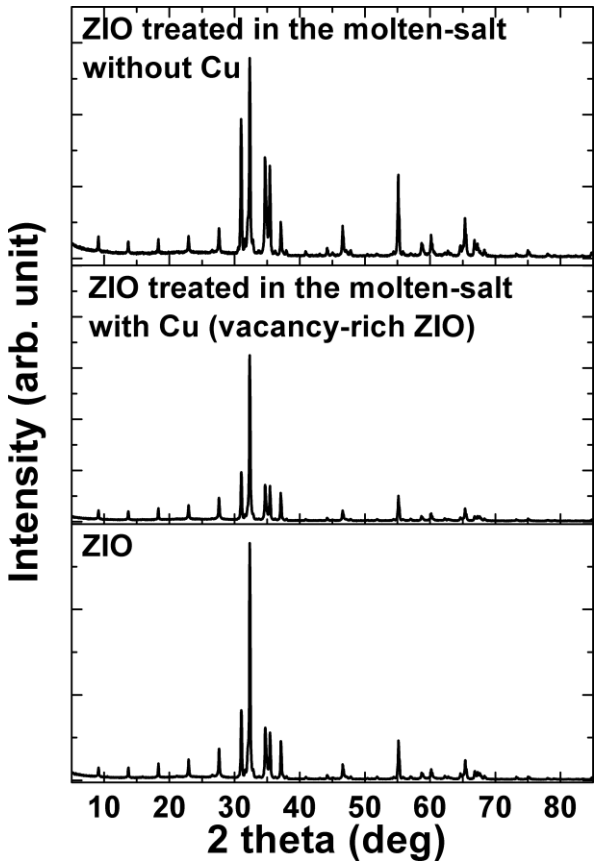

Figure 2.14 XRD patterns of (a) ZIO, (b) ZIO treated in the molten-salt with Cu, and (c) ZIO treated in the molten-salt without Cu.

Figure 2.15 and Figure 2.16 exhibit the SEM images and absorption spectra of ZIO, ZIO treated in the molten-salt with or without Cu metal powder. The morphologies after treatment

didn't show obvious transformation. Based on the above discussion, the blue-shift of the UV-vis absorption spectrum of vacancy-rich ZIO resulted from the indium vacancy. The UV-vis absorption spectrum of ZIO treated in the molten-salt without Cu doesn't show obvious shift in comparison with that of ZIO. Thus, the indium content in the ZIO treated in the molten-salt without Cu was not obviously changed after the treatment.

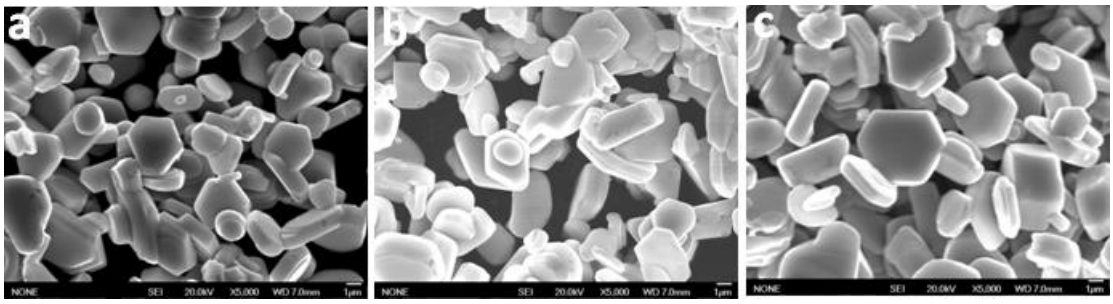

Figure 2.15 SEM images of (a) ZIO, (b) ZIO treated in the molten-salt with Cu, and (c) ZIO treated in the molten-salt without Cu.

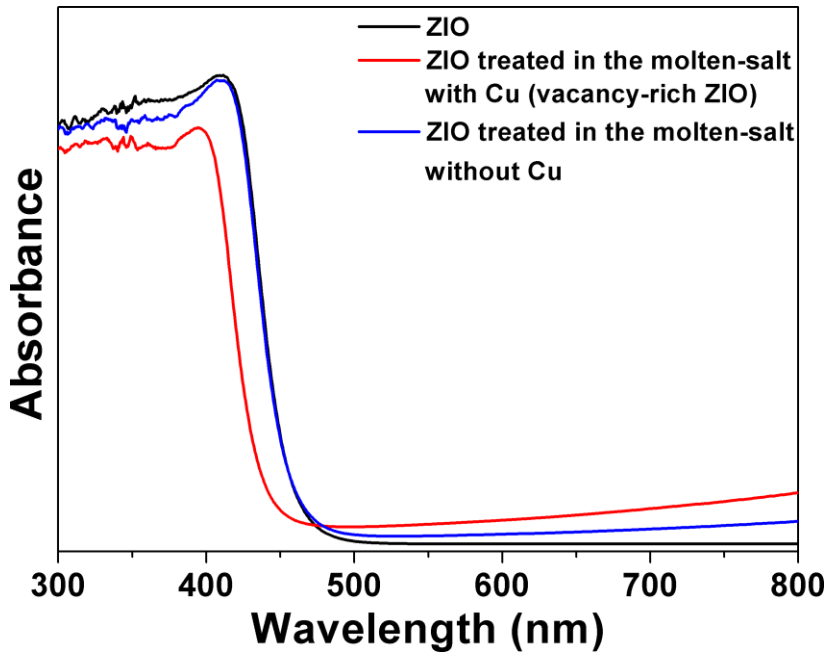

Figure 2.16 UV-vis absorption spectra of (a) ZIO, (b) ZIO treated in the molten-salt with Cu, and (c) ZIO treated in the molten-salt without Cu.

Before the photocatalytic H_2 evaluation under visible-light irradiation, 0.3 g of the sample treated in the molten-salt without Cu was also suspended in 270 ml Na_2S (0.35 M)-K_2SO_3 (0.25 M) aqueous solution containing $H_2PtCl_6 \cdot 6H_2O$ aqueous solution under continuous magnetic stirring. Then this mixture was irradiated using 300 W Xe lamp for 48 h. Figure 2.17 shows the H_2 evolution of surface-sulfurized ZIO and treated ZIO in the molten-salt with or without Cu metal powder under visible-light irradiation. The photocatalytic H_2 evolution rates of ZIO and ZIO treated in the molten-salt without Cu powder were similar. However, the photocatalytic activity of ZIO treated in the molten-salt with Cu powder was greatly enhanced at about 17 times higher as mentioned above. Therefore, the addition of Cu in the treatment process could promote the formation of indium vacancies, which played a significant role in enhancing the photocatalytic activity.

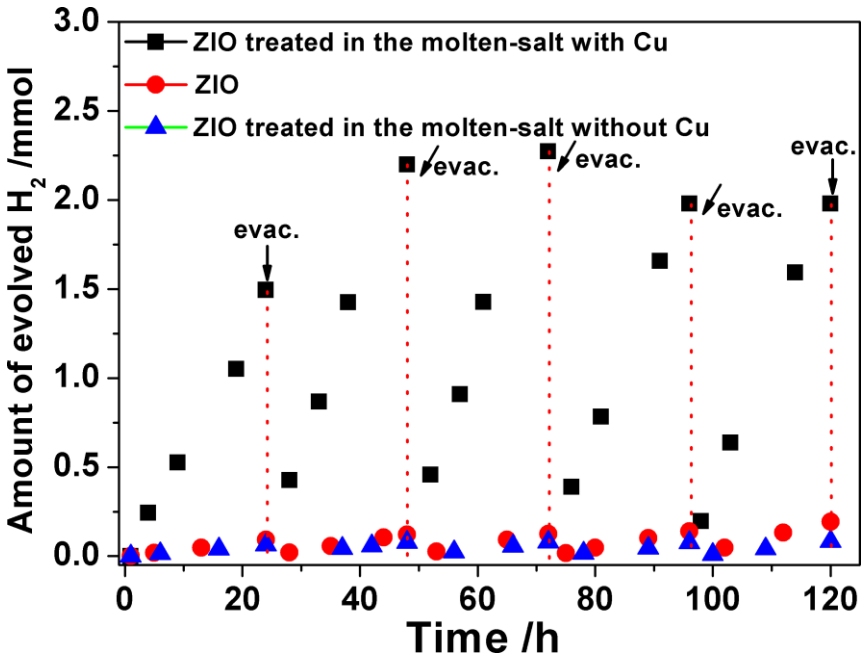

Figure 2.17 Time course of H_2 evolution under visible-light irradiation ($\lambda > 400$ nm). (a) ZIO treated in the molten-salt with Cu, (b) ZIO, and (c) ZIO treated in the molten-salt without Cu powder.

2.7 Reason of the enhanced photocatalytic activity

As mentioned above, indium vacancies were produced by the high-temperature treatment in Ar atmosphere, as confirmed by the increased Zn/In molar ratio in vacancy-rich ZIO compared with ZIO. The vacancies were introduced near the surface because the color of the vacancy-rich ZIO changed from blue to yellow after being milled. The In deficiency on the surface resulted in the blue-shift of the UV-vis absorption spectrum due to the bandgap widening in vacancy-rich ZIO. Metal oxide/surface-S-doped metal oxide composites were successfully synthesized, although very small amount of ZnS was detected as impurity in both ZIO/S-doped ZIO and ZIO/S-doped V-ZIO composites. ZnS did not affect the photoactivity of the two composites because it has a wide bandgap (~ 3.7 eV) and is therefore insensitive to visible light [36]. The formation of S-doped oxides on ZIO and vacancy-rich ZIO samples was confirmed by XRD, UV-vis absorption spectra, EDX, XPS, HRTEM, and STEM elemental mapping. The photocatalytic H_2 evolution rate of ZIO/S-doped V-ZIO composite was 17 times higher than that of ZIO/S-doped ZIO.

To make clear comparison between photocatalytic activities of S-doped V-ZIO and ZIO/S-doped V-ZIO composite, I have tried to fabricate the pure phase of S-doped V-ZIO by several methods such as the sulfuration of vacancy-introduced ZIO in the dense aqueous Na_2S solution under hydrothermal condition. However, I failed to fabricate it. On the other hand, the experimental results indicated: 1) Pt-loaded ZIO did not show any photocatalytic activity for H_2 evolution in aqueous methanol solution under visible-light irradiation by using methanol as the sacrificial reagent; 2) ZIO/S-doped ZIO composite showed a much higher H_2 evolution rate (several micromolar per hour) by using Na_2S/K_2SO_3 as the sacrificial reagents; 3) ZIO/S-doped V-ZIO composite showed a further and intensively enhanced activity. Therefore, the enhanced photocatalytic activity didn’t result from the S-doped V-ZIO itself.

The relative absorptivity could be gained by Kubellka-Munk conversion based on the UV-vis Diffuse Reflectance Spectra. Therefore, for the ZIO/S-doped ZIO and ZIO/S-doped V-ZIO composites, the relation between the relative number of absorbed photons ($N_{abs}(\lambda)$) and the number of incident photons ($N_{inc}(\lambda)$) at wavelength λ is as follows.

$$N_{abs}(\lambda) = N_{inc}(\lambda) * I_{ab}$$

Thus, the total relative absorbed photons in the visible-light region can be calculated as follows.

$$\sum_{420}^{800} N_{abs}(\lambda) = \sum_{420}^{800} N_{inc}(\lambda) * I_{ab} = \sum_{420}^{800} \frac{IAt\lambda}{hc} * I_{ab}$$

$$= 8.04 \times 10^{10} \sum_{420}^{800} I\lambda t * I_{ab}$$

in which *I*, *A*, *t*, *h*, *c*, and I_{ab} are the light intensity, irradiation area (16 cm^2), irradiation time, Planck constant, speed of light, and relative absorptivity, respectively. The light intensity can be measured by a light intensity meter and UV-vis absorption meter, respectively.

The absorbed light ratio and AQE around 418.5 nm of the two composites are shown in Table 2.2.Although the light absorption of ZIO/surface-S-doped V-ZIO composite is about 2 times than that of the ZIO/surface-S-doped ZIO composite, the AQE is much higher than that of the ZIO/surface-S-doped ZIO composite. Thus the enhanced photocatalytic activity of ZIO/surface-S-doped V-ZIO composite was not caused by the enhanced light absorption. As mentioned above, the surface areas of ZIO/surface-S-doped ZIO and ZIO/surface-S-doped V-ZIO composites are 43.8 m^2/g and 26 m^2/g, respectively. These results mean that the average size of ZIO/surface-S-doped ZIO composite is smaller than that of the ZIO/surface-S-doped V-ZIO composite. Therefore, the particle size didn't show obvious positive roles in enhancing the photocatalytic activities in this work. In consideration of all these facts together, it can be reasonably considered that the enhanced activity in ZIO/S-doped V-ZIO composite should be

mainly attributed to the more efficient separation ability of photoexcited electrons and holes in the ZIO/S-doped V-ZIO composite.

Table 2.2 Comparison of light absorption and AQE of the two composites.

Sample	Light absorption (ratio)	AQE (around 418.5 nm)
ZIO/surface-S-doped ZIO	1	0.04%
ZIO/surface-S-doped V-ZIO	2	5.2%

The possible explanation for the enhancement of photocatalytic activity based on the band diagrams of S-doped V-ZIO and S-doped ZIO composites is shown in Figure 2.18. The CB bottom of S-doped V-ZIO synthesized from vacancy-rich ZIO is shifted up compared with that of ZIO as shown in Figure 2.18 (a), whereas the CBs have the same energies in S-doped ZIO and ZIO as shown in Figure 2.18 (b). However, the UV-vis absorption spectra are redshifted (Figure 2.10) both for ZIO/S-doped ZIO and ZIO/S-doped V-ZIO because the VB

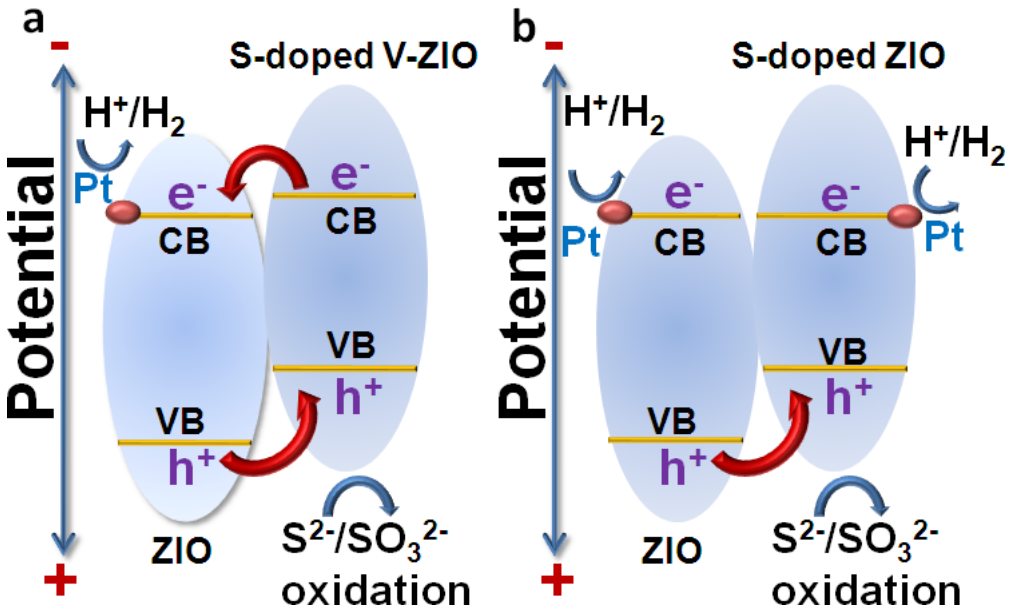

Figure 2.18 Schematic mechanism of electron-hole pair separation in (a) ZIO/S-doped V-ZIO and (b) ZIO/S-doped ZIO composites.

top was lifted up by the S 3*p* orbitals. For the ZIO/S-doped V-ZIO composite, ZIO and S-doped V-ZIO have different potentials both for CB and VB. These different potentials result in a more efficient separation of electron-hole pairs and thus result in a higher photocatalytic activity.

2.8 Conclusions

(I) Microstructure $Zn_5In_2O_8$ (ZIO) with high crystallinity has been successfully synthesized by a NaCl/KCl molten-salt method at 1200 °C for 3 h.

(II) A photo-assisted method has been developed for fabricating $Zn_5In_2O_8$ (ZIO)/Surface-S-doped oxide composites using vacancy-rich ZIO (V-ZIO) as the precursor. The composite exhibited much higher photocatalytic activity for H_2 evolution in a Na_2S/K_2SO_3 aqueous solution under visible-light irradiation than the composite prepared using conventional ZIO.

(III) It was found that Cu metal powder played an important role in the formation of indium vacancies which showed significant impacts on the enhancement of photocatalytic activity. On the other hand, Na_2S could act as not only a sacrificial reagent, but also a chemical reagent to form an S-doped oxide layer.

(IV) The indium vacancies resulted in a more negative conduction band of S-doped V-ZIO in comparison with that of ZIO. Then, the photoexcited electrons transferred from the conduction band of S-doped V-ZIO to that of ZIO. On the other hand, the photoexcited holes transferred from the valence band of ZIO to that of S-doped V-ZIO. The enhanced photocatalytic activity was related to the more efficient separation of photogenerated electrons and holes and the utilization of incident light. Our results provide useful information for improving the activity of photocatalysts.

References

[1] Chiarello G L, Selli E and Forni L 2008 *Appl. Catal. B: Environ.* **84** 332.

[2] Ding Q P, Yuan Y P, Xiong X, Li R P, Huang H B, Li Z S, Yu T, Zou Z G and Yang S G 2008 *J. Phys. Chem. C* **112** 18846.

[3] Hu C C and Teng H 2010 *J. Catal.* **272** 1.

[4] Kato H, Asakura K and Kudo A 2003 *J. Am. Chem. Soc.* **125** 3082.

[5] Chen D and Ye J H 2009 *Chem. Mater.* **21** 2327.

[6] Yi Z G, Ye J H, Kikugawa N, Kako T, Ouyang S X, Stuart-Williams H, Yang H, Cao J Y, Luo W, J, Li Z S, Liu Y and Withers R L 2010 *Nat. Mater.* **9** 559.

[7] Tong H, Ouyang S X, Bi Y P, Umezawa N, Oshikiri M and Ye J H 2012 *Adv. Mater.* **24** 229.

[8] Katayama M, Yokoyama D, Maeda Y, Ozaki Y, Tabata M and Matsumoto Y 2010 *Mater. Sci. Eng.B* **173** 275.

[9] Zhang FX, Maeda K, Takata T and Domen K 2010 *Chem. Commun.* **46** 7313.

[10] Wang D F, Ye J H, Kako T and Kimura T 2006 *J. Phys. Chem. B* **110** 15824.

[11] Bang J H, Helmich R J and Suslick K 2008 *Adv. Mater.* **20** 2599.

[12] Asahi R, Morikawa T, Ohwaki T, Aoki K and Taga Y 2001 *Science* **293** 269.

[13] Ouyang S X, Tong H, Umezawa N, Cao J Y, Li P, Bi Y P, Zhang Y J and Ye J H 2012 *J. Am. Chem. Soc.* **134** 1974.

[14] Ikarashi K, Sato J, Kobayashi H, Saito N, Nishiyama H and Inoue Y 2002 *J. Phys. Chem. B* **106** 9048.

[15] Yoshinari A, Ishida K, Murai K I and Moriga T 2009 *Mater. Res. Bull.* **44** 432.

[16] Kudo A and Mikami I 1998 *Chem. Lett.* **27** 1027.

[17] Ng J W, Xu S P, Zhang X W, Yang H Y and Sun D D 2010 *Adv. Funct. Mater.* **20** 4287.

[18] Lu X J, Huang F Q, Mou X L, Wang Y M and Xu F F 2010 *Adv. Mater.* **22** 3719.

[19] Zhang J, Xu Q, Feng Z C, Li M J and Li C 2008 *Angew. Chem. Int. Ed.* **47** 1766.

[20] Lv J, Kako T, Zou Z G and Ye J H 2009 *Appl. Phys. Lett.* **95** 032107.

[21] Kudo A and Miseki Y 2009 *Chem. Soc. Rev.* **38** 253.

[22] Penn R L and Banfield J F 1998 *Science* **281** 969.

[23] Diebold U 2003 *Surf. Sci. Rep.* **48** 53.

[24] Kasper H 1967 *Z. Anorg. Aug. Chem.* **349** 113.

[25] Nadaud N, Nanot M and Boch P 1994 *J. Am. Ceram Soc.* **77** 843.

[26] Luo W J, Li Z S, Jiang X J, Yu T, Liu L F, Chen X Y, Ye J H and Zou Z G 2008 *Phys. Chem. Chem. Phys.* **10** 6717.

[27] Zhou X H, Hu Q H and Fu Y 2008 *J. Appl. Phys.* **104** 063703.

[28] Lupan O, Pauporté T, Bahers T L, Viana B and Ciofini I 2011 *Adv. Funct. Mater.* **21** 3564.

[29] Fan L and Guo R 2008 *J. Phys. Chem. C* **112** 10700.

[30] Naik B, Parida K M and Gopinath C S 2010 *J. Phys. Chem. C* **114** 19473.

[31] Periyat P, McCormack D E, Hinder S J and Pillai S C 2009 *J. Phys. Chem. C* **113** 3246.

[32] Lv Y Y, Ding Y, Zhou J H, Xiao W M and Feng Y Y 2009 *J. Am. Ceram. Soc.* **92** 938.

[33] Szatmary L, Bakardjieva S, Subrt J, Bezdicka P, Jirkovsky J, Bastl Z, Brezova V and Korenko M 2011 *Catal. Today* **161** 23.

[34] Kudo A, Tsuji I and Kato H 2002 *Chem. Commun.* 1958.

[35] Chen Z X, Li D Z, Zhang W J, Chen C, Li W J, Sun M, He Y H and Fu X Z 2008 *Inorg. Chem.* **47** 9766.

[36] Zhang Q, Chi W Y, Zhang W W, Lv C Y and Li J X 2012 *New. J. Chem.* **36** 119.

Chapter 3 Indium Sulfide/Zinc Indium Sulfide ($In_2S_3/ZnIn_2S_4$) Bulk Composite for Photocatalytic Water Splitting

3.1 Introduction

As mentioned in Chapter 2, development of clean and renewable energy is an urgent task for researchers because of the decreasing fossil fuels and the increasing environmental problems. Photocatalytic water splitting for H_2 evolution attracts plenty of research interest, of which the prime bottleneck is the separation and migration ability of the photoexcited e^-/h^+ pairs [1, 2]. It has been well-documented that an appropriate semiconductor composite with different band potentials can greatly enhance the separation efficiency of such pairs [3, 4]. However, the improved separation ability was dominated by the contact electric field at the interface of a semiconductor composite [5-8]. Consequently, tight contact between the semiconductors in a composite is significant for the efficient separation and migration of the photogenerated electrons and holes. In this case, the electric-field-assisted charge transport from one particle to the other via interfaces is beneficial to enhance the separation ability of photoexcited electrons and holes in the coupled semiconductors. Lin *et al.* fabricated $Bi_2O_3/BaTiO_3$ heterojunction semiconductors by a milling-annealing method [6]. They found that the heterojunction semiconductors showed much better photocatalytic activities than the single-phase $BaTiO_3$ and Bi_2O_3. Figure 3.1 shows the electron-hole separation driven by electric field.

Generally, photocatalytic semiconductor composites can be synthesized by various routes, including impregnation method [9], hydrothermal technique [10], physical milling [11], and soft template method [12], etc. However, the composites synthesized by these methods usually suffer from a poor contact, big particle size, and inhomogeneous distribution

of the components, which are not beneficial to the effective separation and migration of the photoexcited e^-/h^+ pairs.

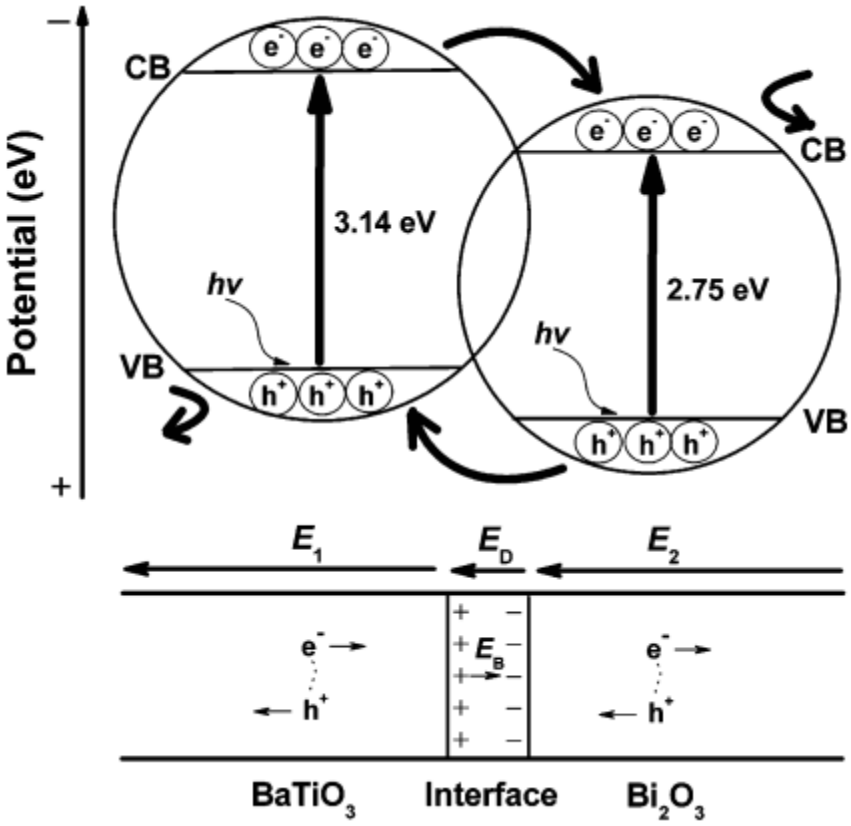

Figure 3.1 Sketch map for electric-field-driven electron-hole separation at the interface and in both semiconductors. E_D: contact electric field induced by the difference of band potentials of two materials; E_B: potential barrier in the interfacial depletion layer ($E_B < E_D$ during the nonequilibrium process of a photocatalytic reaction); E_1 and E_2 are the internal electric fields induced by the redistribution of the spatial charges in $BaTiO_3$ and Bi_2O_3 particles, respectively. Reproduced from ref. [6].

Bulk composites (interpenetrating networks formed by two semiconductors), with fluent interface and evenly distributed components, can easily transfer and dissociate the excited carriers (e^-/h^+ pairs) at the interface [13], which is an excellent strategy to design highly

active photocatalysts. As shown in Figure 3.2 (a), the photoexcited electrons and holes of conventional semiconductor composites must cover a long way to the surface of the semiconductor. It enhances the recombination probability of the carriers during this process. However, the carriers just need to cover a much shorter distance to the interface in the highly distributed bulk composite as shown in Figure 3.2 (b). This is very beneficial to the efficient separation of the photoexcited charges. Hence, it is significant to develop effective and convenient routes for the synthesis of efficient bulk-composite photocatalysts.

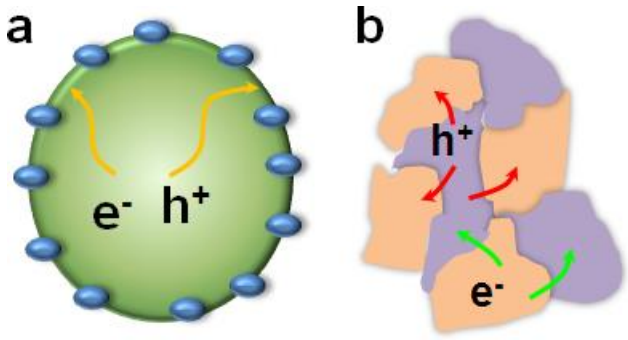

Figure 3.2 Schematic pictures of the migration of the photoexcited electrons and holes in (a) conventional semiconductor composites and (b) bulk composites.

The sulfide photocatalysts, such as ZnS-based solid solutions [14, 15] and CdS-based composites [16-18], have been devoted intense research interests because of their excellent photocatalytic activities for H_2 evolution under visible-light irradiation. However, the band gaps of the highest efficient photocatalysts among them were too large, because a highly efficient photocatalyst which can be sensitized by visible light up to 600 nm and even longer wavelengths (E_g is around 2.1 eV) is crucial for the practical application [19]. In_2S_3, with a band gap of 2.0-2.2 eV for its bulk form, has been paid a decent attention with respect to its photoelectric conversion material own to its efficient absorption of visible light, high photosensitivity and photoconductivity [20]. This compound generally exhibits in three

different phases, namely α, β, and γ, among which β-In_2S_3 with a defective spinel structure attracts much research interest as a photocatalyst for dye degradation or water splitting [21-24]. In addition, In_2S_3 was also used as a component of solid solution or a visible-light-sensitizer of the wide band gap semiconductor [25-27]. Recently, it was reported that Zn-In-S composites containing In_2S_3 have been successfully synthesized by a hydrothermal route [28]. However, the photocatalytic activities of the composites for H_2 evolution were worse than that of the single $ZnIn_2S_4$ phase, because In_2S_3 increased the recombination of photoinduced electrons and holes. As a result, more efforts should be devoted to develop efficient In_2S_3-based composite photocatalysts.

In order to more efficiently utilize the incident light and further enhance the separation and migration ability of the photoexcited carriers, an $In_2S_3/ZnIn_2S_4$ bulk composite photocatalyst was synthesized through an ion-exchange route, which is effective for synthesizing high active photocatalysts [29, 30]. This bulk composite was fabricated by using $NaInS_2$ as a homogeneous precursor under solvothermal conditions and showed high crystallinity and nanoscale dimensions. When two different kinds of reagents were added into the reaction system containing this precursor, the Na^+ was exchanged by the cations of the added reagents. Subsequently, the In_2S_3 and $ZnIn_2S_4$ components were *in situ* produced and $In_2S_3/ZnIn_2S_4$ bulk composite was simultaneously formed during this process. The photocatalytic H_2 evolution of this special composite under visible-light irradiation was greatly enhanced in comparison with those of the two individual components (In_2S_3 and $ZnIn_2S_4$).

3.2 Experimental section

The reagents were sodium sulfide nonahydrate ($Na_2S·9H_2O$), indium chloride tetrahydrate ($InCl_3·4H_2O$), zinc chloride ($ZnCl_2$), magnesium chloride hexahydrate

($MgCl_2·6H_2O$), ethylene glycol dehydrated ($HOCH_3CH_3OH$; EG), and ethanol dehydrated (CH_3CH_2OH). They were of analytical grade and used without further treatment.

3.2.1 Synthesis of hierarchical $NaInS_2$ microflowers

In a typical process, 50 ml of EG and 50 ml of absolute ethanol were magnetically stirred and mixed for 10 min in a beaker, then 2 mmol of $InCl_3·4H_2O$ was added into the mixed organic solution and continuously stirred for 15 min, and then 12 mmol of $Na_2S·9H_2O$ was added into the solution and stirred for another 30 min. Finally, the mixture was transferred into a Teflon liner with 120-ml capacity, which was subsequently sealed in a stainless steel autoclave and heated at 180 °C for 12 h. The autoclave was cooled to room temperature naturally and the products were washed by distilled water and absolute ethanol for several times, respectively. After drying at 70 °C in an oven, the products were collected for further characterizations and treatments.

3.2.2 Synthesis of $In_2S_3/ZnIn_2S_4$ bulk composite

For the synthesis of an $In_2S_3/ZnIn_2S_4$ bulk composite, *x* mmol of $ZnCl_2$, (2-*x*) mmol of $MgCl_2·6H_2O$, and 1 mmol of the as-synthesized $NaInS_2$ were added into the mixture of absolute ethanol (97 ml) and pure water (3 ml), which were filled in a Teflon liner with 120 ml capacity. After totally dissolving of $ZnCl_2$ and $MgCl_2·6H_2O$ by manual stirring, the Teflon liner was sealed in a stainless steel autoclave and heated at 200 °C for 24 h in an oven. The whole system was cooled to room temperature naturally, and the products were washed with distilled water and ethanol for several times, respectively. Finally, the products were dried at 70 °C for further characterization. As a reference, In_2S_3 and $ZnIn_2S_4$ were fabricated by the similar procedure. When the starting reagents were 2 mmol of $MgCl_2·6H_2O$ and 1 mmol of $NaInS_2$, the products were In_2S_3.The products became $ZnIn_2S_4$ when the starting reagents were 2 mmol of $ZnCl_2$ and 1 mmol of $NaInS_2$. The possible reactions involved in the

fabrication process of In_2S_3, $ZnIn_2S_4$, and $In_2S_3/ZnIn_2S_4$ bulk composite are written as in equations (1)-(3), respectively. The MgS product along the equation (1) or (3) must dissolve in the reaction solution because no peaks of it were detected on the XRD patterns presented in the subsequent Figure3.5.

$$NaInS_2 + MgCl_2 \cdot 6H_2O \rightarrow In_2S_3 + MgS + NaCl + H_2O \quad (1)$$

$$NaInS_2 + ZnCl_2 \rightarrow ZnIn_2S_4 + NaCl \quad (2)$$

$$NaInS_2 + MgCl_2 \cdot 6H_2O + ZnCl_2 \rightarrow In_2S_3/ZnIn_2S_4 + MgS + NaCl + H_2O \quad (3)$$

3.2.3 Characterization

Powder X-ray diffraction (XRD) characterization was performed by using an X'Pert PRO X-ray diffraction system (PAN alytical B.V., Netherlands) operating at 45 kV and 40 mA for Cu Kα radiation (λ = 1.5406 Å). The UV-visible diffuse reflection spectra were recorded on a UV-2500PC recording spectrophotometer (Shimadzu Co., Japan). The reflectance spectra were converted into absorption spectra using the Kubelka-Munk equation. Transmission electron microscopy (TEM) and high-resolution TEM (HRTEM), scanning transmission electron microscopy and elemental mapping (STEM elemental mapping) were performed on a 300 kV JEM-3100 FEF (JEOL, Japan) microscope. The photocatalytic evolved H_2 was analyzed by an on-line gas chromatography (GC-8A, Shimadzu Co., Japan) equipped with a thermal conductivity detector (TCD). Apparent quantum efficiency (AQE) was calculated by the following equation:

$$AQE(\%) = \frac{\text{The number of reacted electrons}}{\text{The number of incident photons}} \times 100\%$$

$$= \frac{\text{The number of evolved } H_2 \text{ molecules} \times 2}{\text{The number of incident photons}} \times 100\%$$

3.3 Results and discussion

3.3.1 Morphology and crystal structure

Figure 3.3 shows the XRD pattern of the as-synthesized $NaInS_2$, it can be seen that the products exhibit high crystallinity without impurity. Figure 3.4 is the typical SEM images of the as-synthesized $NaInS_2$ at low and high magnifications. The products are hierarchical microflowers consisting of nanoplates of ca. 100 nm in thickness, as marked in the inset in Figure 3.4 (b).

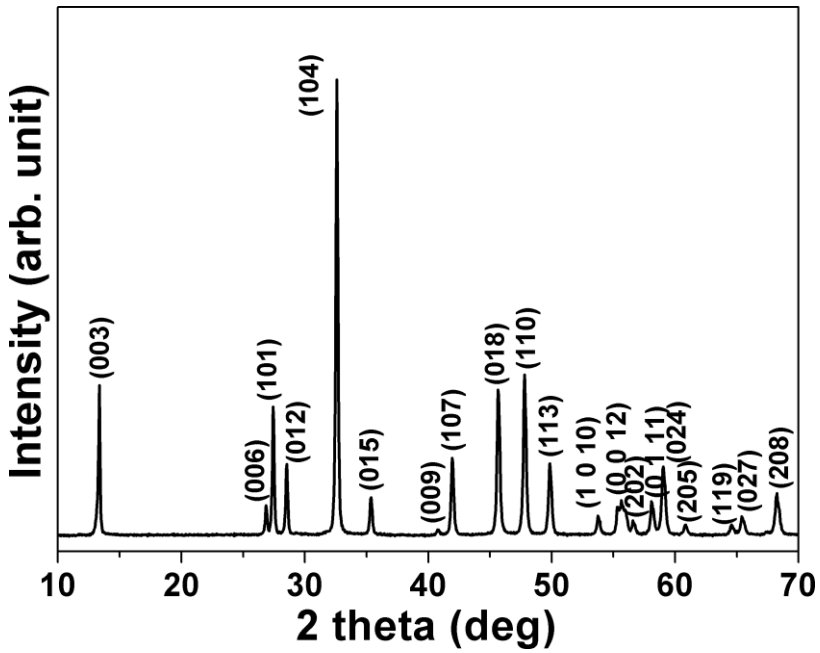

Figure 3.3 XRD pattern of as-synthesized $NaInS_2$.

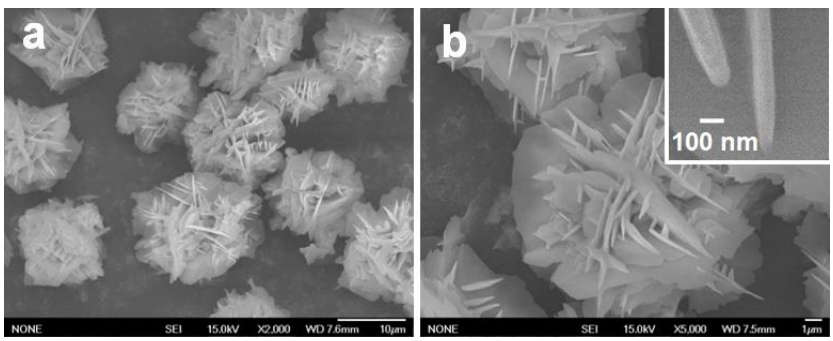

Figure 3.4 SEM images of as-synthesized $NaInS_2$ at different magnifications.

In order to make clear the function of solvent in the fabrication process, we tried to synthesize $ZnIn_2S_4$ using $NaInS_2$ and $ZnCl_2$ as the starting reagents at various conditions, such as different solvents and different reaction temperatures. Figure 3.5 exhibits the XRD patterns of the products synthesized in the 100 ml of water solvent, namely, hydrothermal method at different reaction temperature. The amounts of staring materials, $NaInS_2$ and $ZnCl_2$, were 1 mmol and 2 mmol, 2 mmol and 1 mmol, 2 mmol and 1 mmol, respectively. As shown in Figure 3.5 (A), when there were excessive $ZnCl_2$ in the reaction system and the reaction occurred at high temperature, there were obvious peaks belonging to $In(OH)_3$ which were marked with circle symbols. However, when we decreased the amount of $ZnCl_2$ and the reaction temperature, the main product was $In_{2.77}S_4$ marked with five-pointed stars, though the intensity of $In(OH)_3$ peaks as shown in Figure 3.5 (B) and (C).

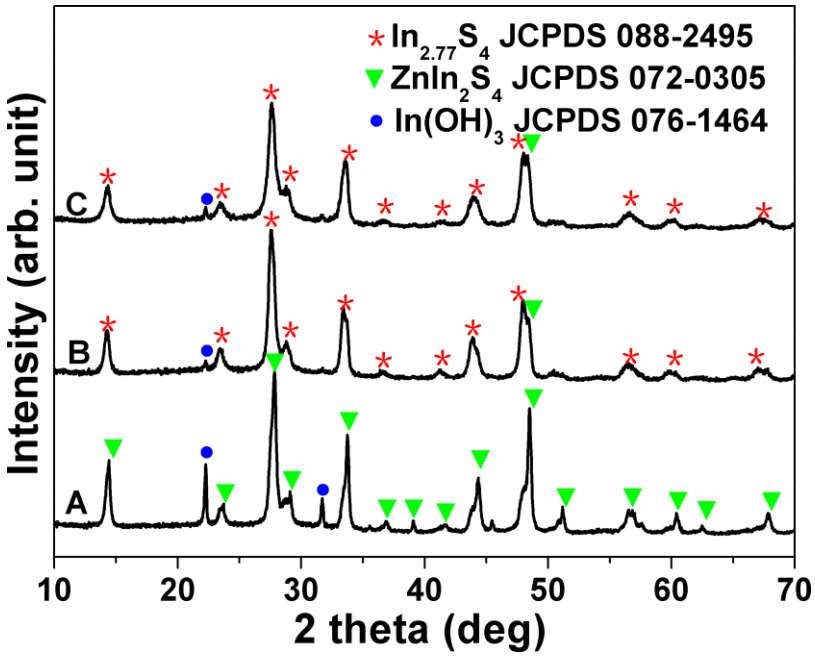

Figure 3.5 XRD patterns of the products. (A) $ZnCl_2$: 2 mmol, $NaInS_2$: 1 mmol, 180 °C, 12 h. (B) $ZnCl_2$: 0.5 mmol, $NaInS_2$: 1 mmol, 160 °C, 12 h. (C) $ZnCl_2$: 0.5 mmol, $NaInS_2$: 1 mmmol, 120 °C, 12 h.

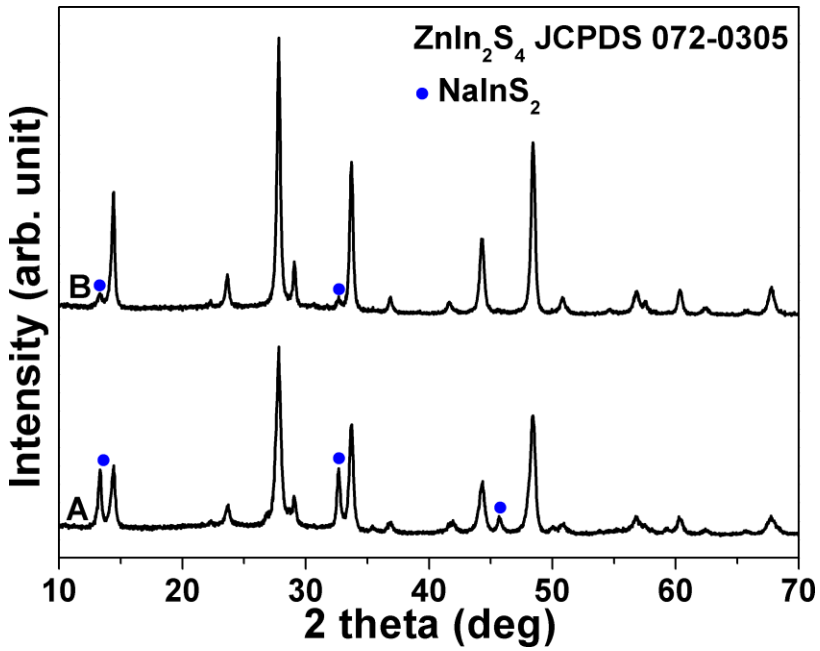

Figure 3.6 XRD patterns of (A) $ZnCl_2$: 4 mmol, $NaInS_2$:1 mmol, 160 °C, 12 h; (B) $ZnCl_2$: 8 mmol, $NaInS_2$:1 mmol, 200 °C, 12 h.

There were hydroxides in the products when we used water as the solvent. Thus, we tried to use organic solvent to synthesize $ZnIn_2S_4$. Figure 3.6 shows the XRD patterns of the products in the absolute ethanol with different amounts of $ZnCl_2$ at different reaction temperature. As shown in Figure 3.6 (A), $NaInS_2$ was not totally transformed into $ZnIn_2S_4$ when 4mmol of $ZnCl_2$ and 1 mmol of $NaInS_2$ reacted in 100 ml of absolute ethanol at 160 °C for 12 h. Then the amount of $ZnCl_2$ was increased to 8 mmol and the reaction temperature was increased to 200 °C, there was still weak peaks belonging to $NaInS_2$. Based on the above results, the solvent was the key to prepare pure $ZnIn_2S_4$, and pure $ZnIn_2S_4$ can be synthesized by using appropriate absolute ethanol and pure water as the solvent.

As mentioned in the Experimental Section, $In_2S_3/ZnIn_2S_4$ bulk composites have been successfully synthesized using $NaInS_2$, appropriate $MgCl_2 \cdot 6H_2O$ and $ZnCl_2$ as the starting reagents in the mixture solvent of absolute ethanol and pure water. As a reference, In_2S_3 and $ZnIn_2S_4$ were fabricated by the similar procedure. Figure 3.7 shows the XRD patterns of the

as-synthesized In_2S_3 and $ZnIn_2S_4$. According to the obtained patterns, $NaInS_2$ was totally transformed into pure tetragonal In_2S_3 (JCPDS 73-1366) and cubic $ZnIn_2S_4$ (JCPDS 72-0305) after the ion-exchange reaction, respectively, because no peaks of $NaInS_2$ can be detected by XRD after the reaction.

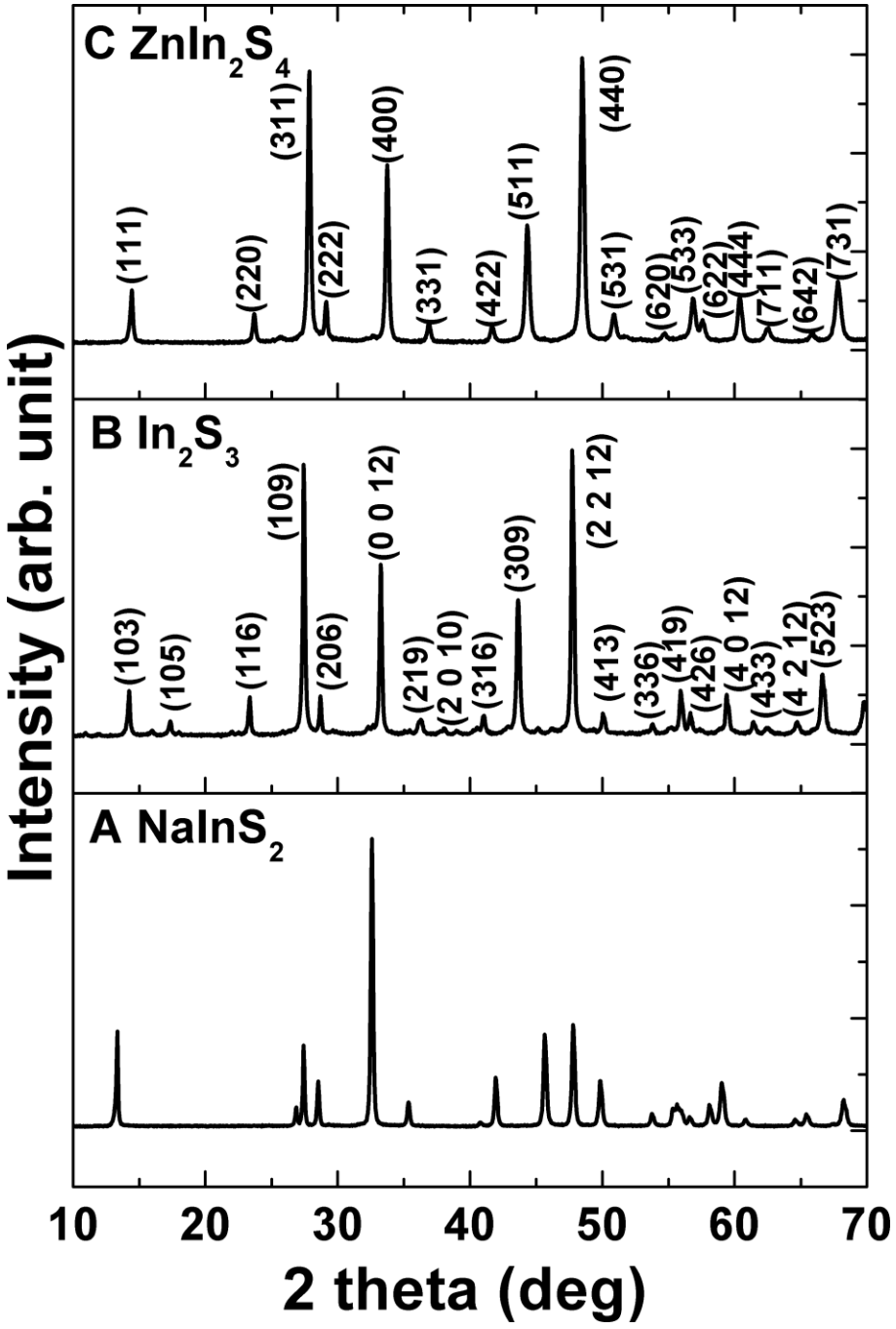

Figure 3.7 XRD patterns of as-synthesized (A) $NaInS_2$, (B) In_2S_3, and (C) $ZnIn_2S_4$.

Figure 3.8 shows SEM images of the synthesized In_2S_3 and $ZnIn_2S_4$, the morphologies don't show obvious transformation in comparison with that of the $NaInS_2$ precursor. The TEM and HRTEM images of In_2S_3 and $ZnIn_2S_4$ are depicted in Figure 3.9. The separated nanoplates of the microflower structures are seen on TEM images in Figure 3.9 (a) and (c). Figure 3.9 (b) and (d) exhibit the interplanar spacings of 3.11 Å and 3.06 Å, which correspond to the (206) of In_2S_3 and (222) of $ZnIn_2S_4$ lattice spacings, respectively.

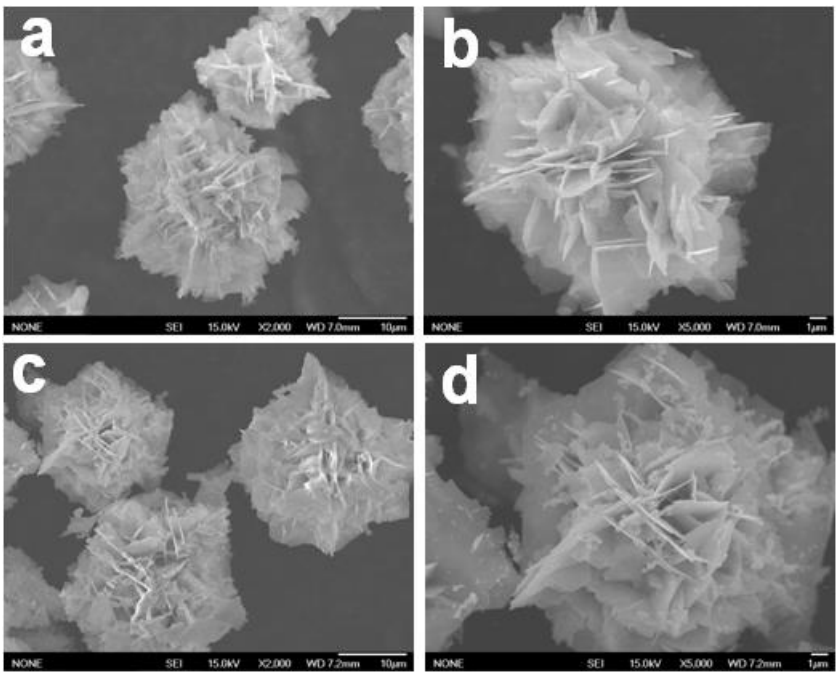

Figure 3.8 SEM images of as-synthesized (a), (b) In_2S_3, and (c), (d) $ZnIn_2S_4$ at different magnifications.

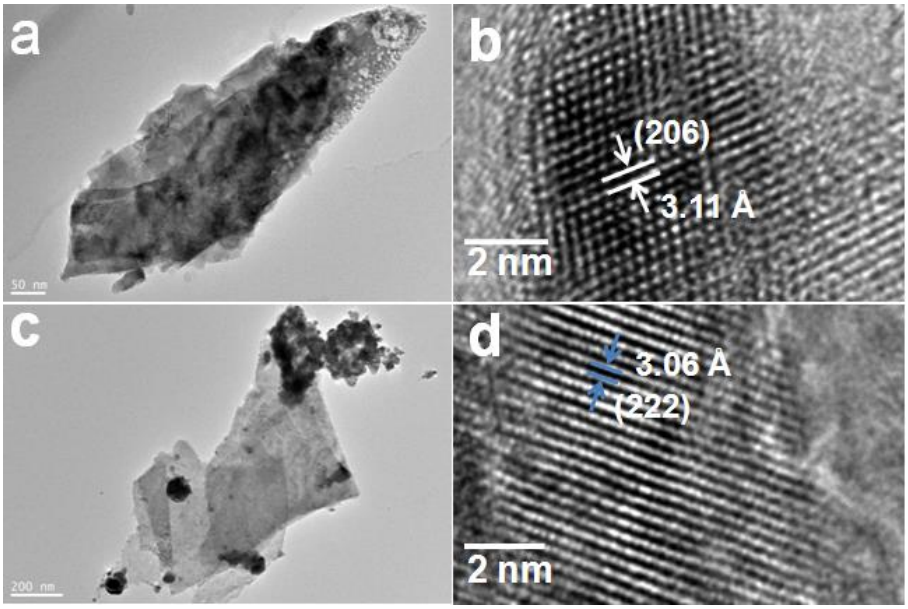

Figure 3.9 TEM images of (a) In_2S_3 and (c) $ZnIn_2S_4$; and HRTEM images of (b) In_2S_3 and (d) $ZnIn_2S_4$.

Figure 3.10 shows the XRD patterns of the $In_2S_3/ZnIn_2S_4$ bulk composites. The intensity of $ZnIn_2S_4$ peaks increases with increasing the amount of $ZnCl_2$ as shown in the enlarged XRD patterns. When 0.8 mmol of $ZnCl_2$ and 1.2 mmol of $MgCl_2 \cdot 6H_2O$ were added into the reaction solution, the peaks of In_2S_3 disappeared. Based on the XRD results, the mass percentage of $ZnIn_2S_4$ and In_2S_3 were calculated and shown in Figure 3.11.

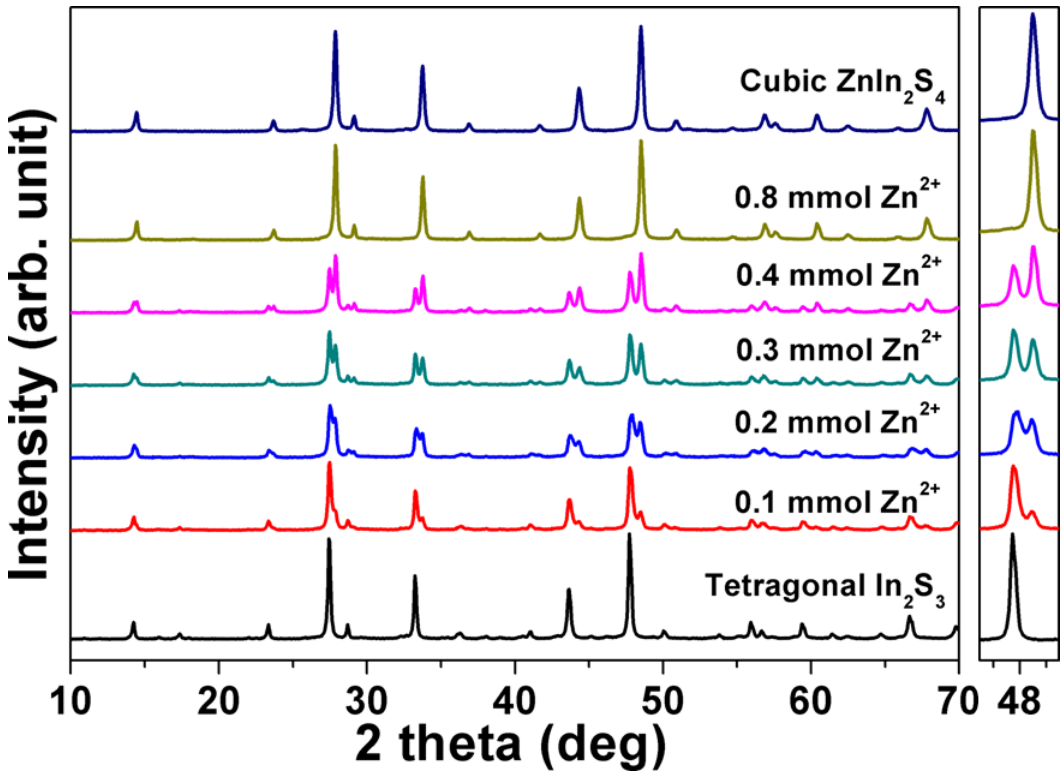

Figure 3.10 XRD patterns of tetragonal In_2S_3 and cubic $ZnIn_2S_4$ phases and an $In_2S_3/ZnIn_2S_4$ bulk composite synthesized from different amount of $ZnCl_2$ (presented as Zn^{2+}) and $MgCl_2 \cdot 6H_2O$ (not shown).

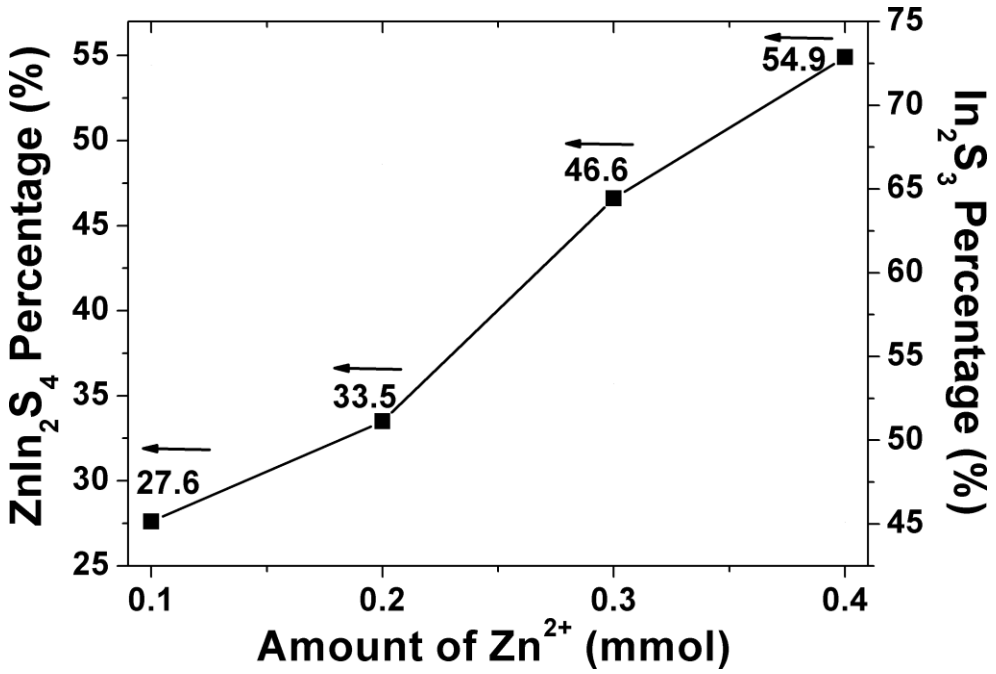

Figure 3.11 The mass percentage of $ZnIn_2S_4$ and In_2S_3 in the bulk composite.

Figure 3.12 shows the typical SEM, TEM, and HRTEM images of the $In_2S_3/ZnIn_2S_4$ bulk composite using 0.3 mmol of $ZnCl_2$, 1.7 mmol of $MgCl_2 \cdot 6H_2O$, and 1 mmol of $NaInS_2$ as the reagents. The bulk composite keeps the similar morphology as the precursor (Figure 3.12 (a) and (b)). As observed in Figure 3.12 (c), the microflowers are constructed from nanoplates. Figure 3.12 (d) depicts the HRTEM image of an $In_2S_3/ZnIn_2S_4$ bulk composite. The interplanar spacing is 3.74 Å which is corresponding with the lattice spacing of {220} of cubic $ZnIn_2S_4$. The inset in Figure 3.12 (d) clearly reveals that there are two sets of SAED patterns. The calculated intersection angles between (220) and (202), and between (202) and $(0\bar{2}2)$ are both 60°. Furthermore, the calculated lattice spacings of (220), (202), and $(0\bar{2}2)$ are 3.74 Å. The two results reveal that these three planes belong to the cubic $ZnIn_2S_4$, which is also consistent with the HRTEM result in Figure 3.12 (d). On the other hand, the calculated intersection angles between (214) and $(1\bar{1}8)$, and between $(1\bar{1}8)$ and $(\bar{1}\bar{2}4)$ are 60.95°. The calculated interplanar spacings of (214), $(\bar{1}\bar{2}4)$, and $(1\bar{1}8)$ are 3.14 Å, 3.14 Å, and 3.24 Å, respectively. These results confirm that the three planes (214), $(\bar{1}\bar{2}4)$, and $(1\bar{1}8)$ belong to the tetragonal In_2S_3. Therefore, it can be concluded that $In_2S_3/ZnIn_2S_4$ bulk composite has been successfully synthesized, though the lattice image of the tetragonal In_2S_3 wasn't observed in the nanoplate in Figure 3.12 (c). The further characterization of other nanoplates by TEM, HRTEM, and SAED confirmed the existence of tetragonal In_2S_3 as shown in Figure 3.13. These HRTEM and SAED results were the characterizations of red-rectangle-marked region in Figure 3.13 (a). The calculated intersection angles of α (between (117) and (1 0 10)) and β (between (1 0 10) and $(0\bar{1}3)$) are 28.5° and 57.9°, respectively. These results reveal that the planes (117), (1 0 10), and $(0\bar{1}3)$ belong to the tetragonal In_2S_3, which are consistent with the HRTEM result in Figure 3.13 (b). The lattice spacing of 6.23 Å is the value of {103} of the

tetragonal In_2S_3.

In order to confirm the fluent interface between In_2S_3 and $ZnIn_2S_4$ in the bulk composite, the interface was characterized by HRTEM as shown in Figure 3.14. The left part is In_2S_3, and the right part is $ZnIn_2S_4$. It can be seen that the interface is smooth.

The comparison of the SEM images of all the bulk composites synthesized from different amount of $ZnCl_2$ and $MgCl_2{\cdot}6H_2O$ is shown in Figure 3.15. These composites exhibit the similar microflower morphology.

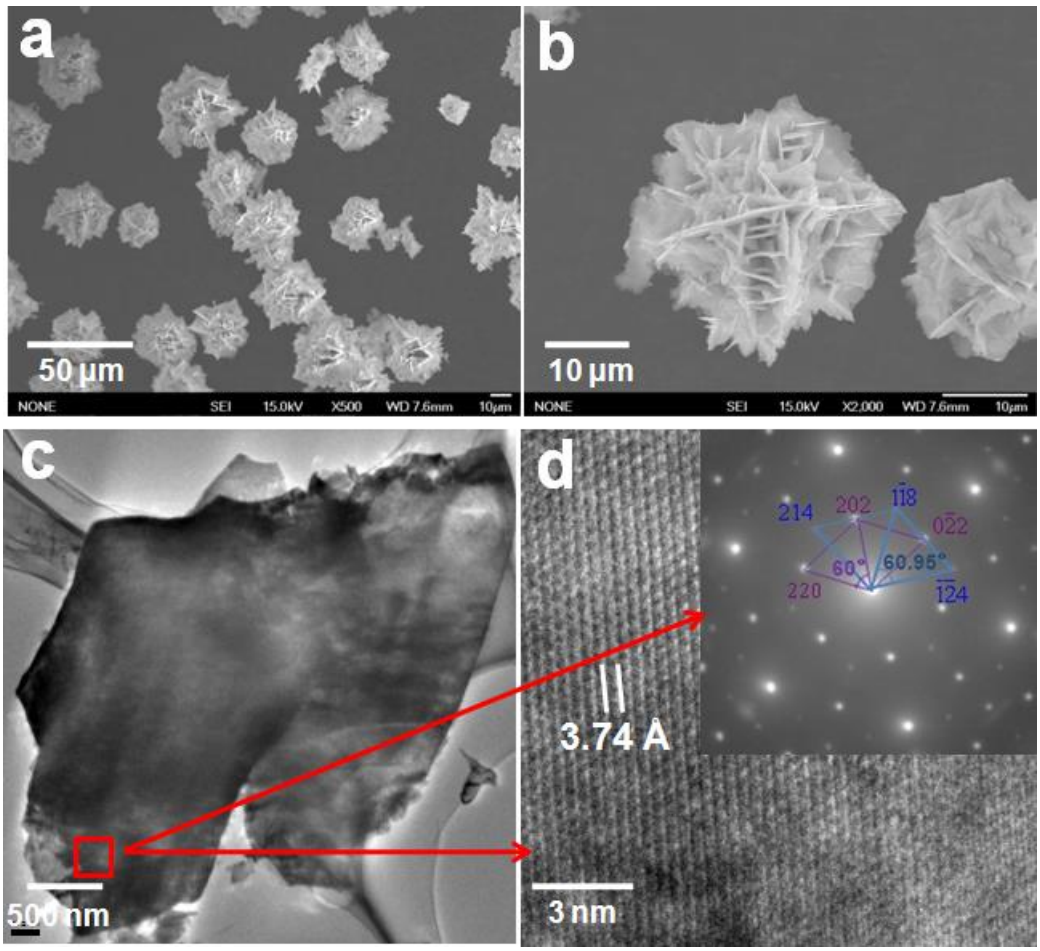

Figure 3.12 (a), (b) SEM images, (c) TEM image and (d) HRTEM image (inset: SAED pattern) of an $In_2S_3/ZnIn_2S_4$ bulk composite synthesized using 0.3 mmol of $ZnCl_2$, 1.7 mmol of $MgCl_2{\cdot}6H_2O$, and 1mmol of $NaInS_2$ as the reagents at 200 °C for 24 h.

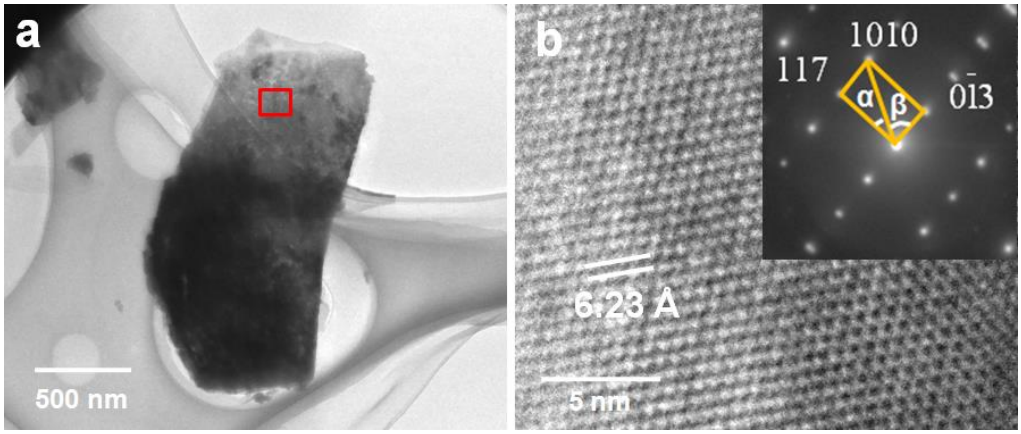

Figure 3.13 (a) TEM image and (b) HRTEM image (inset: SAED patterns) of an $In_2S_3/ZnIn_2S_4$ bulk composite synthesized using 0.3 mmol of $ZnCl_2$, 1.7 mmol of $MgCl_2 \cdot 6H_2O$, and 1mmol of $NaInS_2$ as the reagents at 200 °C for 24 h.

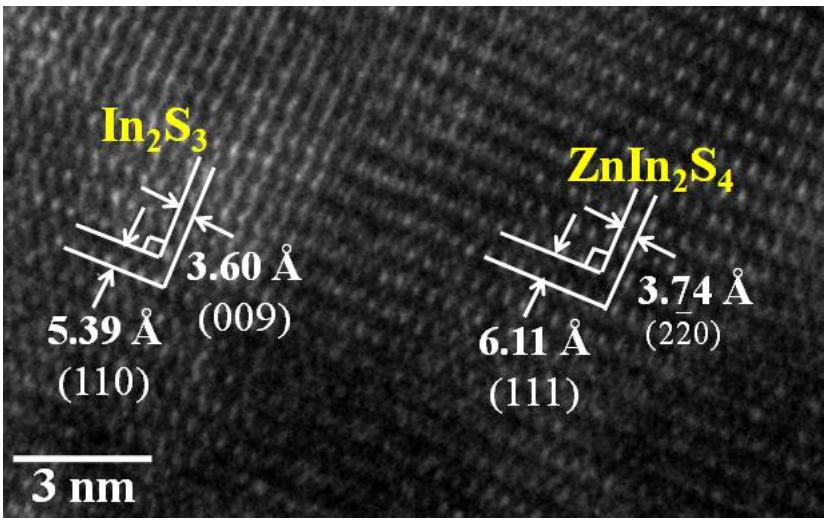

Figure 3.14 HRTEM image of an $In_2S_3/ZnIn_2S_4$ bulk composite synthesized using 0.3 mmol of $ZnCl_2$, 1.7 mmol of $MgCl_2 \cdot 6H_2O$, and 1mmol of $NaInS_2$ as the reagents at 200 °C for 24 h.

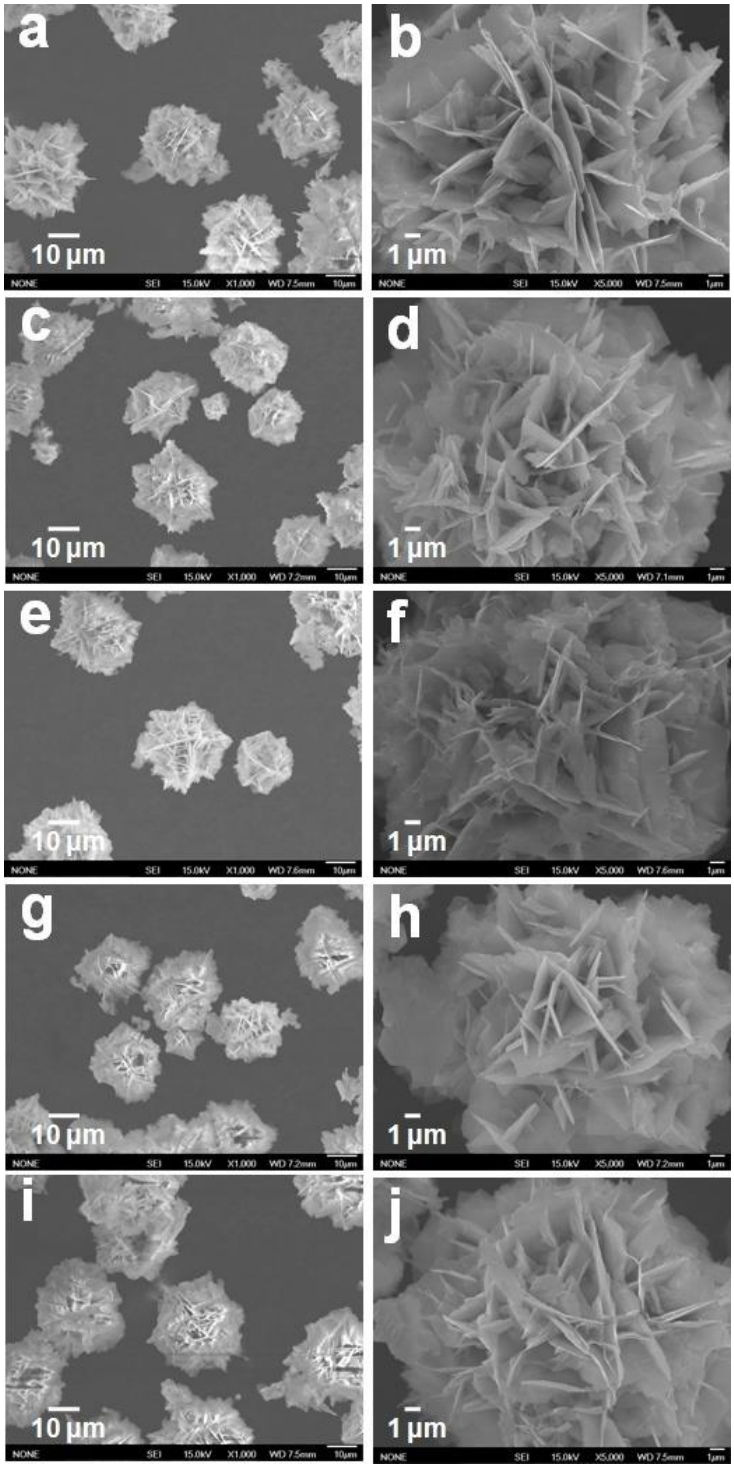

Figure 3.15 SEM images at different magnifications of $In_2S_3/ZnIn_2S_4$ bulk composite synthesized from different amount of $ZnCl_2$ (presented as Zn^{2+}) and $MgCl_2 \cdot 6H_2O$ (not shown): (a), (b) 0.1 mmol; (c),(d) 0.2 mmol; (e), (f) 0.3 mmol; (g), (h) 0.4 mmol; (i), (j) 0.8 mmol.

To evaluate the extent of elemental distribution, the STEM elemental mapping of S, Zn, and In species was performed for the composite as shown in Figure 3.16. It can be seen that S and In elements are homogeneously distributed in all samples while Zn element is non-uniform, which is close to the noise intensity in the marked framed region (in red) in Figure 3.16 (d). On the other hand, there are clear Zn signals in the framed area (purple) in Figure 3.16 (d). Taking into consideration of the fact that two phases, In_2S_3 and $ZnIn_2S_4$, are in the same sample as was shown in Figure 3.10 when appropriate $ZnCl_2$ and $MgCl_2{\cdot}6H_2O$ amounts were added into the reaction system together, the products are In_2S_3 and $ZnIn_2S_4$ in the marked regions as shown in Figure 3.16 (c), respectively. Furthermore, it is reasonable to suggest that In_2S_3 and $ZnIn_2S_4$ phases are evenly distributed, because Zn^{2+} and Mg^{2+} were homogeneous in the solution and simultaneously exchanged Na^+ of the $NaInS_2$ precursor during the reaction process.

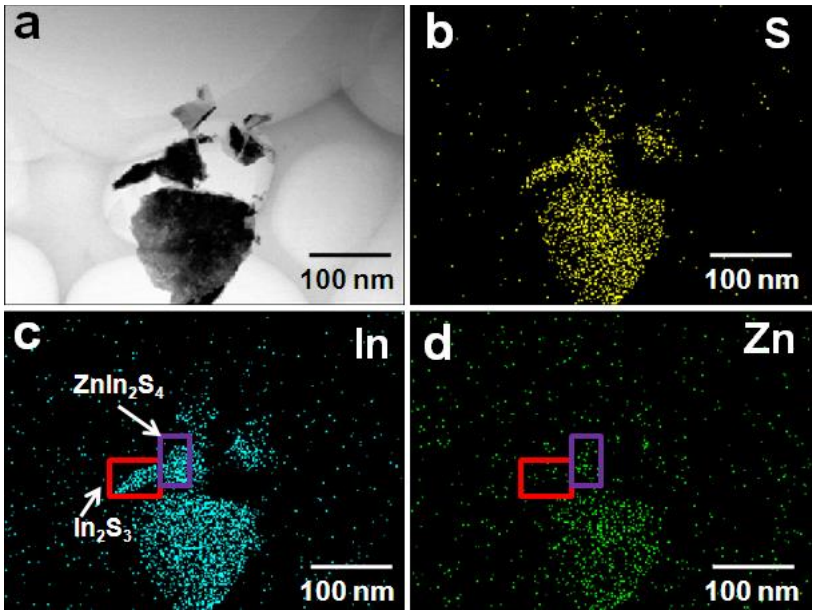

Figure 3.16 (a) STEM image and STEM elemental mapping for (b) S element, (c) In element, and (d) Zn within an $In_2S_3/ZnIn_2S_4$ bulk composite synthesized by using 0.3 mmol of $ZnCl_2$, 1.7 mmol of $MgCl_2{\cdot}6H_2O$, and 1mmol of $NaInS_2$ as the reagents at 200 °C for 24 h.

3.3.2 Optical properties

The unitized UV-vis absorption spectra of $In_2S_3/ZnIn_2S_4$ bulk composites are shown in Figure 3.17 (a). The absorption edges display a gradual blue-shift with increasing the amount of $ZnCl_2$ in the reagents because the band gap of $ZnIn_2S_4$ is wider than that of In_2S_3 according to the subsequent calculations. Their band gaps were calculated in line with of $\alpha h\nu = A(h\nu - E_g)^{n/2}$, in which α, ν, A, and E_g signify the absorption coefficient, light frequency, proportionality constant, and band gap, respectively, and n equals 1 or 4 depending on whether the band gap is direct or indirect. Here $n = 1$ because both In_2S_3 and $ZnIn_2S_4$ phases are direct band gap semiconductors [31, 32]. The calculated values of band gap of In_2S_3 and $ZnIn_2S_4$ are shown in Figure 3.17 (b). It is 2.12 eV for In_2S_3, which is consistent with the reported range of 2.0-2.2 eV [20]; and the band gap is 2.46 eV for $ZnIn_2S_4$, this value is in agreement with the range of 2.2-2.8 eV due to the different phases, morphologies, particle size, and fabrication method of this compound [33].

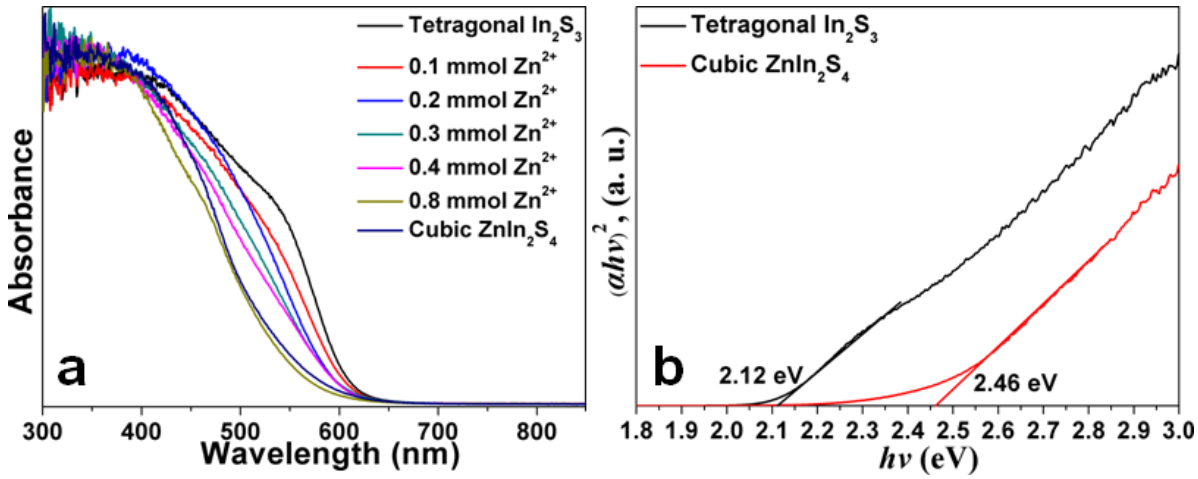

Figure 3.17 (a) UV-vis absorption spectra of an $In_2S_3/ZnIn_2S_4$ bulk composite synthesized by using different amount of $ZnCl_2$ and $MgCl_2 \cdot 6H_2O$ at 200°C for 24 h, and (b) Plots of $(\alpha h\nu)^2$ against photon energy ($h\nu$).

3.3.3 Photocatalytic activity

The photocatalytic evaluation for H_2 evolution of the as-synthesized tetragonal In_2S_3 and cubic $ZnIn_2S_4$ phases, and $In_2S_3/ZnIn_2S_4$ bulk composites was under visible-light irradiation ($\lambda > 400$ nm) in 280 ml of Na_2S (0.35 mol/L)/K_2SO_3 (0.25 mol/L) aqueous solution. This procedure was performed in a pyrex cell (430 ml in volume) connected with the closed gas-circulation system, and the temperature of the aqueous solution containing the photocatalyst and sacrificial reagents was about 60 °C. The light source was a Xe lamp (300 W) with a cut filter (L42). The amount of photocatalyst was 0.1 g loaded with 1wt% of Pt as the cocatalyst using photodeposition under visible light irradiation for 2 h. It took 5 h for the H_2 evaluation under visible-light irradiation after loading the cocatalyst, the time course of photocatalytic H_2 evolution is shown in Figure 3.18.

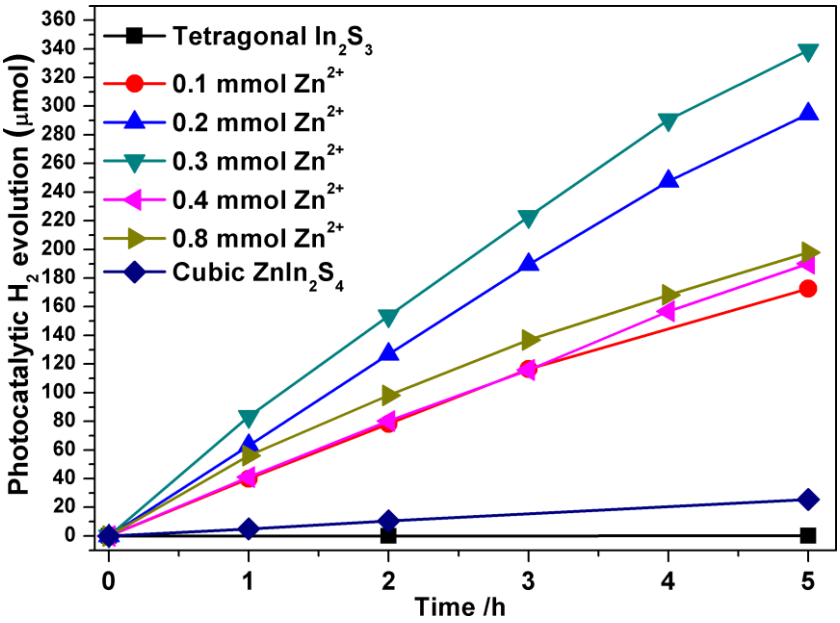

Figure 3.18 Time course of photocatalytic H_2 evolution of individual In_2S_3 and $ZnIn_2S_4$ phases, and an $In_2S_3/ZnIn_2S_4$ bulk composite synthesized from different amounts of $ZnCl_2$ (presented in the picture; mmol) and $MgCl_2 \cdot 6H_2O$ (not shown) as reagents at 200 °C for 24 h.

The photocatalytic H_2 evolution rate of the samples in Figure 3.18 is shown in Figure 3.19 (a). The H_2 evolution rate of tetragonal In_2S_3 is negligible due to its poor separation ability of the photoexcited electrons and holes, which resulted from the ordered indium defects in it [24]. The photocatalytic activity of an individual $ZnIn_2S_4$ phase is also low (about 5.1 μmol/h), probably due to the lower photocatalytic activity of the cubic phase compared to the hexagonal phase, the vacancies and defects in which enhance the recombination probability of carriers [34]. However, the photocatalytic H_2 evolution rate was highly enhanced for the composite in comparison with individual constituting phases. The highest H_2 evolution rate was about 67.8 μmol/h when 0.3 mmol of $ZnCl_2$, 1.7 mmol of $MgCl_2{\cdot}6H_2O$, and 1mmol of $NaInS_2$ were used as reagents which reacted at 200 °C for 24 h. The apparent quantum efficiency (AQE) was about 1.4%.

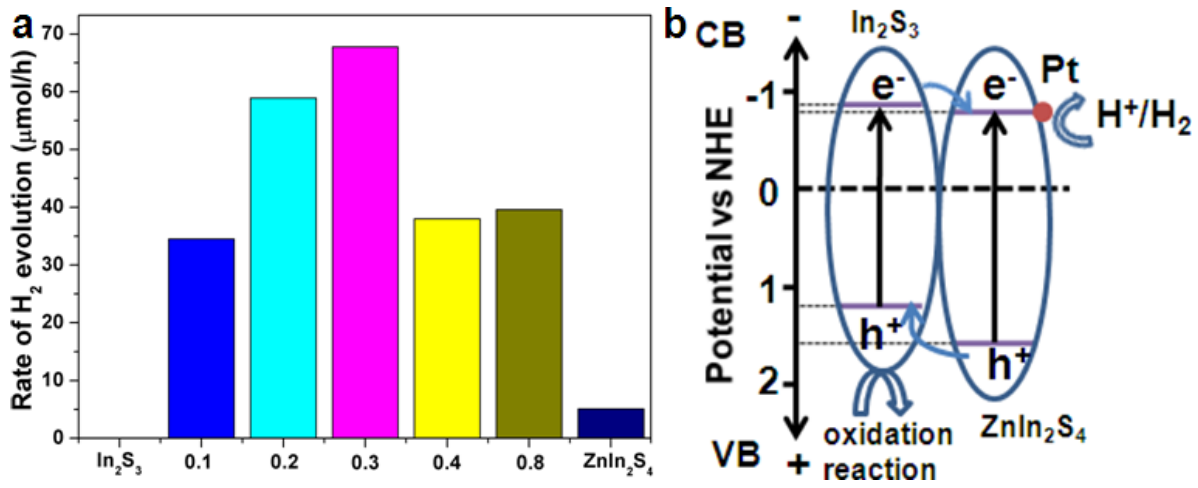

Figure 3.19 (a) Photocatalytic H_2 evolution rate of individual In_2S_3, and $ZnIn_2S_4$ phases and an $In_2S_3/ZnIn_2S_4$ bulk composite synthesized from different amounts of $ZnCl_2$ (presented in the picture; mmol) and $MgCl_2{\cdot}6H_2O$ (not shown) as reagents at 200 °C for 24 h. Photocatalyst: 0.1 g; Light source: 300 W of Xe lamp with a L42 cut filter. (b) Schematic diagram for the photoexcited electrons and holes separation at the interface of the composite.

This enhanced photoactivity is attributed to the efficient separation ability for the photo-generated electrons and holes for the composite. The conduction band edges of In_2S_3 and $ZnIn_2S_4$ at the zero charge (pH_{zpc}) can be evaluated by the following equation [35]:

$$E_{CB}^{0} = X - E^{C} - {}^{1}/_{2}\, E_g$$

where X is the absolute electronegativity of the semiconductor, which shows the geometric mean of the absolute electronegativity of the constituent atoms, and it is defined as the arithmetic mean of the atomic electron affinity and the first ionization energy; E^c is the energy of free electrons on the hydrogen scale (~4.5 eV); and E_g is the band gap of a semiconductor. The calculated values of X are 4.704 eV and 4.894 eV for In_2S_3 and $ZnIn_2S_4$, respectively. According to the above equation and the estimated band gaps, the conduction band edges of In_2S_3 (E_g = 2.12 eV) and $ZnIn_2S_4$ (E_g = 2.46 eV) are -0.856 eV and -0.836 eV, respectively. Accordingly, the valence band edges are 1.264 eV for In_2S_3 and 1.624 eV for $ZnIn_2S_4$. As a result, the photoexcited electrons transfer from the conduction band of In_2S_3 to that of $ZnIn_2S_4$, where the reduction of H^+ occurs; simultaneously, the photoexcited holes in $ZnIn_2S_4$ transfer from its valence band to that of In_2S_3, where the oxidation of sacrificial reagents occurs as shown in Figure 3.19 (b). This process greatly enhanced the separation ability of the photoexcited electrons and holes, which accordingly improved the photocatalytic efficiency.

Furthermore, the photocatalytic evaluation was carried out in the aqueous solution containing S^{2-} and SO_3^{2-}. In this reactant solution, the photocatalytic reaction is supposed to proceed along the following processes [28]:

$$Photocatalyst + h\nu \rightarrow e^{-}(CB) + h^{+}(VB) \qquad (1)$$

$$2H_2O + 2e^{-}(CB) \rightarrow H_2 + 2OH^{-} \qquad (2)$$

$$SO_3^{2-} + H_2O + 2h^{+}(VB) \rightarrow SO_4^{2-} + 2H^{+} \qquad (3)$$

$$2S^{2-} + 2h^{+}(VB) \rightarrow S_2^{2-} \qquad (4)$$

$$S_2^{2-} + SO_3^{2-} \rightarrow S_2O_3^{2-} + S^{2-} \quad (5)$$

$$SO_3^{2-} + S^{2-} + 2h^+(VB) \rightarrow S_2O_3^{2-} \quad (6)$$

In this work, H_2O was reduced into H_2 at active sites by the photoexcited electrons on the Pt cocatalyst locating on the surface of $ZnIn_2S_4$. The photoexcited holes in the valence band of In_2S_3 oxidized SO_3^{2-} and S^{2-} to produce SO_4^{2-} and S_2^{2-} as shown in equations (3) and (4), respectively. The production of S_2^{2-} ions acting as an optical filter was effectively suppressed by the reaction in equation (5) and (6), the $S_2O_3^{2-}$ ions are transparent to light. The excessive S^{2-} ions in the reaction system protected the photocatalyst by suppressing the sulphur defects in the surface of the photocatalyst.

3.4 Conclusions

(I) Hierarchical $NaInS_2$ microflowers were synthesized by a solvothermal route at 180 °C for 12 h. The microflowers consisted of nanoplates with ca. 100 nm in thickness. Then, $In_2S_3/ZnIn_2S_4$ bulk composites were successfully synthesized by an ion-exchange method at 200 °C for 24 h by adding $ZnCl_2$ and $MgCl_2·6H_2O$ as the ion-exchange reagents and using $NaInS_2$ as the homogeneous precursor. The $In_2S_3/ZnIn_2S_4$ bulk composites kept the morphology of the $NaInS_2$ precursor.

(II) The photocatalytic activities of the $In_2S_3/ZnIn_2S_4$ bulk composites for H_2 evolution under visible-light irradiation were highly enhanced compared with the individual In_2S_3 and $ZnIn_2S_4$. The enhancement of photocatalytic activity resulted from the improved separation ability of the photogenerated electrons and holes. Because of the difference of energy levels in the valence and conduction bands of In_2S_3 and $ZnIn_2S_4$, the photoexcited electrons transferred from the conduction band of In_2S_3 to the conduction band of $ZnIn_2S_4$, and simultaneously the photoexcited holes transferred from the valence band of $ZnIn_2S_4$ to that of In_2S_3. This process greatly enhanced the separation ability of the photoexcited charges. The $In_2S_3/ZnIn_2S_4$ bulk composite fabricated from 0.3 mmol of $ZnCl_2$, 1.7 mmol of $MgCl_2·6H_2O$, and 1 mmol $NaInS_2$ as the starting reagents. The apparent quantum efficiency was 1.4% at 420 nm.

(III) The fluent interface of $In_2S_3/ZnIn_2S_4$and mass percentage must play significant roles in the separation of photoexcited carriers. This homogeneous-precursor ion-exchange route provides a novel approach for the synthesis of bulk composites showing good electrical contact and evenly distributed components. It is a good example of the improvement of

photocatalytic activity through a structural design, and thus can be used to synthesize other functional high-performance composites.

References

[1] Tong H, Ouyang S X, Bi Y P, Umezawa N, Oshikiri M and Ye J H 2012 *Adv. Mater.* **24** 229.

[2] Zhang Z B, Wang C C, Zakaria R and Ying J Y 1998 *J. Phys. Chem. B* **102** 10871.

[3] Lü X J, Huang F Q, Mou X L, Wang Y M and Xu F F 2010 *Adv. Mater.* **22** 3719.

[4] Lv J, Kako T, Zou Z G and Ye J H 2009 *Appl. Phys. Lett.* **95** 032107.

[5] Su J, Zou X X, Li G D, Wei X, Yan C, Wang Y N, Zhao J, Zhou L J and Chen J S 2011 *J. Phys. Chem. C* **115** 8064.

[6] Lin X P, Xing J C, Wang W D, Shan Z C, Xu F F and Huang F Q 2007 *J. Phys. Chem. C* **111** 18288.

[7] Kim H G, Borse P H, Choi W Y and Lee J S 2005 *Angew. Chem. Int. Ed.* **44** 4585.

[8] Tada H, Mitsui T, Kiyonaga T, Nkita T and Tanaka K 2006 *Nat. Mater.* **5** 782.

[9] Long M, Cai W M, Cai J, Zhou B X, Chai X Y and Wu Y H 2006 *J. Phys. Chem. B* **110** 20211.

[10] Ng J W, Xu S P, Zhang X W, Yang H Y and Sun D D 2010 *Adv. Funct. Mater.* **20** 4287.

[11] Liu Z F, Zhao Z G and Miyauchi M 2009 *J. Phys. Chem. C* **113** 17132.

[12] Wilson A, Mishra S R, Gupta R and Ghosh K 2012 *J. Magn. Magn. Mater.* **324** 2597.

[13] Kim H G, Borse P H, Jang J S, Jeong E D, Jung O S, Suh Y J and Lee J S 2009 *Chem. Commun.* **39** 5889.

[14] Tsuji I, Kato H, Kobayashi H and Kudo A 2004 *J. Am. Chem. Soc.* **126** 13406.

[15] Tsuji I, Kato H and Kudo A 2005 *Angew. Chem. Int. Ed.* **44** 3565.

[16] Yan H J, Yang J H, Ma G J, Wu G P, Zong X, Lei Z B, Shi J Y and Li C 2009 *J. Catal.* **266** 165.

[17] Zhang W, Wang Y B, Wang Z, Zhong Z Y and Xu R 2010 *Chem. Commun.* **46** 7631.

[18] Zong X, Yan H J, Wu G P, Ma G J, Wen F Y, Wang L and Li C 2008 *J. Am. Chem. Soc.*

130 7176.

[19] Zhang F X, Yamakata A, Maeda K, Moriya Y, Takata T, Kubota J, Teshima K, Oishi S and Domen K 2012 *J. Am. Chem. Soc.* **134** 8348.

[20] Qiu W M, Xu M S, Yang X, Chen F, Nan Y X, Zhang J L, Iwai H and Chen H Z 2011 *J. Mater. Chem.* **21** 13327.

[21] He Y H, Li D Z, Xiao G C, Chen Y B, Sun M, Huang H J and Fu X Z 2009 *J. Phys. Chem. C* **113** 5254.

[22] Rengaraj S, Venkataraj S, Tai C W, Kim Y H, Repo E and Sillanpää M 2011 *Langmuir* **27** 5534.

[23] Cingarapu S, Ikenberry M A, Hamal D B, Sorensen C M, Hohn K and Klabunde K J 2012 *Langmuir* **28** 3569.

[24] Fu X L, Wang X X, Chen Z X, Zhang Z Z, Li Z H, Leung D Y C, Wu L and Fu X Z 2010 *Appl. Catal. B: Environ.* **95** 393.

[25] Chai B, Peng T Y, Zeng P and Mao J 2011 *J. Mater. Chem.* **21** 14587.

[26] Li Y X, Chen G, Zhou C and Sun J X 2009 *Chem. Commun.* **15** 2020.

[27] Li Y X, Chen G, Wang Q, Wang X, Zhou A K and Shen Z Y 2010 *Adv. Funct. Mater.* **20** 3390.

[28] Xu Z D, Li Y X, Peng S Q, Lu G X and Li S B 2011 *CrystEngComm* **13** 4770.

[29] Cheng H F, Huang B B, Liu Y Y, Wang Z Y, Qin X Y, Zhang X Y and Dai Y 2012 *Chem. Commun.* **48** 9729.

[30] Cheng H F, Huang B B, Qin X Y, Zhang X Y and Dai Y 2012 *Chem. Commun.* **48** 97.

[31] Ho C H 2011 *J. Mater. Chem.* **21** 10518.

[32] Yu H T, Quan X, Zhang Y B, Ma N, Chen S and Zhao H M 2008 *Langmuir* **24** 7599.

[33] Chen Y J, Hu S W, Liu W J, Chen X Y, Wu L, Wang X X, Liu P and Li Z H 2011 *Dalton Trans.* **40** 2607.

[34] Chai B, Peng T Y, Zeng P, Zhang X H and Liu X J 2011 *J. Phys. Chem. C* **115** 6149.

[35] Xu Y and Schoonen M A A 2000 *Am. Mineral.* **85** 543.

[36] Tsuji I, Shimodaira Y, Kato H, Kobayashi H and Kudo A 2010 *Chem. Mater.* **22** 1402.

Chapter 4 $Zn_{1-x}Cu_xS$ for Photocatalytic Water Splitting

4.1 Introduction

As mentioned in the above chapters, development of clean and renewable energy is an urgent task for researchers because of the decreasing fossil fuels and the increasing environmental problems. Photocatalytic water splitting for H_2 evolution attracts plenty of research interest in recent years. For photocatalytic water splitting, one bottleneck is the separation and migration ability of the photoexcited e^-/h^+ pairs [1, 2]. Ultrafine particle of photocatalyst facilitates the charge separation and migration due to the shorter transfer distance, quantum confinement effects, and more trapping sites to counteract charge recombination [3-6]. Yu *et al.* studied the charge transfer process between MO molecules and bulk TiO_2 films and nano-sized TiO_2 using time-correlated single-photon counting (TCSPC) and nanosecond and femtosecond transient absorption spectroscopies. The recombination of electrons and holes in the bulk TiO_2 film was 1000 times faster than that in nano-sized TiO_2 particles. They explained the reason as that bulk TiO_2 film becoming a developed crystal had fewer trapping sites to hinder the electrons and holes recombination [3]. Furthermore, ultrafine particle size means large surface-area-to-volume ratio, so that it can provide more active sites for surface redox reactions [2, 4, 7-9], which is beneficial to enhance the photocatalytic activity.

Although the photocatalysts containing indium are efficient for photocatalytic reactions, ZnS with more negative bottom of conduction band is more beneficial for photocatalytic H_2 evolution than Zn/In-based oxides and sulfides. On the other hand, the indium element is rare on the earth. It is not beneficial to the wide-range application of photocatalysts. Zinc sulfide (ZnS) exhibits wide band gaps of 3.72 eV and 3.77 eV for the cubic zinc blende structure and

hexagonal wurtzite structure, respectively [10]. Due to the rapid generation of photoexcited e^-/h^+ pairs and highly negative potentials of excited electrons, ZnS can achieve photocatalytic H_2 evolution even without any noble metal as the cocatalyst [11-14]. However, the wide band gap limits its practical application in respect that it is only active under UV-light. Many efforts have been carried out to sensitize ZnS to visible light. One favorable attempt is 3*d*-transition metal ions doping (i.e., Ni^{2+} and Cu^{2+}) [15-17]. Intensive efforts have also been devoted to fabricate the solid solutions based on ZnS, such as $Zn_xCd_{1-x}S$, $(AgIn)_xZn_{2(1-x)}S$, ZnS-$CuInS_2$-$AgInS_2$, and ZnS-In_2S_3-CuS [18-21]. And coupling other semiconductors with narrow band gaps to harvest visible light has been verified to be a feasible approach [22, 23]. Unfortunately, among these photocatalysts and synthetic methods, cadmium ion is poisonous to human beings and environment, and indium is rare element on the earth; additionally, high temperature treatment usually is necessary to synthesize solid solution with high crystallinity, which inevitably increases the particle size and thus weakens the photocatalytic activity. There is no doubt that rich-element-based, environmental friendly, and visible-light-sensitive photocatalysts with excellent photocatalytic activity are necessary to make photocatalysis practical. $Zn_{1-x}Cu_xS$ exhibits great potential for practical application according to the discussion above, and it was usually prepared by a facile coprecipitation method [24, 25]. However, controllable synthesis of ultrafine $Zn_{1-x}Cu_xS$ is still a challenge. The ZnS is much easier to dissolve in water than CuS due to the greatly different solubility products (K_{sp}(ZnS) = 1.6×10^{-24}, K_{sp}(CuS) = 6.3×10^{-36}) [12]. This difference results in that CuS shows much faster precipitation rate than ZnS in aqueous solution, it is apparently hard to fabricate $Zn_{1-x}Cu_xS$ with well dispersion of Cu element in the whole host material. Therefore, the key of fabrication of high quality $Zn_{1-x}Cu_xS$ is to achieve a balance of the precipitation rate between ZnS and CuS. As we know, complex agent can strongly adjust the reaction rate in a synthesis process [26]. It is obvious that a wet-chemical approach with the assistance of appropriate

complex agent, namely, the complexing-wet-chemical method, is a promising route to control the synthesis of $Zn_{1-x}Cu_xS$.

Thiourea (TU) is an excellent complexing reagent for metal ions, which can balance the reactivity velocity [27, 28]. In this study, visible-light-sensitive ultrathin $Zn_{1-x}Cu_xS$ nanocrystallines with good photocatalytic H_2 evolution activity have been synthesized through the complexing-wet-chemical method with TU as the complexing reagent of Zn^{2+} and Cu^{2+}.

4.2 Experimental section

All the reagents consist of sodium sulfide nonahydrate ($Na_2S·9H_2O$), zinc acetate dihydrate ($(CH_3OO)_2Zn·2H_2O$), thiourea (H_2NCSNH_2), copper (II) acetate monohydrate ($(CH_3COO)_2Cu·H_2O$), and cadmium chloride 2.5-hydrate ($CdCl_2·2.5H_2O$). They were analytical grade and used without further treatment.

4.2.1 Synthesis of $Zn_{1-x}Cu_xS$ by the complexing-wet-chemical method

In a typical procedure, white ZnS deposition was firstly fabricated by adding 100 ml of $Na_2S·9H_2O$ (0.06 mol/L) into 200 ml of $(CH_3OO)_2Zn·2H_2O$ (0.02 mol/L) drop by drop and then the solution was magnetically stirred for 30 min. After that, the white products were washed with distilled water for 5 times and separated by centrifuge, respectively. Secondly, the white ZnS was dispersed into 100 ml of distilled water for 10 min by a ultrasonic method before adding 50 ml of H_2NCSNH_2 (0.4 mol/L) and $(CH_3COO)_2Cu·H_2O$ (0.0032 mol/L) into it. Thirdly, the whole solution was added into a three-neck flask (500 ml) and vigorously stirred at 85 °C for 72 h by a mechanical stirrer at 300 r/min. Finally, the yellow products were cleaned by distilled water and ethanol for several times, respectively. Then the products were dried in air. The other $Zn_{1-x}Cu_xS$ were prepared by the same way just changing the

starting molar ratio of Cu^{2+}/Zn^{2+} (6%, 5%, 3%, and 2%). As reference, $Zn_{1-x}Cu_xS$-I was synthesized by the same way but there was not H_2NCSNH_2 added in the second step, the molar ratio of Cu^{2+}/Zn^{2+} was 4%. $Zn_{1-x}Cu_xS$-II was also synthesized by coprecipitation method as follows. 4 mmol $(CH_3OO)_2Zn\cdot 2H_2O$ and 0.16 mmol $(CH_3COO)_2Cu\cdot H_2O$ was dissolved into 100 ml distilled water, then 50 ml of $Na_2S\cdot 9H_2O$ (0.12 mol/L) was added into that solution drop by drop. After that, the whole solution was vigorously stirred in a three-neck flask at room temperature for 72 h. The products were cleaned by distilled water and ethanol for several times and dried in air for further characterization.

4.2.2 Synthesis of CdS and ZnS

As comparison, CdS was synthesized by the same way mentioned above. At first, 4 mmol of $CdCl_2\cdot 2.5H_2O$ was dissolved into 200 ml of distilled water, then 100 ml of $Na_2S\cdot 9H_2O$ (0.06 mol/L) was added into the solution drop by drop. The final solution was magnetically stirred for 30 min. The synthesized orange CdS were separated and cleaned with distilled water for 5 times by centrifuge. After that, the cleaned CdS was dispersed into 100 ml of distilled water for 10 min by ultrasonic method, then 50 ml of H_2NCSNH_2 (0.4 mol/L) was quickly added into the dispersed CdS solution. Finally, the mixture was transferred into 500 ml of three-neck flask and constantly heated at 85°C for 72 h. The final orange CdS was cleaned by distilled water and ethanol for several times, respectively. Then the products were dried in air for further characterization. ZnS was synthesized by the same way using $Na_2S\cdot 9H_2O$ and $(CH_3OO)_2Zn\cdot 2H_2O$ as the starting materials.

4.3 Characterization

Powder X-ray diffraction (XRD) characterization was performed by using Rint-2000 diffractometer (Rigaku Co., Japan) operating at 40 kV and 30 mA for Cu Kα radiation (λ =

1.5406 Å). Inductively coupled plasma/optical emission spectrometer (ICP/OES) characterization for Zn and Cu elements was operated on IRIS Advantage (Nippon Jarrell-Ash Co., Japan), while the characterization of S element was carried out on Carbon/Sulfur determinator CS-444LS (LECO Co. USA). The BET surface area was measured by nitrogen adsorption at 77 K with a BELSORP II Surface Area Analyzer (Bel Japan Co., Japan). X-ray Photoelectron Spectroscopy (XPS) experiments were performed in type Theta probe using monochromatized Al Kα at hν = 1486.6 eV. The UV-visible diffuse reflection spectra were recorded on a UV-2500PC recording spectrophotometer (Shimadzu Co., Japan). The reflectance spectra were converted into absorption spectra using Kubelka-Munk equation. Transmission electron microscope (TEM) and high-resolution TEM (HRTEM) were operated on JEM-2100F (JEOL).Apparent quantum efficiency (AQE) was calculated by the following equation:

$$AQE(\%) = \frac{\text{The number of reacted electrons}}{\text{The number of incident photons}} \times 100\%$$
$$= \frac{\text{The number of evolved } H_2 \text{ molecules} \times 2}{\text{The number of incident photons}} \times 100\%$$

4.4 Theoretical calculation

The electronic structures of the Cu-doped ZnS were calculated via the plane-wave-pseudopotential approach based on the density functional theory (DFT).The most stable structure was determined via geometry optimization model. Then the electronic structures were calculated using the standard Cambridge serial total energy package (CASTEP) code. The electron-core interaction was showed by ultrasoft pseudopotentials with a plane-wave basis cutoff energy of 310 eV. The electronic exchange-correlation energy was treated within the framework of the local density approximation (LDA). The self-consistent field (SCF)

tolerance was all 1×10^{-6} eV/atom. The FFT grid of basis in the model was 54 × 54 × 54. The *k*-point sets of 2 × 2 × 2 were used for the model.

4.5 Results and discussion

Figure 4.1 shows the crystal structures of the products synthesized by the complexing-wet-chemical method. The peaks of the $Zn_{1-x}Cu_xS$ (starting molar ratio of Cu^{2+}/Zn^{2+} = 2% ~ 6%) don't exhibit obvious shift compared with those of the pure cubic ZnS (JCPDS 065-5476) due to the tiny difference of ionic radius between Zn^{2+} (0.60 Å) and Cu^{2+} (0.57Å).

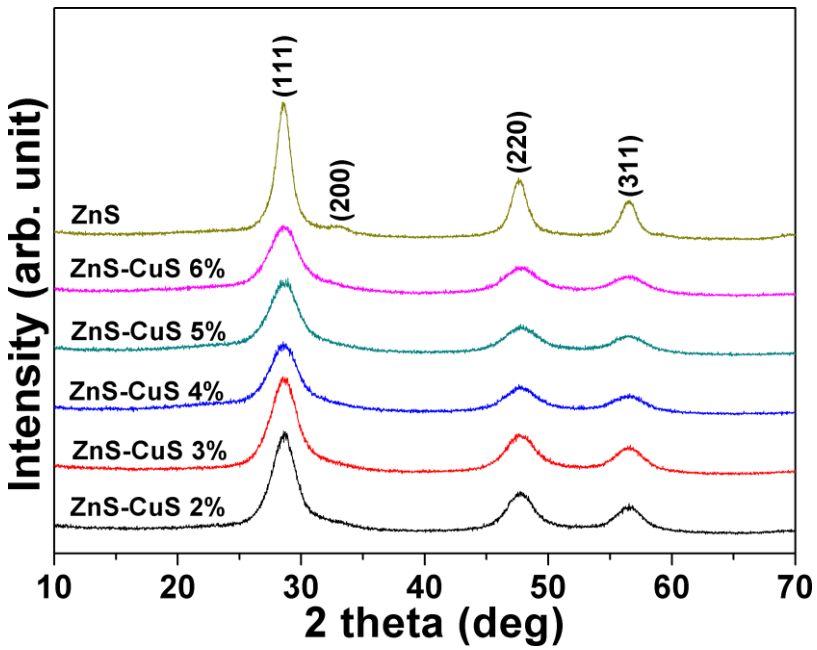

Figure 4.1 XRD patterns of $Zn_{1-x}Cu_xS$ ($0 \leq x \leq 0.066$).

ICP/OES results reveal the actual element molar ratio of Zn/Cu in the as-synthesized $Zn_{1-x}Cu_xS$ (Table 4.1). The calculated molar ratio of Cu/Zn of $Zn_{1-x}Cu_xS$ decreases as the starting molar ratio of Cu^{2+}/Zn^{2+} decreases.

Table 4.1 ICP/OES and Carbon/Sulfur Determinator characterization for Zn, Cu, and S elements.

Starting molar ratio of Cu^{2+}/Zn^{2+}	Element (mass%) Zn	Cu	S	Molar ratio of Zn:Cu:S	Molar ratio of Cu/Zn (x value of $Zn_{1-x}Cu_xS$)
6%	53.3±0.3	3.4±0.1	28.2±0.2	0.927:0.061:1	0.066
5%	55.2±0.1	2.6±0.3	28.9±0.2	0.937:0.051:1	0.054
4%	55.7±0.1	2.8±0.1	28.8±0.2	0.950:0.047:1	0.049
3%	57.1±0.1	1.9±0.1	28.9±0.2	0.969:0.033:1	0.034
2%	57.9±0.1	1.0±0.2	28.8±0.1	0.986:0.018:1	0.018

Figure 4.2 exhibits the representative Transmission Electron Microscope (TEM) and High-resolution TEM (HRTEM) images of $Zn_{0.951}Cu_{0.049}S$. The product consists of many small particles, and the diameter of the ultrafine nanocrystalline is about 5 nm, which is approximate to the value (8.7 nm) calculated by Scherrer-Debye equation.

$$d = \frac{k\lambda}{\beta \cos\theta}$$

Where k is the shape factor, λ is the X-ray wavelength, β is the line broadening at half the maximum intensity (FWHM) in radians, and θ is the Bragg angle; d is the mean size of the crystal. The dimensionless shape factor has a typical value of about 0.9. The interplanar spacing in Figure 4.2 (b) is about 3.1 Å which is corresponding to the value of (111) of cubic ZnS.

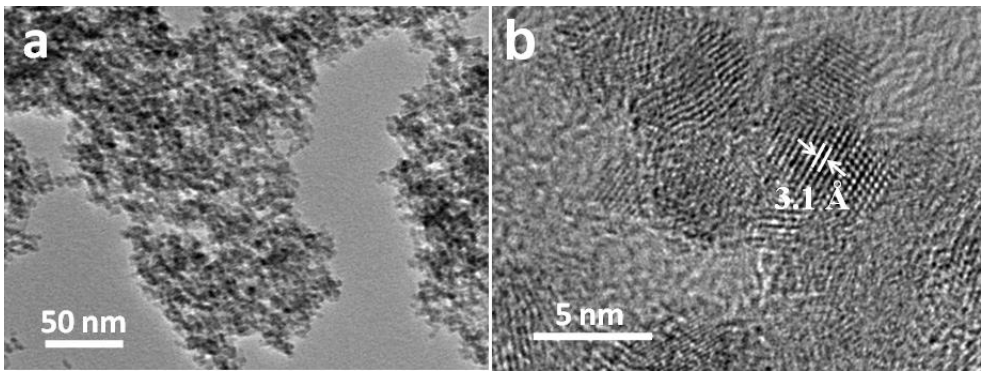

Figure 4.2 Typical (a) TEM image and (b) HRTEM image of $Zn_{0.951}Cu_{0.049}S$.

Figure 4.3 shows the TEM and HRTEM images of the other $Zn_{1-x}Cu_xS$ ($0 \leq x \leq 0.066$) samples, $Zn_{0.934}Cu_{0.066}S$, $Zn_{0.946}Cu_{0.054}S$, $Zn_{0.966}Cu_{0.034}S$, and $Zn_{0.982}Cu_{0.018}S$. All the products are accumulated nanoparticles with ca. 5 nm in diameter.

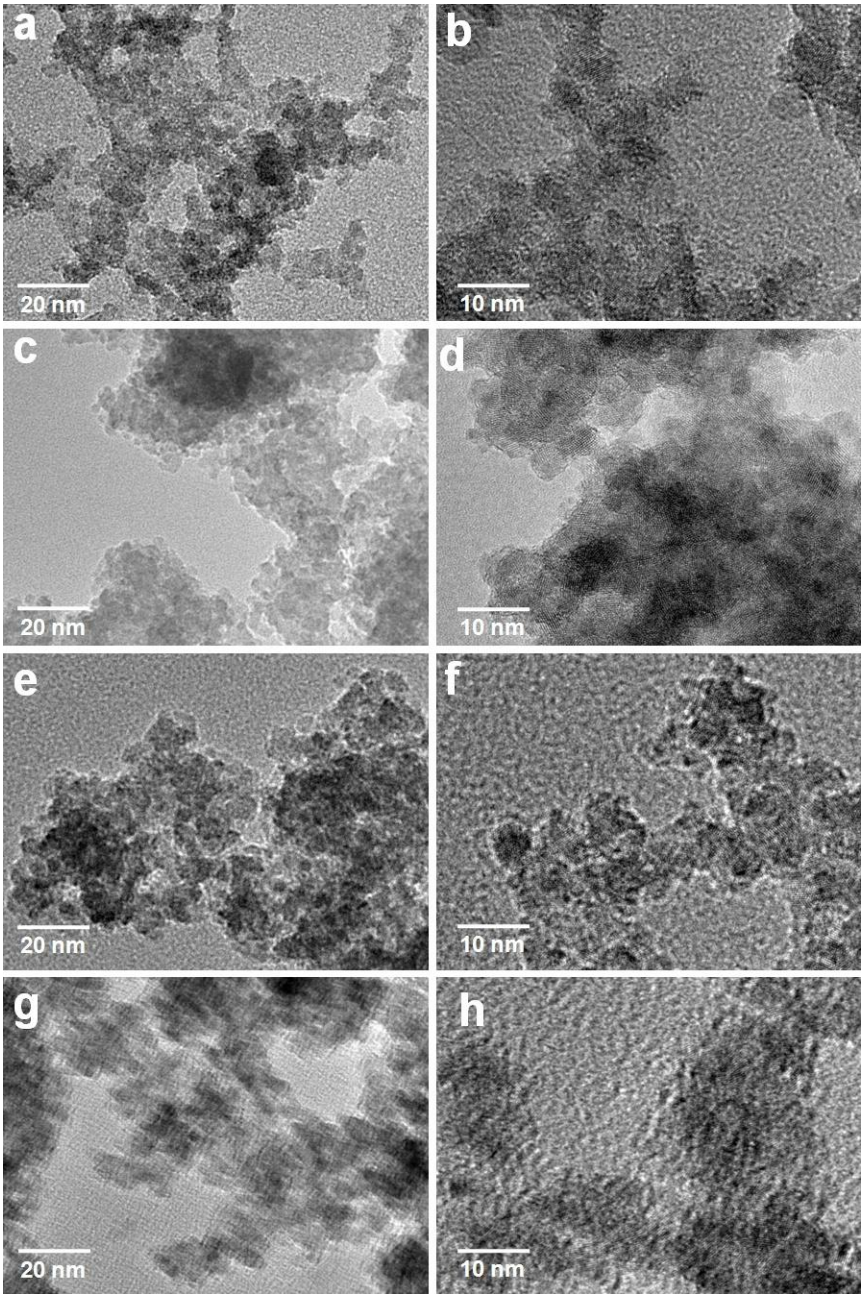

Figure 4.3 Typical TEM images (a), (c), (e), (g) and HRTEM images (b), (d), (f), (h) for $Zn_{0.934}Cu_{0.066}S$, $Zn_{0.946}Cu_{0.054}S$, $Zn_{0.966}Cu_{0.034}S$, and $Zn_{0.982}Cu_{0.018}S$, respectively.

UV-vis absorption spectra of $Zn_{1-x}Cu_xS$are exhibited in Figure 4.4. All the spectra of $Zn_{1-x}Cu_xS$ ($0 \leq x \leq 0.066$) show visible-light absorption and red-shift as increasing the value of *x*, because Cu 3*d* orbitals locate at more negative positions than S 3*p* orbitals and higher percentage of Cu element results in less positive top of valence band [25].

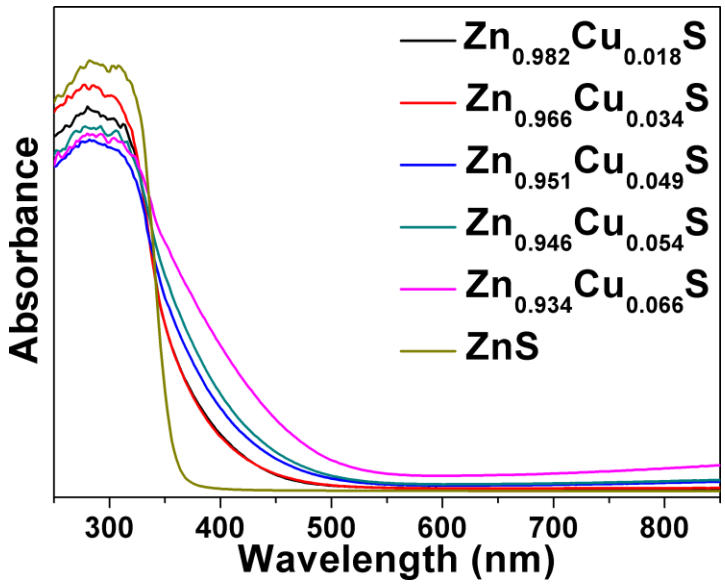

Figure 4.4 UV-vis absorption spectra of $Zn_{1-x}Cu_xS$ ($0 \leq x \leq 0.066$).

In order to confirm the successful dopant of Cu^{2+} into ZnS, we compared the UV-vis absorption spectra of $Zn_{0.951}Cu_{0.049}S$ and the mixture of ZnS and CuS at the mole ratio of 0.951:0.049 as shown in Figure 4.5.For the mixture of ZnS and CuS, the absorption belongs to the ZnS (band edge: ~ 350 nm) and the CuS (600 ~ 850 nm). However, $Zn_{0.951}Cu_{0.049}S$ shows red-shifted absorption band-edge and there is no absorption between 600 nm and 850 nm. Thus, it can be concluded that the Cu^{2+} has been successfully doped into ZnS.

Figure 4.6 shows the density of states for Cu-doped ZnS. From the results of the CASTEP calculations, the bottom of conduction band is mainly constructed from Zn 4*s*4*p* orbitals, and the top of valence band consists of S 3*p* orbitals with partial contribution of Cu 3*d* orbitals. The hybridized Cu 3*d* and S 3*p* orbitals can lift up the top of the valence band,

which makes the Cu-doped ZnS sensitive to visible light.

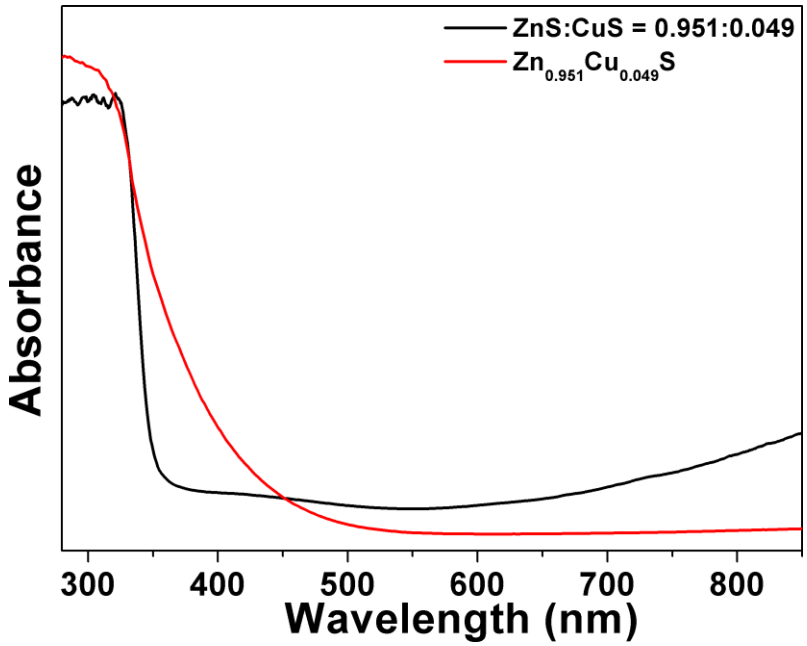

Figure 4.5 Comparison of UV-vis absorption spectra for $Zn_{0.951}Cu_{0.049}S$ and ZnS/CuS mixture.

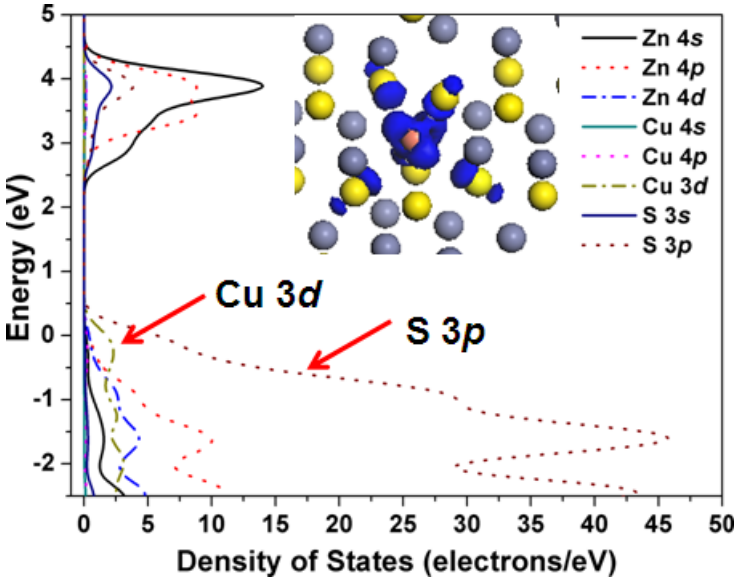

Figure 4.6 Total density of states (DOS) of Cu-doped ZnS by CASTEP calculation.

Brunauer-Emmett-Teller (BET) gas sorptometry measurements were performed to check the surface areas of the samples as shown in Table 2. For $Zn_{0.951}Cu_{0.049}S$, the surface area is as large as 201.1 m^2/g.

Table 4.2 Surface areas of samples characterized by Brunauer-Emmett-Teller (BET) gas sorptometry.

Sample	S_{BET} (m^2/g)
$Zn_{0.982}Cu_{0.018}S$	212.4
$Zn_{0.966}Cu_{0.034}S$	223.0
$Zn_{0.951}Cu_{0.049}S$	201.1
$Zn_{0.946}Cu_{0.054}S$	192.9
$Zn_{0.934}Cu_{0.066}S$	183.2

XRD was also carried out to identify the products synthesized without TU by our method and coprecipitation method (Figure 4.7). There are high intensity peaks of impurities in $Zn_{1-x}Cu_xS$-I with weaker signals of hexagonal ZnS marked by triangle symbols. The peaks of $Zn_{1-x}Cu_xS$-II can be indexed to cubic ZnS.

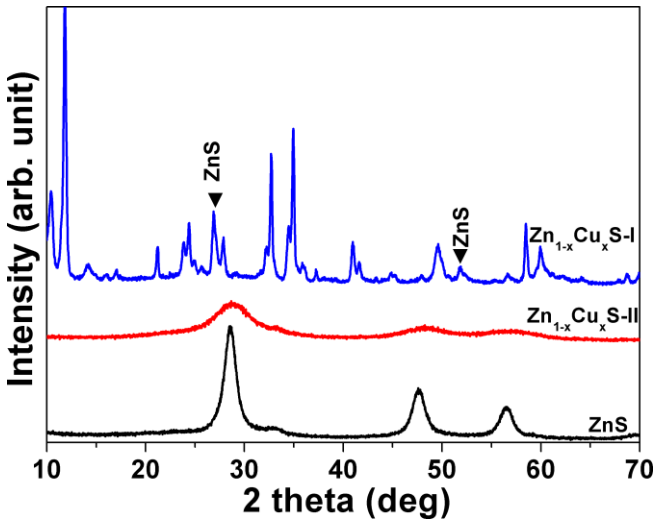

Figure 4.7 XRD patterns of (a) $Zn_{1-x}Cu_xS$-I synthesized without thiourea from ZnS precursor at 85 °C for 72 h, (b) $Zn_{1-x}Cu_xS$-II synthesized by coprecipitation method, and (c) cubic ZnS synthesized in this study.

TEM images of $Zn_{1-x}Cu_xS$-I (Figure 4.8) reveal that the products consist of microplates and nanorods with different sizes, its surface area intensively decreased to 23.2 m^2/g.

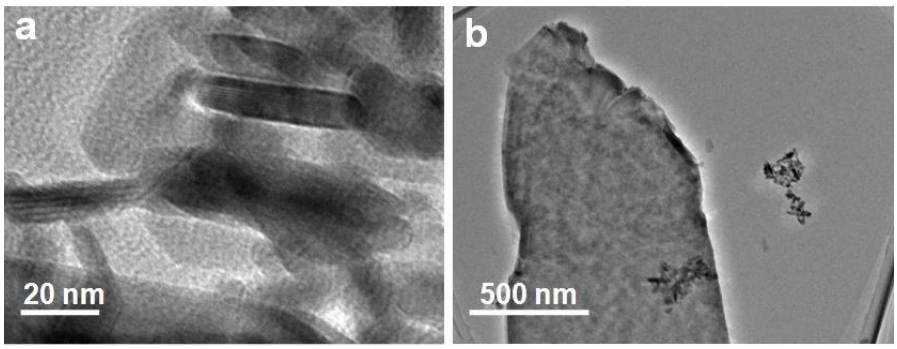

Figure 4.8 TEM images of $Zn_{1-x}Cu_xS$-I synthesized without thiourea from ZnS precursor at 85 °C for 72 h.

UV-vis absorption spectra of $Zn_{0.951}Cu_{0.049}S$ (synthesized by complexing-wet-chemical method), $Zn_{1-x}Cu_xS$-I, and $Zn_{1-x}Cu_xS$-II exhibit totally different patterns (Figure 4.9). For $Zn_{1-x}Cu_xS$-I, the absorption less than 550 nm must result from the band-gap transition between the valence band and conduction band of the impurity. The absorption between 550 nm and 850 nm should be attributed to the *d-d* transition of Cu^{2+} [12, 29, 30], which is substitution of Zn^{2+} to form copper sulfide, though it isn't detected by XRD probably due to its trace amount or poor crystallinity. $Zn_{1-x}Cu_xS$-II shows the similar absorption from 550 nm to 850 nm. However, $Zn_{0.951}Cu_{0.049}S$ shows no absorption in this range. Therefore, there is no doubt that TU plays a significant role in synthesizing ultrathin nanocrystal $Zn_{1-x}Cu_xS$ ($0 \leq x \leq 0.066$) with even distribution of Cu element in the samples. In this study, the ZnS precursor could decompose into Zn^{2+} and S^{2-}.Then Zn^{2+} and Cu^{2+} were combined with TU to produce $Zn(TU)_n^{2+}$ and $Cu(TU)_n^{2+}$ complexes, respectively. At last, $Zn(TU)_n^{2+}$, $Cu(TU)_n^{2+}$, and S^{2-} coprecipitated to form $Zn_{1-x}Cu_xS$ ($0 \leq x \leq 0.066$) at appropriate rate. On the other hand, TU also acted as capping reagent to prevent the formation of $Zn_{1-x}Cu_xS$ with bigger size and

reaction to form by-products. The entire reaction is exhibited as follows.

$$ZnS \leftrightarrow Zn^{2+} + S^{2-}$$

$$Zn^{2+} + n\mathrm{TU} \leftrightarrow Zn(\mathrm{TU})_n^{2+}$$

$$Cu^{2+} + n\mathrm{TU} \leftrightarrow Cu(\mathrm{TU})_n^{2+}$$

$$(1-x)Zn(\mathrm{TU})_n^{2+} + xCu(\mathrm{TU})_n^{2+} + S^{2-} \leftrightarrow Zn_{1-x}Cu_xS + n\mathrm{TU}$$

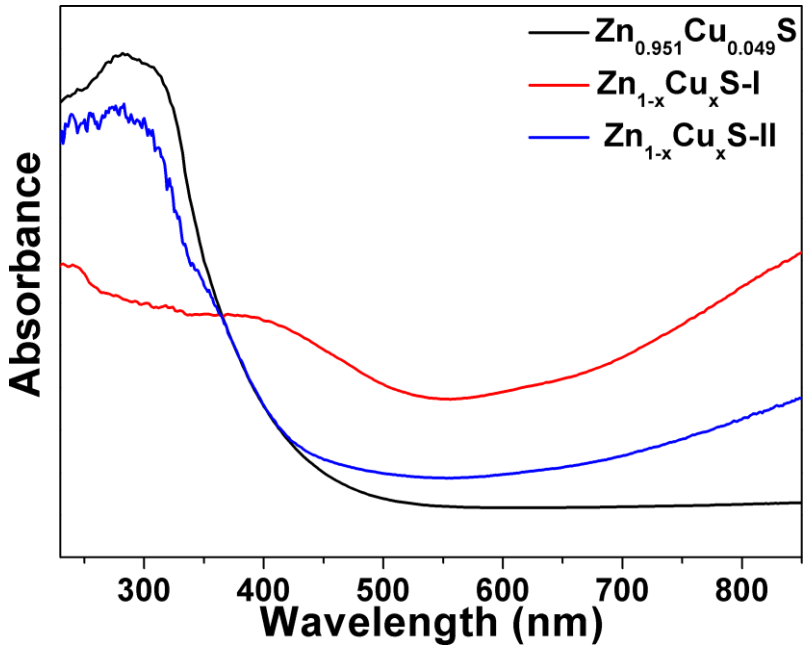

Figure 4.9 UV-vis absorption spectra of (a) $Zn_{0.951}Cu_{0.049}S$ synthesized by complexing-wet-chemical method at 85 °C for 72 h, (b) $Zn_{1-x}Cu_xS$-I synthesized without thiourea from ZnS precursor at 85 °C for 72 h, and (c) $Zn_{1-x}Cu_xS$-II synthesized by coprecipitation method at room temperature for 72 h.

X-ray photoelectron spectroscopy (XPS) was carried out for the surface analysis of $Zn_{1-x}Cu_xS$ to analyze chemical composition and valence status. Figure 4.10(a) reveals the XPS survey spectrum of Zn 2*p*, S 2*p*, O 1*s*, and C 1*s* of $Zn_{0.951}Cu_{0.049}S$. The peaks of Cu 2*p* are not obvious due to its low percentage. The peaks of O 1*s* and C 1*s* must come from H_2O, O_2, and CO_2 adsorbed on the samples and the hydrocarbon of XPS instrument [31]. Figure4.10(b) ~

(d) exhibit the peaks of Zn 2*p*1/2, Zn 2*p*3/2, Cu 2*p*1/2, Cu 2*p*3/2, and S 2*p*, locating at 1044.9 eV, 1022.0 eV, 952.1 eV, 932.8 eV, and 162.0 eV, respectively, which are values for Zn^{2+}, Cu^{2+}, and S^{2-} [32, 33].

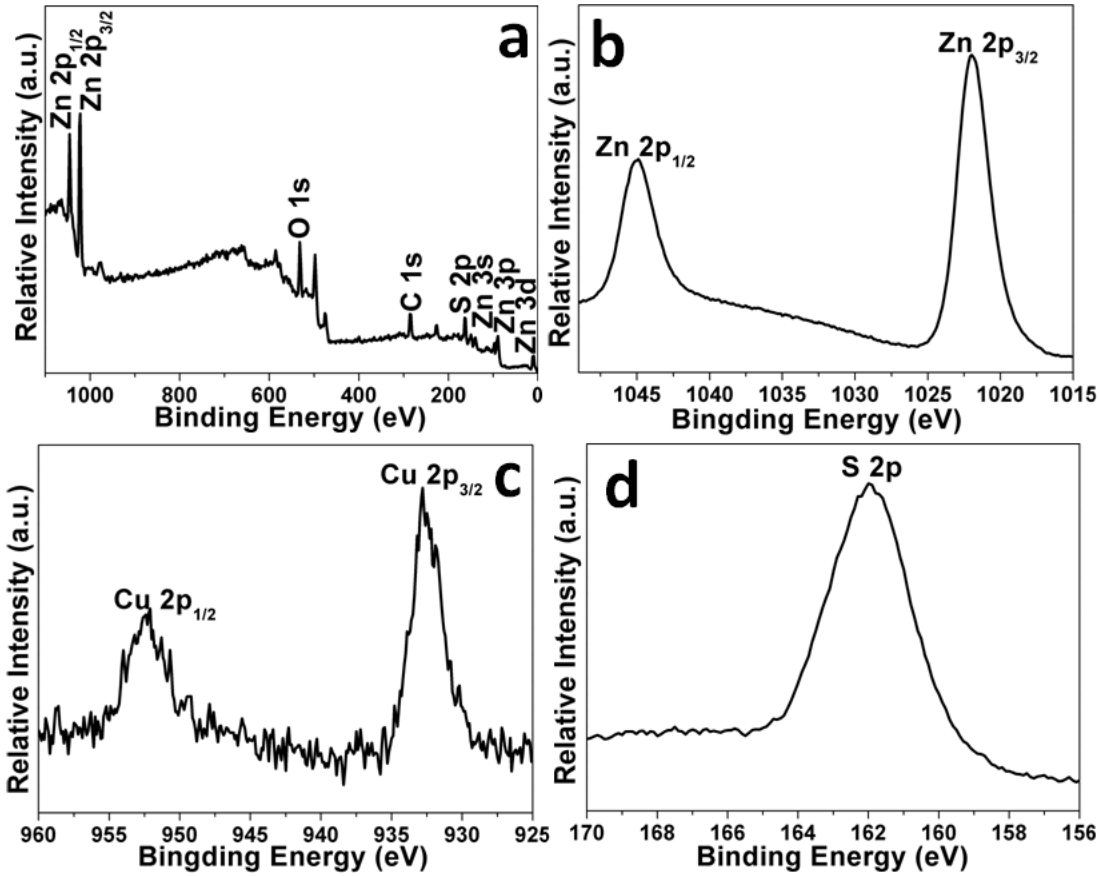

Figure 4.10 Typical room temperature XPS (a) survey spectrum, and spectra for (b) Zn 2*p*, (c) Cu 2*p*, and (d) S 2*p* of $Zn_{0.951}Cu_{0.049}S$, respectively.

Figure 4.11 (a) is the time course photocatalytic H_2 evolution without cocatalyst under visible-light irradiation ($\lambda > 400$ nm) in 0.35 M Na_2S/0.25 M K_2SO_3 aqueous solution (Amount of photocatalyst: 0.1 g). $Zn_{0.951}Cu_{0.049}S$ shows better photocatalytic H_2 evolution activity than other $Zn_{1-x}Cu_xS$ ($0 \leq x \leq 0.066$) in this work, and the H_2 evolution rate reaches about 189 μmol/h as shown in Figure 4.11 (b). Three runs were carried out to check the stability of $Zn_{0.951}Cu_{0.049}S$ and the reaction system was evacuated after each run as shown in

Figure4.12. The amount of evolved H_2 decreased in each run. It might result from the photo-corrosion of $Zn_{0.951}Cu_{0.049}S$, or the consumption of the sacrificial reagents in the solution [21].

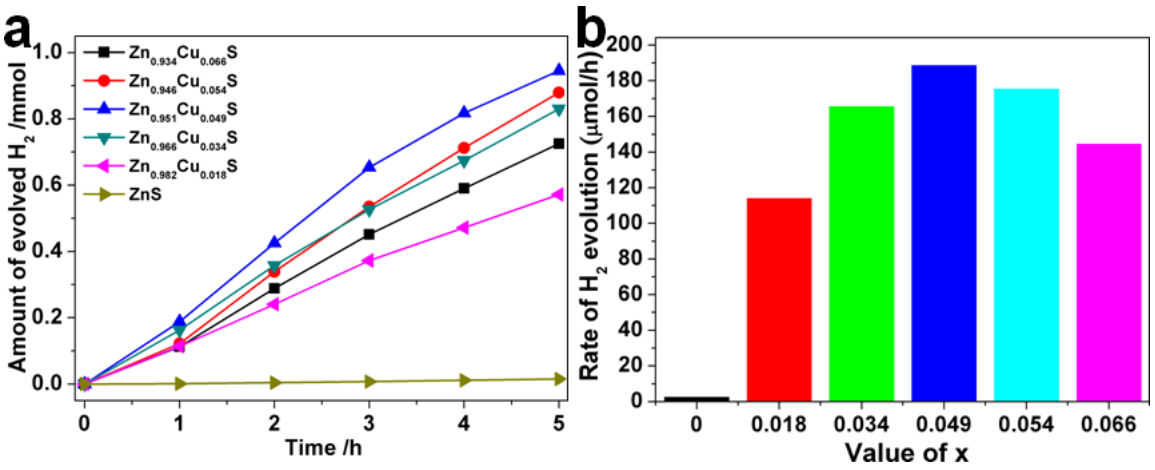

Figure 4.11 (a) Time course of photocatalytic H_2 evolution (b) H_2 evolution rate of $Zn_{1-x}Cu_xS$ ($0 \leq x \leq 0.066$) from 0.35 M Na_2S/0.25 M K_2SO_3 aqueous solution under visible-light irradiation ($\lambda > 400$ nm). Light source: 300 W of Xe lamp; Light filter: L42.

Compared with $Zn_{0.951}Cu_{0.049}S$ (Figure 4.13), pure ZnS exhibits trace photocatalytic activity under visible-light irradiation due to its wide band gap. As we know, CdS is an efficient photocatalyst for H_2 evolution by loading Pt as cocatalyst in S^{2-}/SO_3^{2-} aqueous solution under visible-light irradiation [34]. However, noble-metal-loading increases the cost which is one of the barriers for practical application. The H_2 evolution rate of CdS under the same synthesis and evaluation conditions is 15.2 μmol/h, which is about 1/12 of that of $Zn_{0.951}Cu_{0.049}S$. Because $Zn_{1-x}Cu_xS$ has negative enough conduction band for H^+ reduction even without cocatalyst. It is also found that the fabrication method of $Zn_{1-x}Cu_xS$ shows great impact on the photocatalytic activity. Our complexing-wet-chemical process fabricating $Zn_{0.951}Cu_{0.049}S$ much improves the H_2 evolution rate by 2.3 times than the traditional

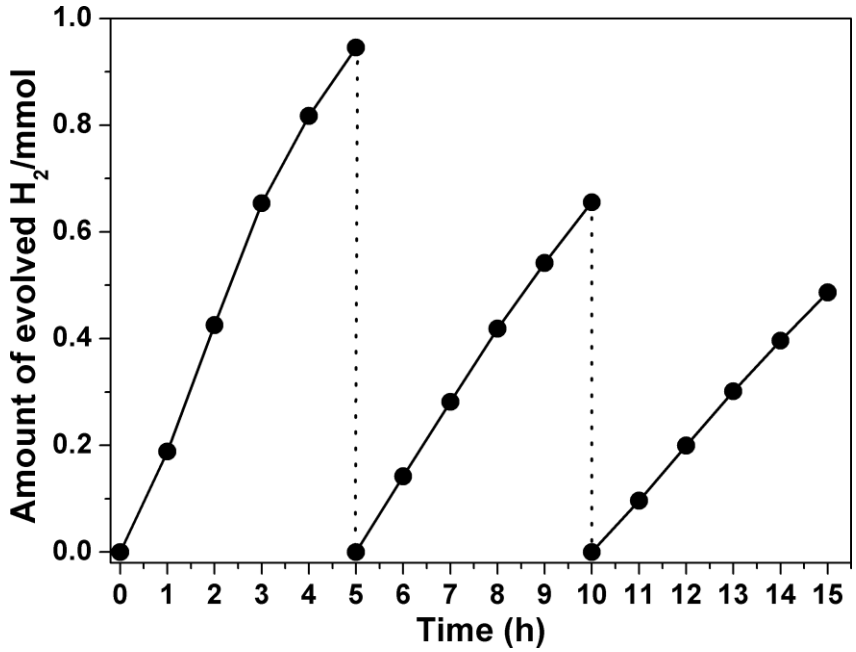

Figure 4.12 Amount of H_2 evolved at each run for $Zn_{0.951}Cu_{0.049}S$.

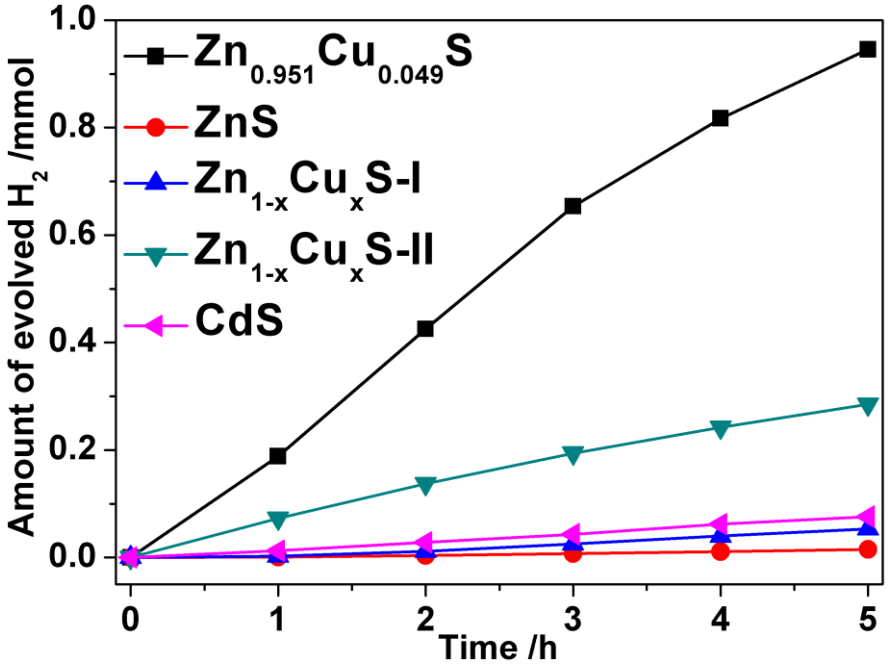

Figure 4.13 Time course of photocatalytic H_2 evolution of different photocatalysts (0.1 g) in comparison to $Zn_{0.951}Cu_{0.049}S$ without cocatalyst under visible-light irradiation ($\lambda > 400$ nm) in 0.35 M Na_2S/0.25 M K_2SO_3 aqueous solution. Light source: 300 W of Xe lamp; Light filter: L42.

coprecipitation method ($Zn_{1-x}Cu_xS$-II, H_2 evolution rate: 57.0 μmol/h). The decreased activity may result from the formation of CuS phase, which can prevent the efficient utilization of incident light in this case. $Zn_{1-x}Cu_xS$-I was fabricated by the same procedure as $Zn_{0.951}Cu_{0.049}S$ just without adding TU in the solution, its H_2 evolution rate is 10.6 μmol/h. The by-products show low photocatalytic activity.

Then why did the $Zn_{0.951}Cu_{0.049}S$ sample show the best photocatalytic activities in the doped products? Usually, the photocatalytic activities are mainly affected by the crystallinity, particle size, light absorption, and band structures. In this work, the crystallinity and particle size of the Cu-doped ZnS were similar. Thus the light absorption and band structures would show impacts on the photocatalytic activities of the Cu-doped ZnS. The increased light absorption of the doped products was calculated by the following equations as mentioned in Chapter 2.

$$N_{abs}(\lambda) = N_{inc}(\lambda) * I_{ab}$$

$$\sum_{420}^{800} N_{abs}\,(\lambda) = \sum_{420}^{800} N_{inc}\,(\lambda) * I_{ab} = \sum_{420}^{800} \frac{IAt\lambda}{hc} * I_{ab}$$

$$= 8.04 \times 10^{10} \sum_{420}^{800} I\lambda t * I_{ab}$$

in which *I*, *A*, *t*, *h*, *c*, and I_{ab} are the light intensity, irradiation area (16 cm^2), irradiation time, Planck constant, speed of light, and relative absorptivity, respectively. The light intensity can be measured by a light intensity meter and UV-vis absorption meter, respectively. In comparison with ZnS, the increased light absorption (times) of the doped products in visible-light region was shown as the black line in Figure 4.14, it can be seen that the times were increased with increasing the Cu dopant. However, when *x* is 0.049, the sample shows the largest AQE (6.9%, blue line) around 418.5 nm. Therefore, the band structures must show effects on the photocatalytic activities besides the light absorption.

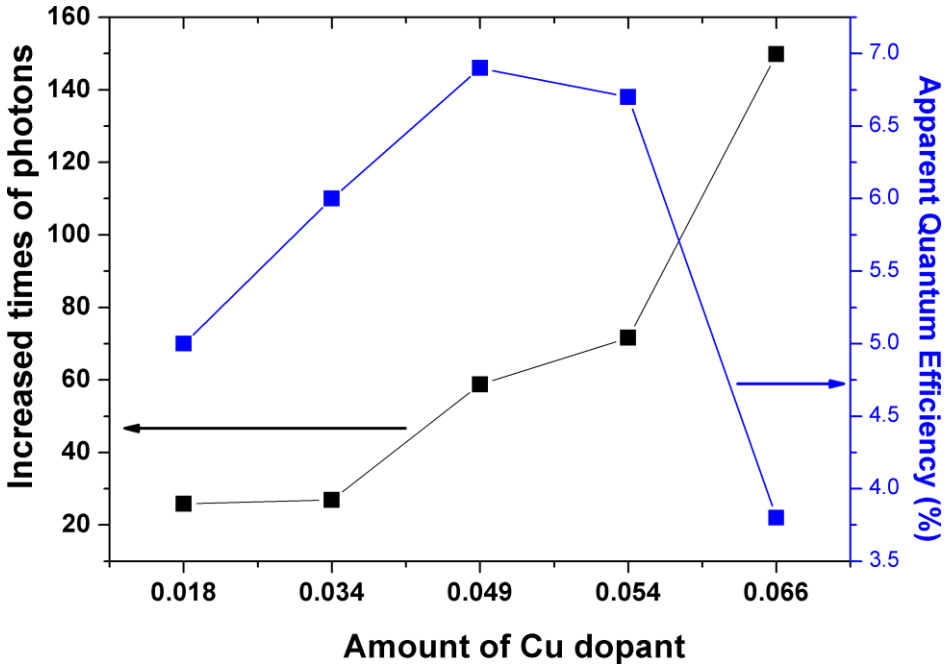

Figure 4.14 Increased times of absorbed photons compared with ZnS in the visible-light region (black line) and AQE (blue line) of different samples around 418.5 nm.

The band gaps of the products were calculated in line with of $\alpha hv = A(hv - E_g)^{n/2}$, in which α, v, A, and E_g signify the absorption coefficient, light frequency, proportionality constant, and band gap, respectively, and n equals 1 or 4 depending on whether the band gap is direct or indirect. Here $n = 1$ because ZnS is a direct band gap semiconductor. The concrete values are shown in Figure 4.15. Then the absorption band edges ($1240/E_g$) are 442.9 nm, 442.9 nm, 476.9 nm, 496.0 nm, 516.7 nm, respectively. Therefore, I checked the AQE till around their absorption band edges, which were shown in Table 4.3.

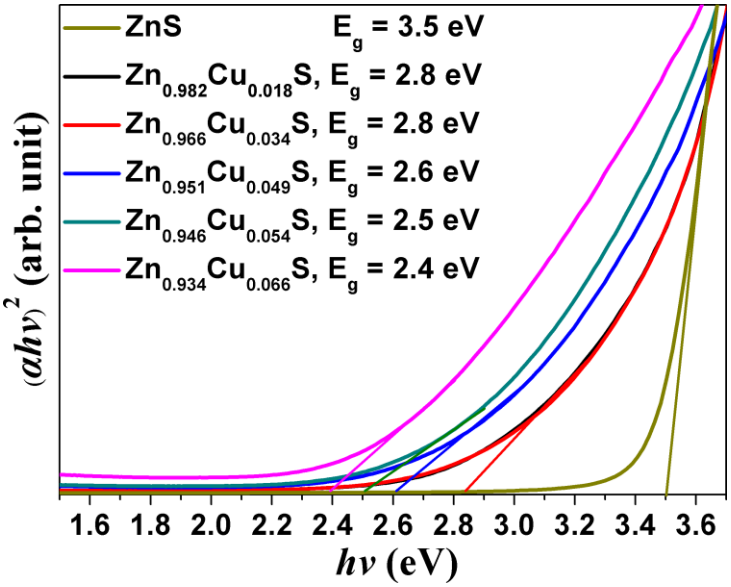

Figure 4.15 Band gaps of ZnS and Cu-doped ZnS products.

Table 4.3 AQE of the Cu-doped ZnS products around different wavelength.

Sample	Wavelength region (nm)	AQE
$Zn_{0.982}Cu_{0.018}S$	418.5±14.5	5.0%
$Zn_{0.966}Cu_{0.034}S$	418.5±14.5	6.0%
$Zn_{0.951}Cu_{0.049}S$	418.5±14.5	6.9%
	462.4±13.9	2.5%
	479.3±11.1	1.2%
$Zn_{0.946}Cu_{0.054}S$	418.5±14.5	6.7%
	462.4±13.9	2.9%
	479.3±11.1	0.76%
	498.4±10.9	0.38%
$Zn_{0.934}Cu_{0.066}S$	418.5±14.5	3.8%
	462.4±13.9	1.2%
	479.3±11.1	0.74%
	498.4±10.9	0.40%
	517.5±14.7	0.18%

Based on the theoretical calculation, the Cu 3*d* orbitals only changed the valence band energy. Therefore, the band positions of the products can be shown as Figure 4.16. The Cu dopant lifts up the valence band top, and the visible-light absorption increases with increasing the Cu dopant. However, the oxidation ability of holes decreases. Therefore, when *x* equals 0.049, the sample reaches the best balance between the light absorption and oxidation ability of holes, and accordingly shows the best photocatalytic activities.

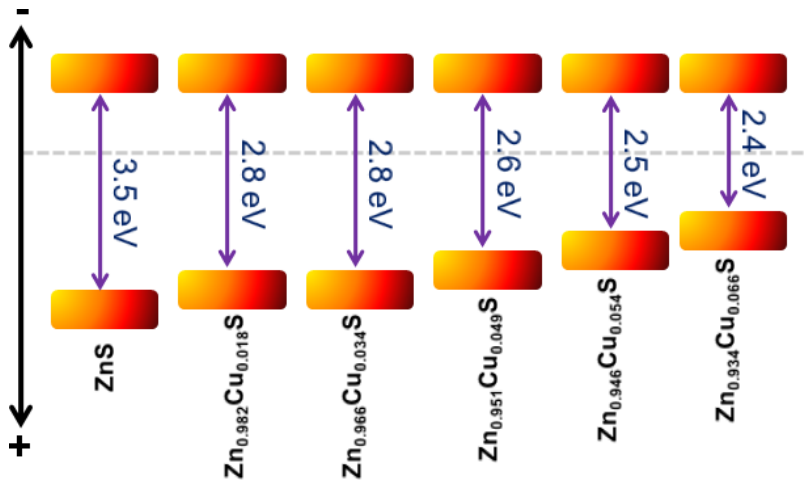

Figure 4.16 Band positions of ZnS and Cu-doped ZnS products.

4.6 Conclusions

(I) $Zn_{1-x}Cu_xS$ ($0 \leq x \leq 0.066$) ultrafine nanocrystalline was synthesized under well control by complexing-wet-chemical method using thiourea as the complex reagent. Thiourea can act as not only complexing reagent to adjust the reaction rate to synthesize $Zn_{1-x}Cu_xS$ ($0 \leq x \leq 0.066$) with homogeneous distribution of Cu element in the whole samples, but also capping reagent to confine the particle size and prevent the unexpected reaction to producing impurities.

(II) The photocatalytic H_2 evolution rate of $Zn_{0.951}Cu_{0.049}S$ is 189 μmol/h without cocatalyst from 0.35 M Na_2S/0.25 M K_2SO_3 aqueous solution under visible-light irradiation. It is about 11 times higher than that of CdS synthesized under the same conditions; it is also about 3.3 times as high as that of the product synthesized by the traditional coprecipitation method. The apparent quantum efficiency of $Zn_{0.951}Cu_{0.049}S$ is about 6.9% around 418.5 nm.

(III) The high photocatalytic H_2 evolution activity is induced by the synergism of more appropriate band structure and more efficient untilization of incident light. Due to the highly negative conduction band of $Zn_{0.951}Cu_{0.049}S$, it can split water into H_2 even without cocatalyst. Our method provides useful information to well control chemical reaction and fabricate ultrafine particles by wet chemical process.

References

[1] Kato H, Asakura K and Kudo A 2003 *J. Am. Chem. Soc.* **125** 3082.

[2] Zhang Z B, Wang C C, Zakaria R and Ying J Y 1998 *J. Phys. Chem. B* **102** 10871.

[3] Yu L H, Xi J Y, Li M D, Chan H T, Su T, Phillips D L and Chan W K 2012 *Phys. Chem. Phys. Chem.* **14** 3589.

[4] Wu J J, Huang F Q, Lü X J, Chen P, Wan D Y and Xu F F 2011 *J. Mater. Chem.* **21** 3872.

[5] Zheng H D, Ou J Z, Strano M S, Kaner R B, Mitchell A and Kalantar-zadeh K 2011 *Adv. Funct. Mater.* **21** 2175.

[6] Rothenberger G, Moser J, Grätzel M, Serpone N and Sharma D K 1985 *J. Am. Chem. Soc.* **107** 8054.

[7] Li Z S, Yu T, Zou Z G and Ye J H 2006 *Appl. Phys. Lett.* **88** 071917.

[8] Cao L X, Spiess F J, Huang A M, Suib S L, Obee T N, Hay S O and Freihaut J D 1999 *J. Phys. Chem. B* **103** 2912.

[9] Zhang N, Ouyang S X, Kako T and Ye J H 2012 *Chem. Commun.* **48** 1269.

[10] Zhang Q, Chi W Y, Zhang W W, Lv C Y and Li J X 2012 *New J. Chem.* **36** 119.

[11] Hu J S, Ren L L, Guo Y G, Liang H P, Cao A M, Wan L J and Bai C L 2005 *Angew. Chem. Int. Ed.* **44** 1269.

[12] Zhang J, Yu J G, Zhang Y M, Li Q and Gong J R 2011 *Nano Lett.* **11** 4774.

[13] Reber J F and Meier K 1984 *J. Phys. Chem.* **88** 5903.

[14] Youn H C, Baral S and Fendler J H 1988 *J. Phys. Chem.* **92** 6320.

[15] Kudo A and Sekizawa M 2000 *Chem. Commun.* **15** 1371.

[16] Bang J H, Helmich R J and Suslick K S 2008 *Adv. Mater.* **20** 2599.

[17] Arai T, Senda S, Sato Y, Takahashi H, Shinoda K, Jeyadevan B and Tohji K 2008 *Chem. Mater.* **20** 1997.

[18] Wang W Z, Zhu W and Xu H L 2008 *J. Phys. Chem. C* **112** 16754.

[19] Tsuji I, Kato H, Kobayashi H and Kudo A 2004 *J. Am. Chem. Soc.* **126** 13406.

[20] Tsuji I, Kato H and Kudo A 2005 *Angew. Chem. Int. Ed.* **44** 3565.

[21] Li Y X, Chen G, Wang Q, Wang X, Zhou A K and Shen Z Y 2010 *Adv. Funct. Mater.* **20** 3390.

[22] Yu J G, Zhang J and Liu S W 2010 *J. Phys. Chem. C* **114** 13642.

[23] Yu Y F, Zhang J, Wu X, Zhao W W and Zhang B 2012 *Angew. Chem. Int. Ed.* **51** 897.

[24] Kudo A and Sekizawa M 1999 *Catal. Lett.* **58** 241.

[25] Zhang W, Zhong Z Y, Wang Y S and Xu R 2008 *J. Phys. Chem. C* **112** 17635.

[26] Wang Z, Qian X F, Yin J and Zhu Z K 2004 *Langmuir* **20** 3441.

[27]Ghahremaninezhad A, Asselin E and Dixon D G 2011 *J. Phys. Chem. C* **115** 9320.

[28] Han S K, Kong M G, Guo Y and Wang M T 2009 *Mater. Lett.* **63** 1192.

[29] Qiu X Q, Miyauchi M, Yu H G, Irie H and Hashimoto K 2010 *J. Am. Chem. Soc.* **132** 15259.

[30] Yu H G, Irie H and Hashimoto K 2010 *J. Am. Chem. Soc.* **132** 6898.

[31] Yu J G, Hai Y and Cheng B 2011 *J. Phys. Chem. C* **115** 4953.

[32] Jiang C L, Zhang W Q, Zou G F, Xu L Q, Yu W C and Qian Y T 2005 *Mater. Lett.* **59** 1008.

[33] Chen Z X, Li D Z, Zhang W J, Chen C, Li W J, Sun M, He Y H and Fu X Z 2008 *Inorg. Chem.* **47** 9766.

[34] Bao N Z, Shen L M, Takata T and Domen K 2008 *Chem. Mater.* **20** 110.

Chapter 5 General Conclusions and Future Prospects

5.1 General conclusions

Solar energy conversion has been given tremendous research activities and H_2 is regarded as a clean energy. In this case, photocatalysts are ideal intermediates for solar energy conversion to chemical energy in H_2 through photocatalytic water splitting. However, the biggest bottleneck of water splitting is the separation and migration ability of photoexcited electrons and holes. In this thesis, I aimed at developing efficient photocatalysts for H_2 evolution under visible-light irradiation from water. I adopted two strategies to achieve high efficiency of energy conversion: (1) fabricating appropriate semiconductor composites with matching conduction and valence bands to enhance the separation and migration ability of photogenerated electrons and holes, and accordingly enhance the photocatalytic activities; (2) fabricating photocatalyst with intrinsically high photocatalytic activity and tailoring it by nanotechnology. The main conclusions of this thesis are summarized as follows:

1. Zinc indium oxide ($Zn_5In_2O_8$)/surface-S-doped $Zn_5In_2O_8$composites (ZIO/S-doped V-ZIO and ZIO/S-doped ZIO) were synthesized through a photoassisted method under UV-vis light irradiation in the Na_2S/K_2SO_3 aqueous solution. Indium vacancies, which were promoted by adding Cu powder in the treatment process in the NaCl/KCl molten-salt under Ar atmosphere, played a significant role in enhancing the photocatalytic activity for H_2 evolution under visible-light irradiation from the Na_2S/K_2SO_3 aqueous solution. In comparison with ZIO, the deficient of indium element in S-doped V-ZIO shifted the bottom of its conduction band to a more negative position and the top of its valence band was shifted to a more positive position by S 3*p* orbitals. Thus, the photoexcited electrons transferred from the

conduction band of S-doped V-ZIO to the conduction band of ZIO, and simultaneously the photoexcited holes transferred from the valence band of ZIO to the valence band of S-doped V-ZIO, this process greatly enhanced the separation ability of the photoexcited charges. The photocatalytic H_2 evolution rate of ZIO/S-doped V-ZIO composite was 18 times as high as that of ZIO/S-doped ZIO composite. The apparent quantum efficiency of ZIO/S-doped V-ZIO composite was about 5.2% at 420 nm.

2. Bulk composites show more advantages for the enhancement of photocatalytic activities due to the more influent and tight contact of interface of the components. In_2S_3 and $ZnIn_2S_4$ are good candidates for photocatalytic H_2 evolution under visible-light irradiation. In order to achieve high photocatalytic activities, $In_2S_3/ZnIn_2S_4$ bulk composites were designed and synthesized by a facile ion-exchange route using $NaInS_2$ as the precursor. In comparison with In_2S_3 and $ZnIn_2S_4$, $In_2S_3/ZnIn_2S_4$ bulk composites show greatly enhanced photocatalytic activities. The highest H_2 evolution rate of $In_2S_3/ZnIn_2S_4$ bulk composite was 67.8 μmol/h under visible-light irradiation from the Na_2S/K_2SO_3 aqueous solution. The enhanced photocatalytic activity of $In_2S_3/ZnIn_2S_4$ bulk composites resulted from the improved separation ability of the photoexcited electrons and holes. Furthermore, the fluent interface of $In_2S_3/ZnIn_2S_4$ bulk composites must play a significant role in enhancing the photocatalytic activity.
3. It is important to develop high efficient and nontoxic photocatalysts based on earth-rich elements. Ultrafine $Zn_{1-x}Cu_xS$ nanocrystalline was synthesized by a complexing-wet-chemical method. During the fabrication process, thiourea acted as not only complexing reagent to adjust the reaction rate to synthesize homogeneous $Zn_{1-x}Cu_xS$ ($0 \leq x \leq 0.066$), but also capping reagent to confine the particle size and prevent the formation of impurities. $Zn_{0.951}Cu_{0.049}S$ showed the highest photocatalytic H_2

evolution activity under visible-light irradiation from Na_2S/K_2SO_3 aqueous solution without cocatalyst. The high activity was induced by the synergism of appropriate band structure and efficient untilization of the incident light.

5.2 Future prospects

In this work, effective routes have been developed to synthesize the $Zn_5In_2O_8$/surface-S-doped $Zn_5In_2O_8$ composite and $In_2S_3/ZnIn_2S_4$ bulk composite. On the other hand, ultrafine $Zn_{1-x}Cu_xS$ nanocrystalline has also been synthesized by a complexing-wet-chemical method. All the photocatalysts developed in our work showed efficient photocatalytic activities for H_2 evolution under visible-light irradiation. However, there are still some challenges and problems, which are necessary to overcome in the future.

1. The $Zn_5In_2O_8$/surface-S-doped $Zn_5In_2O_8$ composite was successfully synthesized in our work, which showed efficient photocatalytic activity for water splitting due to the enhanced separation and migration ability of the photoexcited electrons and holes. It is also meaningful to successfully synthesize the single phase of S-doped $Zn_5In_2O_8$ and study its photocatalytic activities.
2. In the research of $In_2S_3/ZnIn_2S_4$ bulk composites, the bulk composite has large space to improve its photocatalytic activity. In this respect, I plan to synthesize this bulk composite with better crystallinity, less defect, and smaller size. On the other hand, it is also meaningful to fabricate other bulk composites with better photocatalytic activities based on this method.
3. The $Zn_{1-x}Cu_xS$ is a promising candidate for practical application due to its high activity, low toxicity, low cost, and facile fabrication for mass production. Due to its excellent characters, it also shows potential applications as other functional materials, such as solar cell and photoluminescence materials.

4. The comparatively low photocatalytic stability of metal sulfides is the biggest challenge for their practical application. We can try the following strategies to overcome this problem: (i) Based on the previous research, an oxysulfide shows higher stability than the sulfide photocatalyst, and it also shows narrower band gap than its oxide counterpart. Thus, it is meaningful to develop new and high efficient oxysulfide photocatalysts; (ii) Developing high effective acceptors of photoexcited holes will be an effective route to suppress the photocorrosion of metal sulfide photocatalysts; (iii) Developing new sacrificial reagents might be another approach to suppress the photocorrosion of sulfide photocatalysts.

ACKNOWLEDGMENTS

This thesis was finished under the direction of my supervisors, Prof. Jinhua Ye and Associate Prof. Tetsuya Kako. I want to take this chance to appreciate their great help, apropos suggestions, and encouragement. Prof. Ye is a famous scientist in the photocatalysis and materials chemistry fields. She has profound knowledge, and she is also rigorous scholarship. Furthermore, she is a wise person with integrity and modesty. She has shown great impacts on my research and daily life. It is a treasure for me.

Associate Prof. Kako also gave me so many impacts due to his knowledge, friendship, and sense of humor. He is strict on science, but this can't prevent him from being a kind man. His direction and suggestion to my research activities were very valuable, which made my research smoother.

I also must thank Dr. Ouyang Shuxin. He taught me lots of useful knowledge on photocatalysis and experimental experience. I also acquired skills of writing a science paper with his help.

I still would like to thank Dr. Junyu Cao, a warmhearted and kind guy. He helped me so much not only with my research work, but also with my personal affairs. I will always remember him in my mind as a good friend.

I also would like to thank Takehiko Matsumoto sensei, Dr. Naoto Umezawa, Dr. Hideki Abe, Dr. Masanobu Naito, Dr. Jun Li, Dr. Dai-Ming Tang, Mrs. Junko Ito, Miss Haruna Kurokawa, Mrs. Sachiko Tanaka, Mrs. Liqun Yang, Mrs. Aya Hagino and Mrs. Takako Tsubata, who gave me suggestions and so much support for my research.

Then I want to thank my previous and present group members, Dr. Hua Tong, Dr. Qiuye Li, Dr. Bi Yingpu, Dr. Yuanjian Zhang, Dr. Guangchen Xi, Dr. Kui Xie, Dr. Xiaoqing Chen, Dr. Bing Yue, Dr. Lequan Liu, Dr. Han Zhou, Dr. Qing Kang, Dr. Ning Zhang, Dr. Peng Li,

Mr. Jianjun Guo, Miss Hua Xu, and Mr. Xianguang Meng, for their help with both academics and life.

I also want to take this chance to thank the Chinese government, who supports my life expense during my Ph.D course. Here, I hope my homeland gets stronger and more prosperous.

Lastly, I must thank my family and my close friends. They support me and stand by me all the time. They are my loyal companies when I am in trouble. Because of your support and understanding, I am full of courage to overcome all the difficulties in my life. Thank you very much for your unselfish love and help.

Academic Activities

Published papers

1. **Zongwei Mei**, Ning Zhang, Shuxin Ouyang, Yuanjian Zhang, Tetsuya Kako, and Jinhua Ye*****

Photoassisted fabrication of zinc indium oxide/oxysulfide composite for enhanced photocatalytic H_2 evolution under visible-light irradiation.

Science and Technology of Advanced Materials 2012 **13** 055001.

2.**Zongwei Mei**, Shuxin Ouyang, Dai-Ming Tang,Tetsuya Kako, Dmitri Golberg, Jinhua Ye*****

Facile ion-exchange route for the synthesis of $In_2S_3/ZnIn_2S_4$ bulk composite and its photocatalytic activity under visible light irradiation.

Dalton Transactions, 2013 **42** 2687.

3. **Zongwei Mei***, Shuxin Ouyang, Yuanjian Zhang, and Tetsuya Kako.

Ultrafine $Zn_{1-x}Cu_xS$ ($0 \leq x \leq 0.066$) nanocrystallites for photocatalytic H_2 evolution under visible light irradiation.

RSC Adv. 2013 **27** 10654.

Presentations

(1) Zongwei Mei, Shuxin Ouyang, Dai-Ming Tang, Tetsuya Kako, Dmitri Golberg, Jinhua Ye.

"Facile ion-exchange route for the synthesis of $In_2S_3/ZnIn_2S_4$ bulk composite and its photocatalytic activity under visible-light irradiation" **Verbal & poster presentation**

第 19 回シンポジウム「光触媒反応の最近の展開」Tokyo University, Dec. 2012.

(2) Zongwei MEI, Tetsuya KAKO, Jinhua YE.

"Enhanced photocatalytic H_2 evolution of Zinc indium oxide/oxysulfide composite under visible light irradiation" **Verbal presentation**

日本化学会第 92 春季年会(2012),慶應義塾大学, 25th Mar. 2012.

(3) Zongwei Mei, Ning Zhang, Shuxin Ouyang, Yuanjian Zhang, Tetsuya Kako, Jinhua Ye.

"Photo-assisted fabrication of zinc indium oxide/oxysulfide composite for enhanced photocatalytic H_2 evolution under visible light irradiation" **Verbal&poster presentation**

第 18 回シンポジウム「光触媒反応の最近の展開」Tokyo University, 12th Dec. 2011.

(4) Zongwei Mei, Ning Zhang, Shuxin Ouyang, Tetsuya Kako, Jinhua Ye.

Fabrication of Zinc Indium oxide/oxysulfide composite for enhanced photocatalytic H_2 evolution from water under visible light irradiation" **Verbal & poster presentation**

NIMS International Symposium on Photocatalysis and Environmental Remediation Materials 2011 & The 4th Japan-China Symposium on Advanced Photocatalytic Materials, NIMS, 16th Jan. 2011.